Crustal velocity-depth model from Barents Sea Southeast based on a SSW-NNE oriented OBS-profile transecting the Tiddlybanken Basin and the Bjarmeland Platform

Sune Aase Tønnessen

Master of Science Thesis in
Marine Geology and Geophysics

Department of Earth Science
University of Bergen
November 2014

“We shall not cease from exploration
And the end of all our exploring
Will be to arrive where we started
And know the place for the first time”

I - ABSTRACT

A crustal model transecting the Tiddlybanken Basin, Hjalmar Johansen High and Bjarmeland Platform in the Barents Sea Southeast have been constructed with emphasis on P-wave phase picking and subsequent P-wave model-building with the ray-tracing software MacRay (Luetgert, 1992). The final model consist of a 7-8 km thick cover of platform sediments of Late Paleozoic – to Mesozoic age., underlain by a up to 11 km thick layer of Late Proterozoic age (Riphean Complex). The upper crystalline basement is situated at extreme depth of 13-16 km and is characterized by an irregular topography that can be divided into a basement high corresponding to Hjalmar Johansen High, and two basin-shaped depressions corresponding to Tiddlybanken Basin in the SSE of the profile and Bjarmeland Platform in the NNE of the profile. The crustal thickness is quite thin taken into consideration that the area is characterized as a platform area. The crust can be divided into an upper and a middle crust with the respective velocity-intervals of 6.15 - 6.35 km s^{-1} and 6.5 – 6.7 km s^{-1}. The depth-position of the upper crust was poorly covered by arrivals due to the overprint over multiples from earlier arrivals; whereas the middle crust was characterized by high reflectivity and high amplitude arrivals. The Moho-discontinuity is situated at 32-34 km depth, and was covered by high-amplitude arrivals which could be picked at great offset-intervals.

II - ACKNOWLEDGMENTS

I would like to express my gratitude to my supervisor, Pr. Rolf Mjelde, whose theoretical expertise has been invaluable. His guidance trough discussions and constructive feedbacks from the very initial model-building too concluding levels are highly appreciated.

Special thanks go out to Dr. Alexey Shulgin from the Research Center for Marine Geosciences *(GEOMAR)* for assistance with the modeling. He was responsible for teaching me the actual execution of the different software's, and also organizing and customizing the seismic data to simplify the user-interface. I also appreciate that he took the time to answer questions by e-mail.

I am grateful to friends and fellow students for an enjoyable time at the university, and the exchange of competence on varied topics. Especially thanks to MSc. Anders Bjerga for a complete grammar check before submission.

At last, but not least, I am indebted to my family for their support and caring presence throughout my study- and lifetime.

Sune Aase Tønnessen

20 November, 2014

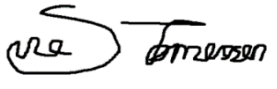

Table of contents

1 Introduction

1.1 Aim and background

The aim of this master thesis in marine geology- and geophysics was to construct a realistic P-wave velocity-depth model of the sedimentary cover, the crust and uppermost mantle from a SSW-NNE-trending OBS transect conducted in the formerly disputed area off the Barents Sea Southeast. The final velocity-depth model is based on phase-identification and interpretation of wide-angle refraction- and reflection events; subsequently compared with a synthetic velocity-depth model constructed in the interactive 2-D ray-tracing software MacRay (Luetgert, 1992). A coincident multi-channel reflection-profile with constraint on the sedimentary cover was provided by the Norwegian Petroleum Directorate (NPD) in order to construct an initial model of the sedimentary cover. Main targets of the modeling was to constrain: (i) the velocity-distribution, thickness and geometry of the sedimentary succession; (ii) top-to-depth position and physiographic characteristic of the crystalline basement; (iii) the velocity-distribution, thickness and intra-crustal structures of the crust; (iv) the depth position and geometry of the upper mantle; and (v) mapping of possible high-velocity deep-seated underplated body of mafic composition.

As the area of study remains relatively unexplored in comparison to adjacent areas such as the East Barents megabasin on Russian territory and the southwestern Barents shelf area on Norwegian territory, this study will hopefully contribute to a better understanding on how the areas are linked together, and contribute to a better understanding of the local geology in general.

1.2 Study area

The study area is situated in Barents Sea Southeast, alternatively referred to as Central Barents Sea. The area is part of the former disputed area between Norway and Russia, referred to as the “grey zone” as it has been closed for scientific and commercial exploration and industrial exploitation for over 40 years due to political disagreements on the dividing-line (delimitation agreement) between the states. The “grey-zone” covers about 44 000 km^2, accounting for 12 % of the total area of the Barents Sea, and corresponds to approximately 45 % of Norway’s total land area (Arctic Forum Foundation and NPD). A breakthrough in the

negotiations was archived on 7th of July, 2011 when the area was declared open. Since this day, NPD (the Norwegian Petroleum Directorate) have conducted several multichannel seismic reflection profiles across the area in order to evaluate the hydrocarbon potential. Since the availability of this data still remain unpublished, or restricted, the information on the geology of the area is quit sparse, especially for sub-basement structures which mainly constitute a target for scientific exploration more than for hydrocarbon-prospecting and economic reasons.

The seismic transect that this thesis is based on was conducted in approximation to the marine boarder of Russia. The transect is trending NNE-SSE with starting point at the Tiddlybanken Basin at coordinates 72° 05’33’’ N, 33° 46’50’’ E, crossing Hjalmar Johansen High and ends up at Central Barents margin at the Bjarmeland Platform at coordinates 74° 01’54 N, 36° 51’41’’ E (Fig. 1.1). Adjacent structural elements include the Finnmark Platform, Central Barents High and the Nordkapp Basin. The total length of the acquired profile is 237.5 km containing a total of 20 OBS-recordings.

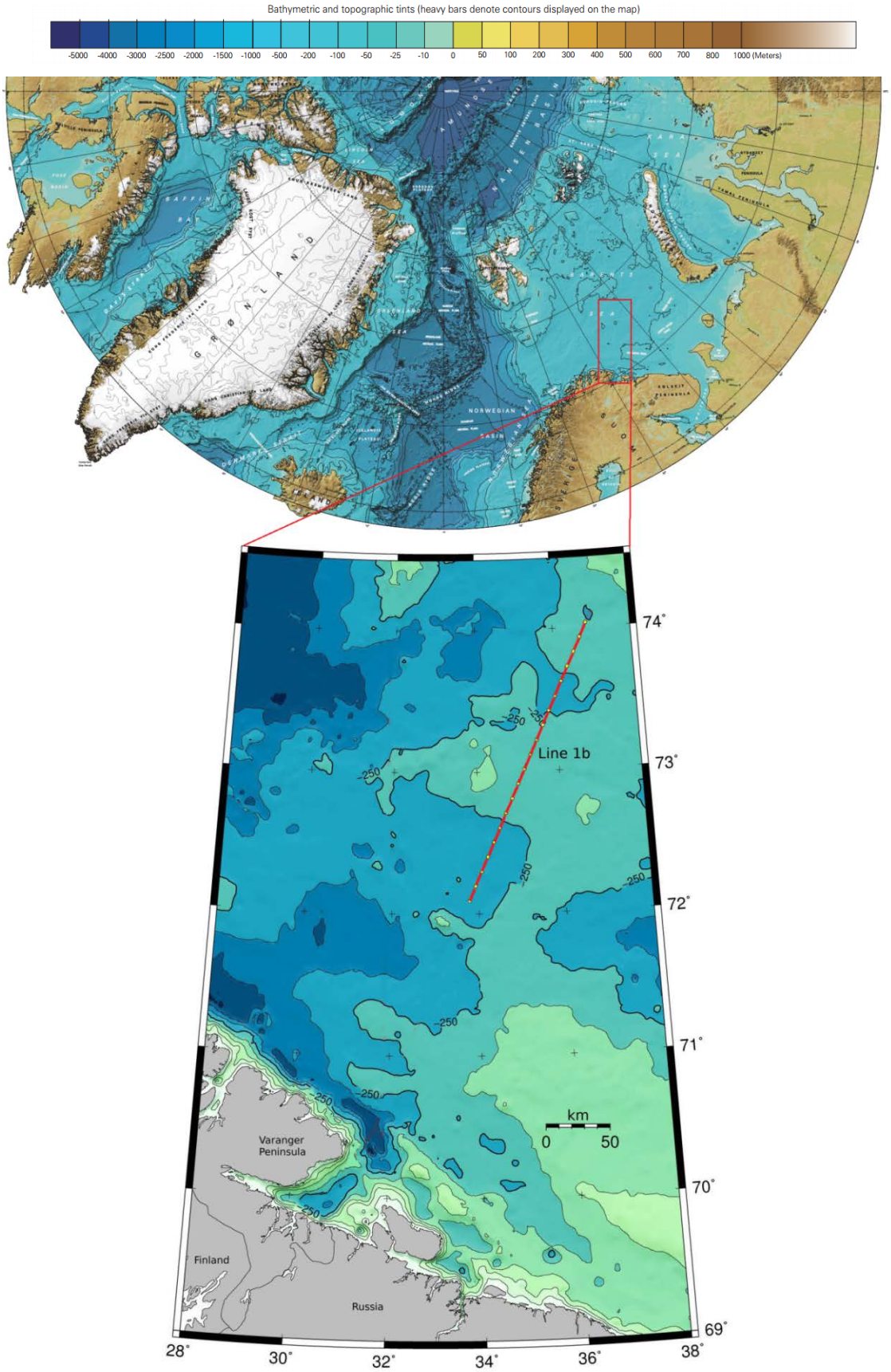

Fig.1.1 *– Geographic overview of the Study area. Top picture is a bathymetric chart over the Arctic ocean from Jakobsson et al. (2012), with study area highlighted inside red rectangle. Bottom picture indicates the survey route of the seismic transect (red line) and the position of the OBS-stations (yellow circles).*

2 Geological framework

2.1 Tectonic evolution of the Norwegian margin and the Barents Sea

The plate-configuration between the currently passive continental margin of Norway and the conjugate passive margin of Greenland reveal complex structures (Fig. 2.1) developed in accordance with a complete Wilson Cycle (1966). The margin-evolution can be categorized into three main tectonic phases based on the following sequence of plate-tectonic events:

2.1.1 The Caledonian orogeny and the amalgamation of Laurasia

The first phase comprises the Early Ordovician closing of the proto-Atlantic Iapetus Ocean separating Baltica from Laurentia until Late Silurian to Early Devonian time (Roberts and Gee, 1985) when the subsequent collision results in the Caledonian Orogeny and the formation of the supercontinent Laurussia. The suturing was initiated by a west-directed subduction of the oceanic crust and partial subduction of the Baltic plate beneath Laurentia during Cambrian-Devonian time (Krogh, 1977, Roberts and Gee, 1985). The orogeny enabled the onset of five allocthons (orogenic wedge) onto the Baltic shield (Gee et al., 2008) by translation on top of basal décollement zones (Hossack and Cooper, 1986). In Early Devonian, the allocthons where reactivated again by backsliding on the same décollement zones (Fossen, 1992, Fossen, 2000, Andersen, 1998, Terry et al., 2000); followed by orogenic collapse of hinterland parts of the orogeny in Early Cenozoic (Andersen, 1998).

The tectonic evolution of the Barents shelf in Ordovician to Devonian time was characterized by extensional tectonism, possibly related to back-arch spreading in the Uralien Ocean (O'Leary et al., 2004) and the formation of NW-trending Devonian basins and highs (Fossum et al., 2001). In eastern parts of the Barents Sea, transpressional reactivations of faults in Early Carboniferous time initiated the closing of the Uralian Ocean by an eastward subduction (Puchkov, 2002, Cocks and Torsvik, 2006). Subsequent collision between the Siberian plate and Laurussia took place in latest Permian- to earliest Triassic, resulting in the establishment of the supercontinent Laurasia, the Ural mountain chain and the Novaya Zemlya fold-and trust belt in the very eastern parts of the current Barents Sea (e.g. Johansen et al., 1992, Faleide et al., 1993a, Otto and Bailey, 1995, Cocks and Torsvik, 2006). A continuation of the Uralide Orogen northwards into the Barents shelf and eastwards to Taimyr

has been proposed by Gee et al. (2006).

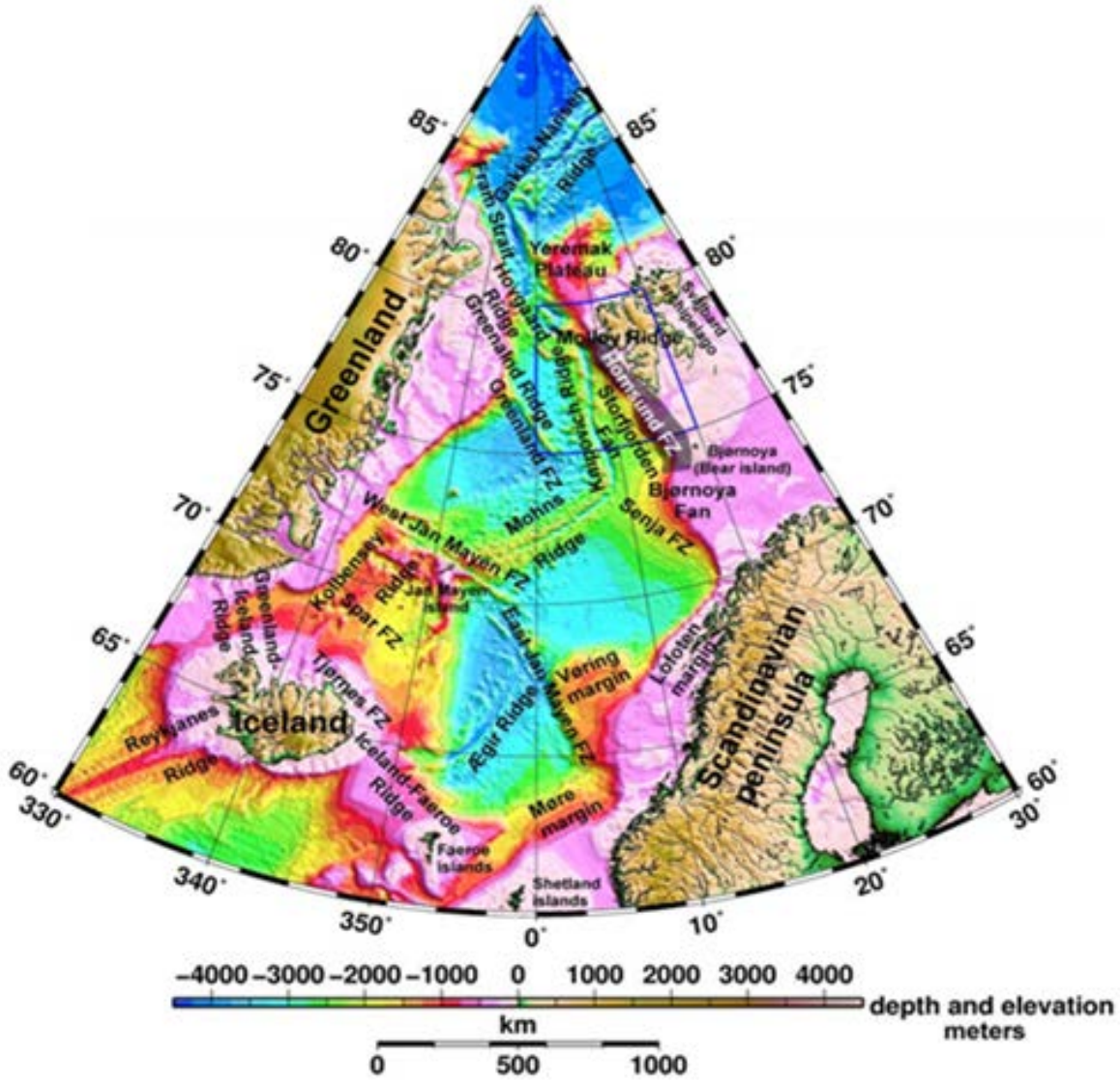

Fig.2.1 - Bathymetric map over present day Norwegian-Greenland Sea and the western Barents Sea, with emphasis on seafloor-features: oceanic ridges; shelf areas; and major fracture zones. (Kandilarov et al., 2008)

2.1.2 Post-orogenic extension- rifting and breakup

The next phase is marked by the transition from a contractional- to a extensional regime, defined by periods of post-orogenic extension (e.g. McClay et al., 1986, Andersen, 1998, Breivik et al., 2005a, Gudlaugsson et al., 1998, Hartz and Andresen, 1997, Doré et al., 1999, Nunns, 1983, Talwani and Eldholm, 1972, Talwani and Eldholm, 1977) eventually resulting in continental breakup between Greenland and Eurasia in Early Eocene (Chron 24B; 53.7 Ma) (Lundin and Doré, 2002). The underlying mechanism behind the orogenic breakup and

associated collapse is controversial, and the hypothesis ranges from the removal of a deep lithospheric root, slab-breakoff, elastic rebound and gravitational drag to pure extensional rifting (Andersen and Jamtveit, 1990, Wilks and Cuthbert, 1994, Hartz and Andresen, 1997, Milnes et al., 1997, Marotta et al., 1998, Schott and Schmeling, 1998, Koyi et al., 1999, Fossen, 2000, Milnes and Koyi, 2000). In the early phase of the intracratonic rifting, the focus of deformation progressively shifted laterally towards the site of breakup, and propagated axially (Doré et al., 1999). Widespread intracratonic rifting was further developed into large-scale basins related to deep-seated sutures (Worsley, 2008). In Jurassic- to Early Cretaceous, the rifting and extension caused considerable thinning of the lithosphere, especially along rift-axis in the North Sea and the mid-Norwegian margin (Gabrielsen et al., 1999). The Icelandic mantle plume was responsible for considerable uplift of the thinned lithosphere around Paleocene (63-62 Ma) (Skogseid et al., 1992, Saunders et al., 1997, Mjelde et al., 1998). By Late Cretaceous, the area between Norway and Greenland had become an epicontinental sea (Doré, 1991).

In contrast to the mid-Norwegian margin which experienced overall rifting, the western Barents Sea was deformed by transcurrent- to transform movements dominated by asymmetric crustal extension and strike-slip transfer setting, resulting in the formation of regional horst- and graben system, and a 300 km wide fan-shaped arrays of block-faulted basins reactivated along older weakness zones (fault-lineaments) (e.g. Faleide et al., 1993b, Faleide et al., 1993a, Faleide et al., 2008, Faleide et al., 1984, Johansen et al., 1992, Gudlaugsson et al., 1998, Dengo and Røssland, 1992, Worsley, 2008). Several basins in the western Barents Sea were initiated at this time (Gudlaugsson et al., 1998) such as the Tromsø, Nordkapp and Hammerfest Basins. The eastern Barents Sea shows little evidence of tectonic activity during the same period, and was mainly subjected to overall regional subsidence until Late Devonian to Early Carboniferous (Johansen et al., 1992), when major rifting coeval with basaltic volcanism in southeastern parts of the region occurred (Drachev et al., 2010). Sediments from Carboniferous to Early Permian differs from west to east (Gudlaugsson et al., 1998). Thick carbonate successions dominates the eastern Barents shelf indicating the presence of a shallow-marine environment ; whereas continental siliclastic deposits dominates in the west (Gudlaugsson et al., 1998). Overlying salt deposits has been proposed to mark the change from rifting to the beginning of thermal subsidence and the development of regional sag-basins affecting the entire Barents shelf in late Carboniferous to Early Permian (Dengo and Røssland, 1992, Gudlaugsson et al., 1998).

In early Permian time, a widespread carbonate shelf was established in the west (especially prominent on the Bjarmeland and Finnmark Platform); while the east was confined to semi-enclosed basins with deposition of shales and carbonate mudstones. As the regional sag continued, the basins formed dissected mosaics of shallow basins and highs (Stemmerik and Worsley, 2005). Doré (1991) suggests that the belt of structural highs that can be observed across the Central Barents Platform represent a northeasterly extension of Late Palaeozoic Atlantic rift which separates the western Barents region from the eastern Barents region. In late Permian, a major transgression occurred, leading to deposition of shallow- to deep-marine sediments across the entire shelf area (Worsley et al., 2006, Smelror et al., 2009). In the transition from Permian- to Early Triassic, the Uralien Sea was closed, and as a consequence, the Barents shelf were placed in a distal foreland position relative to the Ural Mountains. Increased sediment loading in the basins reactivated older normal faults due to the overburden, accompanied by local development of basement-detached normal faults which caused withdrawal of salt (Dengo and Røssland, 1992, Gabrielsen et al., 1992, Nilsen et al., 1995).

In Triassic, the rapid subsidence continued throughout the whole period, especially localized in southern and eastern Barents shelf areas where the Triassic strata range from 4-7 km thickness (Ritzmann and Faleide, 2009). For the eastern shelf, the area was tectonically passive, and was mainly affected by local subsidence. The exception is the faulting taking place at Loppa high, and Bjarmeland- and Finnmark Platforms which was uplifted and subsequently eroded due to sub-aerial exposure - forming a regional unconformity between Permian and Triassic sediments (Ziegler, 1988, Gabrielsen et al., 1990, Smelror et al., 2009). In the Nordkapp Basin and the Tiddlybanken Basin, halokinetic movements of Late Paleozoic salt was initiated in Early Triassic times resulting in large salt diapirs (Nilsen et al.1995). In Middle- to Late Triassic, a marine transgression resulted in the development of an extensive regional coastal flood plain area (Smelror et al., 2009) with deposition of thick units of deltaic sandstones sourced from the Fennoscandian hinterland (Henriksen et al., 2011). The Triassic succession (Induan – Early Norian) is in general around 2500 m thick, comprised of regressive-transgressive cycles (parasequence) and can be recognized in seismic based on characteristic large-scale clinoforms.

In Jurassic, block faulting occurred in western Barents Sea, terminating in the formation of major basins and highs in late Jurassic (Gabrielsen et al., 1990); whereas the subsidence-rate decrease in central parts of eastern Barents Sea megabasin. In mid Jurassic, uplift caused regression and consequent sub-aerial erosion in the central and western Barents Sea. The marine environments were restricted to eastern and western areas in this period (Drachev et al., 2010), but was followed by a transgression that reached its maximum in Late Jurassic, when an extensive marine shelf established (Johansen et al., 1992). In late Jurassic, magmatic activity was accompanied with uplift in the north; and subsequent breakup and opening of the present polar Euramerica Basin (Worsley et al., 2006). Simultaneously, organic rich sediment accumulated in the east Barents Sea (Drachev et al., 2010). The Jurassic strata (Early Norian – Bajocian) shows a thickness ranging from 100 m or less across the Bjarmeland and Finnmark Platforms, to around 300 m thickness in the adjacent Nordkapp Basin.

In Cretaceous, the western Barents Sea experienced extensive rifting and subsequent subsidence that was delimited from the rest of the Barents shelf (Smelror et al., 2009). A possible basin-inversion also took place (Johansen et al., 1992). For eastern parts of the shelf, no major plate-tectonic movements occurred, and it was instead subjected to moderate sedimentation-rates and basin-subsidence (Johansen et al., 1992). The Barents shelf was at this time an open shelf, with structural highs and platforms separating the basins (Smelror et al., 2009). By mid-Cretaceous, The Amerasia Basin in the Arctic Ocean opened, causing uplift and gentle tilting in northern parts of the Barents-Kara region, having a big impact on the sediment-supply for the surrounding areas (Smelror et al., 2009, Johansen et al., 1992). In the northwestern corner of the shelf, vertical tectonic movements was accompanied by volcanic activity associated with Large Igneous Provinces (LIP) linking Greenland, Svalbard, Franz-Josef Land and adjacent shelf areas (Grogan et al., 2000) just prior to continental breakup located in the Amundsen Basin in late Cretaceous (Faleide et al., 2008).

2.1.3 Sea-floor spreading

The last phase represents a period of active seafloor spreading and the generation of oceanic crust across the Jan Mayen and the Greenland-Senja fracture-zone transecting the Norwegian-Greenland Sea (Fig.2.1). The seafloor spreading spans from early Eocene to present day (Chron 24B; 57 Ma – present day) (Fig 2.2) (Eldholm et al., 1987, Eldholm et al., 1989,

Lundin and Doré, 2002, Talwani and Eldholm, 1977) and is characterized by two major plate-tectonic evolutionary phases and local migration of the plate boundary (Talwani and Eldholm, 1977, Nunns and Peacock, 1983, Myhre et al., 1982):

The first phase is set between early Eocene (Chron 24 B; 53.7 Ma) to early Oligocene (Fig.2.2 b) (Chron 13; 35 Ma) (Fig.2.2 a, b) (Lundin and Doré, 2002) and comprises the early initiation of seafloor-spreading of the Norwegian-Greenland Sea. The seafloor spreading in this period occurred along the Aegir and Mohns ridges, coupled to the Gakkel Ridge along the continental transform De Geer zone, composed of the Senja, Greenland and Hornsund fracture zones (Faleide et al., 2008). The direction of the seafloor-spreading axis was in general oriented north-northeast as the Greenland-plate drifted apart from the Eurasian plate. A distinction can be made from the symmetrical seafloor spreading occurring along the Mohns ridge in central parts of the Norwegian-Greenland Sea, experiencing only minor offsets along its strike subsequently to Chron 23 (Hagevang et al., 1983); compared to the region north of Jan-Mayen and Greenland fracture zone which experienced obliquely seafloor-spreading and the formation of sheared- and rotated margin blocks (Talwani and Eldholm, 1977)

The second phase is set between Chron 13 (35.5 Ma) - to present day (Fig.2.2 c, d) and is defined by a major plate-reorganization as the seafloor-spreading between Greenland and Eurasia experienced a counter-clockwise pole-rotation of 30 °, as the axis of seafloor-spreading changed from north-northwest- to northwest-southeast orientation (Lundin and Doré, 2002). This event is related to the suturing of Greenland and the North American plate (Kristoffersen and Talwani, 1977, Srivastava, 1978). Based on magnetic data from the Norwegian Geological survey (NGU) along the Knipovich Ridge (Olesen et al., 1997); Lundin and Doré (2002) suggests that seafloor spreading north of 74° mainly was formed after Chron 13. A complete separation of the Jan Mayen Ridge from Greenland took place just prior to Chron 6 (20 Ma) (Eldholm et al., 1987) as the spreading-axis migrated westward. From Oligocene to Present, the opening continued in a northwest-southeast direction.

The evolution of the Barents shelf in Cenozoic was dominated by a continuation of the basin-subsidence from Neogene and Quaternary to the west, opposed to eastern and northern parts which experienced isostatic rebound and consequent uplift. Due to the elevation differences that arose between the areas, large amounts of Cretaceous sediments where displaced from east and north to the west. (Johansen et al., 1992, Smelror et al., 2009). Faleide et al. (1996b) and Ryseth et al. (2003) reports the erosion to exceed 1 km for several

localities, with a general trend of a more comprehensive erosion towards north. Estimates shows erosion of more than 1 km in the southern Barents Sea (Nøttvedt et al., 1988, Vorren et al., 1988, Vorren et al., 1991), to 2-3 km in the Svalbard area (Eiken and Austegard, 1987, Vorren et al., 1991, Vorren et al., 1988). The late Cenozoic erosion was caused by a global lowering of the base-level due to the combined effect of glacio-eustatic and glacial erosion by marine ice sheets (Vågnes et al., 1992). In Paleogene- to Neogene, compressive deformation associated with a dextral stress fields developed the Spitsbergen Fold- and-Thrust Belt (Eldholm et al., 1987, Saalmann and Thiedig, 2001). Sparse evidence for this compression is evident from the eastern shelf area (Smelror et al., 2009, Otto and Bailey, 1995). From mid Miocene- to present, the western Barents Sea has been regionally uplifted (Dengo and Røssland, 1992), with large influx of Neogene deposits dominated by thick clastic wedges sourced by glacial erosion and subsequent deglaciation (Worsley et al., 2006).

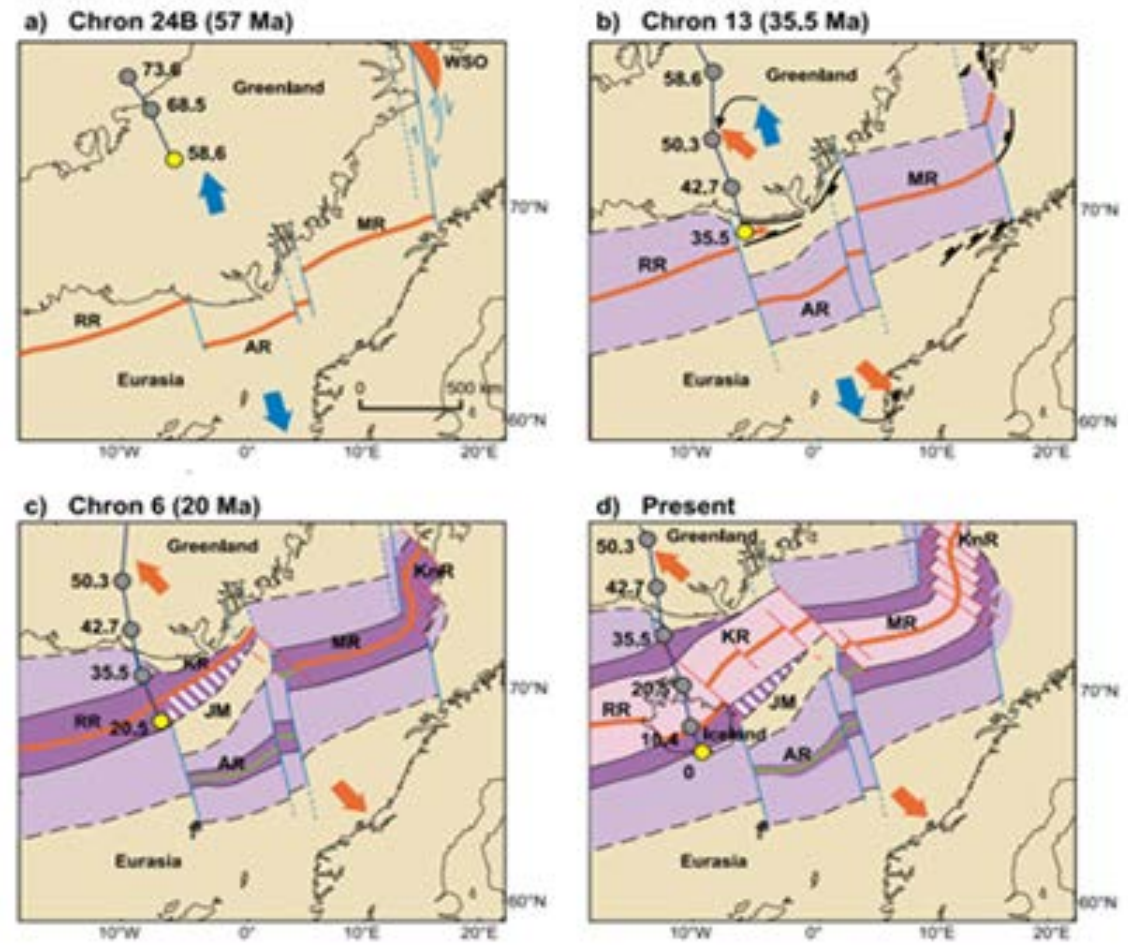

Fig.2.2 *– Reconstruction of the Cenozoic sea-floor spreading between the Norwegian-Greenland Sea and the Barents Sea. a) Initiation of early seafloor spreading; b) major plate reorganization as Greenland and the N. American plate collides; c) the Jan Mayen micro continent is separated from East Greenland; d) present day situation. Legend and abbreviations: Blue arrows - spreading direction pre-dating Chron 13; orange arrows –*

spreading direction post-dating Chron 13; AR - Aegir Ridge; JM - Jan Mayen; KnR- Knipovich Ridge; KR - Kolbeinsey Ridge; MR - Mohns Ridge; RR - Reykjanes Ridge; WSO - West Spitsbergen Orogeny. (Lundin and Doré, 2002)

2.2 Regional setting of the greater Barents Sea

The Barents Sea is a wide pericontinental (and epicontinental) sea covering a total area of about 1.3 million km^2 and is located in the northern European arctic between 70°- 82° N (Faleide et al., 2008). The shelf-area is confined to the continent-ocean transition (COT) in the west, to the Svalbard archipelago in the northwestern corner, the Artic Gakkel Seam margin in the north, the Franz Josef Land archipelago in the northeastern corner, the Kola Peninsula and the Pechora Basin in the south and the Novaya Zemlaya in the east (Fig.2.3 for overview) (Faleide et al., 1984, Gac et al., 2012). The Barents margin is mainly characterized as a passive sheared non-volcanic margin, and is structurally segmented from the mainly rifted volcanic offshore mid-Norwegian margin located between 62°- 70° N (Faleide et al., 2008); and by the passive Eurasian Basin in the north. Regional structures include complex features such as platform areas, and basement highs and lows (Fig. 2.3 for overview) representing the final product of a multiphase geodynamic evolution, developed throughout the following sequence of events: (1) the Timanian, (2) the Caledonian and (3) the Uralian orogenies; (4) the proto-Atlantic rifting episodes (mainly affecting the western shelf-area); and (5) the subsequent breakup and opening of the northern Atlantic (mainly affecting the western shelf area) (e.g. Fichler et al., 1997, Johansen et al., 1992, Gudlaugsson et al., 1998, Henriksen et al., 2011, Doré, 1991).

2.2.1 Geological provinces

The Barents Sea shelf can be divided into two distinct regions: the eastern shelf; and the western region (Fig. 2.4) (e.g. Henriksen et al., 2011). The regions differs from each other with respect to physiographic characteristics of the basement and sediment distribution (e.g. Fichler et al., 1997, Johansen et al., 1992, Gramberg et al., 2001, Drachev et al., 2010) and tectonic evolution (e.g. Smelror et al., 2009, Henriksen et al., 2011, Ziegler, 1988, Gabrielsen et al., 1990, Johansen et al., 1992, Breivik et al., 2005b, Gee, 2004, Torsvik and Andersen, 2002, Drachev et al., 2010).

2.2.1.1 West Barents Province

The western shelf-area is predominantly a transform margin which architecturally was greatly affected by the continental breakup along the dextral transform De Geer megashear zone in early Cenozoic; subsequently evolving into the obliquely spreading Knipovich Ridge (Engen et al., 2008, Faleide et al., 1993a). The province is characterized by small basins and highs, shallow and widespread platform areas with narrow grabens and half-grabens (e.g. Faleide et al., 1991a, Faleide et al., 1993a, Gudlaugsson et al., 1998, Gabrielsen et al., 1990, Faleide et al., 1996a) and thick units of well-preserved Palaeogene-Neogene deposits which oppose the situation in the eastern province (Smelror et al., 2009). Gravity measurements across the western province (Henriksen et al., 2011) shows a mainly high-gravity field which coincide with a north-northeast oriented Caledonian arm representing an offshore-extension of the Barents Sea Caledonides (e.g. Roberts and Olovyanishnikov, 2004, Gee et al., 2008, Breivik et al., 2002). Evidence of dominant north-east striking structural trends in the southwestern Barents Sea (e.g., Troms-Finnmark and Nysleppen fault complex) aligned with onshore Caledonian trends, support this idea (Rønnevik and Jacobsen, 1984, Faleide et al., 1984, Ronnevik et al., 1982, Dengo and Røssland, 1992). Structurally, the Barents Sea shelf is dominated by ENE-WSW to NE-SW and NNE-SSW to NNW-SSE trends (Gabrielsen et al., 1990). The Moho depth in the southwest is typically between 20 and 25 km, clearly different from the +30 km deep Moho east of the province (Faleide et al., 1991b, Jackson et al., 1990)

2.2.1.2 East Barents Province

The eastern shelf-area is characterized by ultradeep- broad and elongated megabasins trending north-northeast, and is comprised of the South- and the North Barents Basins (Gramberg, 1988, Doré, 1991, Johansen et al., 1992, Verba et al., 1992, Henriksen et al., 2011, Vågnes et al., 1992); collectively referred to as the East Barents Basin (Gac et al., 2012). Main geological events affecting the East Barents Sea region includes (1) the west-ward subduction along East Barents Sea shelf in Middle Devonian (Ziegler, 1988); (2) the back-arch extension followed by syn-rift magmatism in Late Devonian (Nikishin et al., 1996, Petrov et al., 2008); (3) the closure of the Uralien ocean east of Novaya Zemlaya and the orogeny during the collision between the Baltic and Siberian cratons in Permo-Triassic (Petrov et al., 2008); and last but not least; (4) the westward thrusting of Novaya Zemlaya in Triassic (Otto and Bailey, 1995).

Today, the basin is in isotatic equilibrium, but a mass excess in the lithosphere is required to explain the 16-20 km thick sedimentary section observed in central parts of the basin (Ebbing et al., 2007, Ritzmann and Faleide, 2009). The sediment cover is comprised of a 5 km thick section of early Paleozoic to mid-Permian sediments (Verba, 1985, Gramberg, 1988, O'Leary et al., 2004); superimposed by a 7 km thick section of late Permian to early Triassic sediment deposited during accelerating subsidence of the basin facilitated by great accommodation space (Johansen et al., 1992, Artyushkov, 2005). Subsequent Neogene uplift resulted in the removal of early Cenozoic sediments; and around 1 km of the Cretaceous cover, leaving a great hiatus to the uppermost layer of Neogene deposits (Johansen et al., 1992). The great subsidence from early Paleozoic- to middle Cretaceous can be explained by three competing hypothesis: (1) densification of the lower crust from metamorphic alteration of gabbro- to eclogite, forced by lithospheric buckling and the formation off overpressure (Artyushkov, 2005, Semprich et al., 2010, Cloetingh and Kooi, 1992); (2) mafic underplating and intrusion of melts (Stel et al., 1993, Naimark and Ismail-Zadeh, 1995, Lobkovsky et al., 1996, Ritzmann and Faleide, 2009); and (3) Permo-Triassic crustal thinning by extension and possibly serpentinization of upper mantle (Ivanova et al., 2006). Gac et al. (2012) suggests scenario two as the most likely and explains that the present-day deep basin geometry is the result of magmatic underplating in Devon induced by rifting and extension followed by an east-west shortening in Permo-Triassic, resulting in densification of the underplated body, thereby increasing the subsidence-rate dramatically.

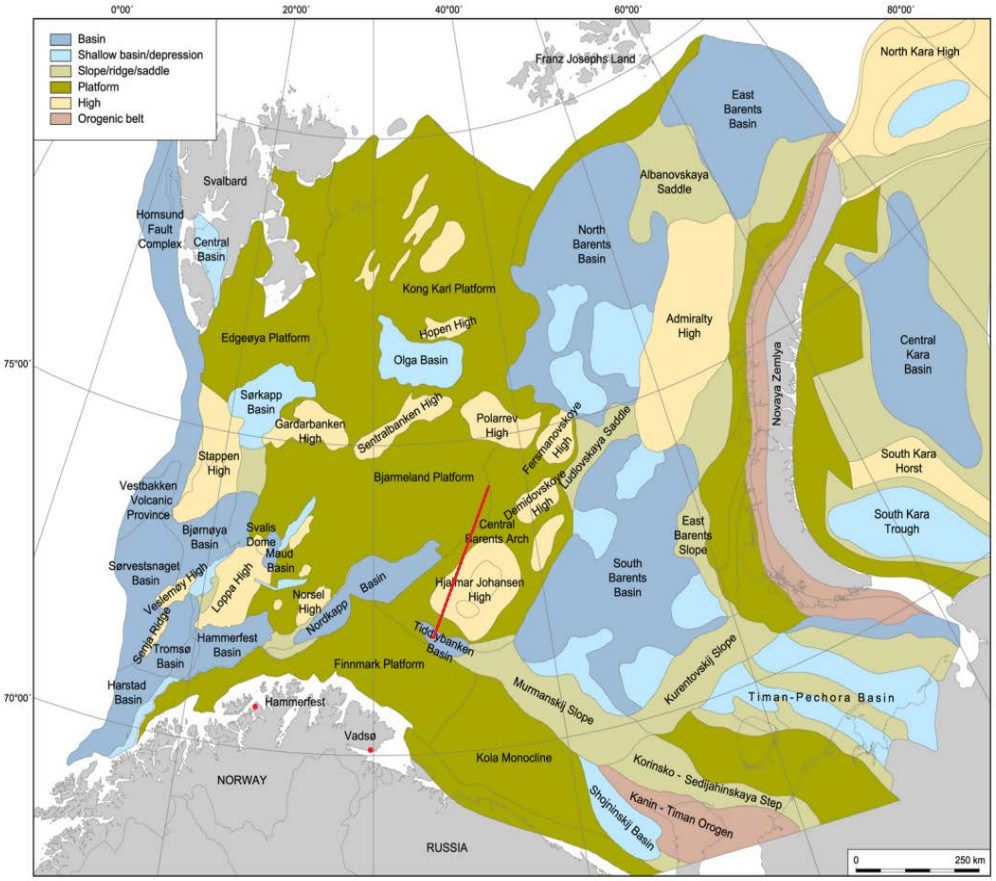

Fig.2.3: Structural elements of the greater Barents Sea. The red line marks the seismic transect related to this thesis. Figure from (Henriksen et al., 2011)

2.2.1.3 The Suture Zone (transition zone)

The western and eastern province is interconnected by a north-northeast trending Suture Zone following the Central Barents Arch/Fersmanovskoye High (Fig. 2.3) (Henriksen et al., 2011). The suture zone is traceable in regional magnetic data, transformed to represent a pseudo-gravity field (Fig. 2.4) (Henriksen et al., 2011): as the western province appears as a high-gravity zone; whereas the east appears as a distinct low-gravity zone. This division of gravity zones represents the general distinction between the highs, platforms and smaller basins to the west and the larger basins to the east (Henriksen et al., 2011).

Ebbing et al. (2007) report that the lithospheric mantle densities also shows regional division between the provinces, ranging from 3250 – 3300 kg m^3 in the west; to 3300-3350 kg m^3 in the east. This observation can possibly reflect the presence of different plates and/-or different lithospheric ages between the provinces; and possibly also reflects the descriptions of a west-trending Caledonian suture in the western province, crossing the entire Barents Sea from south to the north (Breivik et al., 2005a, Gee, 2004). However, lithospheric

density distributions east of the Central Barents transition is inconsistent with this correlation as the suture zone would cross-cut the area of high lithospheric mantle densities (Ebbing et al., 2007). Furthermore, density distribution in lower crust along the suture zone shows relatively high densities. Ebbing et al. (2007) concludes that the suture zone is related to Neoproterozoic Timanide Orogen of Eastern Baltica, as previously inferred by (Gee and Pease, 2004). Such an interpretation would also imply tectonic stability of the Eastern Barents Sea since these times, possibly explaining the presence of the very deep subsidence of the intracratonic basins observed in this region.

Seismic tomography data from Levshin et al. (2007) and Ritzmann and Faleide (2009) indicate slower S-wave velocities of the upper mantle beneath the East Barents Sea compared to the West Barents Sea, indicating a steep deepening of the Lithosphere-Asthenosphere Boundary (LAB) in the Central Barents Sea from West to East. In addition, the Central Barents Sea is marked by a South-North succession of regularly-spaced inverted structures (uplifted domes) such as the Fedinsky High and the Sentralbanken High. The interpretation of recent seismic data in the Central Barents Sea suggests that part of the inversion is contemporaneous with Late-Triassic- to Early Jurassic westwards thrusting of Novaya Zemlya. This suggests that the origin of domes might be linked to compressional events on the eastern side of the Barents Sea. Based on physiographic characterization of the basement-geometry, Johansen et al. (1992) defines the transition zone to be defined by a monocline-structure located within the shallow basement-area; whereas Gee (2004) suggests that the transition should be defined by the shallow basement itself.

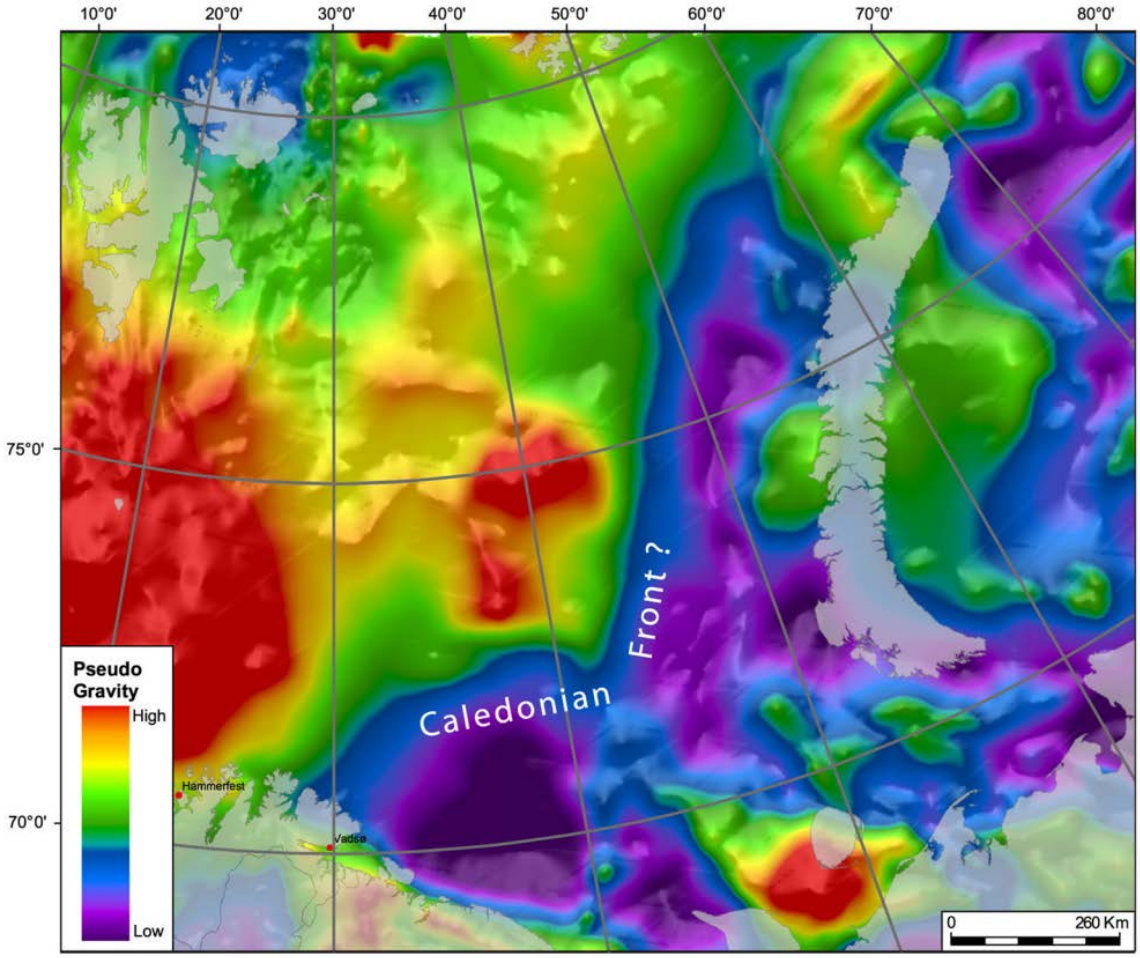

Fig. 2.4: Pseudo-gravity field based on low-frequency magnetic field. A major suture trending north-northeast appears to divide the western and eastern parts of the Barents Sea into two provinces. (Henriksen et al., 2011).

2.3 Barents Sea Southeast- and Central Barents Sea

The geology in Barents Sea southeast is dominated by five large structural elements. In the southern area, the Finnmark Platform abuts the Norwegian coast. In the north, the eastern section of Bjarmeland Platform emerges. In between these platform-areas, the Tiddlybanken- and the Hjalmar Johansen Basins and the Central Barents High are situated at the eastern flank, in approximation to the marine boarder of Russia (Fig. 2.3).

2.3.1 Finnmark Platform

The Finnmark Platform (Sund et al., 1986, Gudlaugsson et al., 1987) is confined by the Caledonides of the Norwegian mainland to the south; and by to the Troms-Finnmark Fault complex and the Nordkapp Basin in the west and northwest respectively. Characteristic features of the platform-sediments are the gently north-dipping strata with progressively older

strata subcrop at the base of the Quaternary (Vorren et al., 1986). Underlying rift-topography with faults blocks contains siliclastic sediments from Early Carboniferous (Larssen et al., 2002). The latest modification of the platform was by differential uplift in Late Tertiary, forming a northward tilt. The boundary between Early Carboniferous to Permian carbonates is interpreted as the transition from a pre-platform to a stabile platform development (Gabrielsen et al., 1990). Paleozoic and Precambrian rocks affected by the Caledonian Orogeny is thought to underlay the platform-sediments (Gabrielsen et al., 1990).

2.3.2 Bjarmeland Platform

The Bjarmeland Platform (Bergsager, 1986) is situated between Hammerfest and Nordkapp Basins to the south and southeast respectively, and the Sentralbanken and Gardarbanken Highs to the north. To the west, it is restricted by the Fingerdjupt Sub-basin and the Loppa High (Gabrielsen et al., 1990). Tertiary uplift caused the platform sediments to dip gently towards the south and progressively older sediments subcrop to the north at the unconformity at the base of the Quaternary (Gabrielsen et al., 1990). Tectonically the area has been stable since Late Palaeozoic. The boundary between Early Carboniferous clastics and Late Carboniferous to Permian carbonates is interpreted as the transition from a pre-platform to a stable platform development (Gabrielsen et al., 1990). The platform area is assumed to be underlain by Palaeozoic and Precambrian rocks like the Finnmark Platform. Pronounced structural highs in the eastern part of the platform existed throughout the Late Permian and Early Triassic, and subsequently evolved into a basin in Late Triassic time (Gabrielsen et al., 1990). The platform is divided into minor highs- and sub-basins characterized by the Svalis Dome.

2.3.3 Tiddlybanken Basin (Varanger Basin)

Tiddlybanken is situated at 72°05’ N, 32°40’ E, and is to date, a relatively unexplored feature. The only certain knowledge is that the basin contain considerable amounts of salt and may have similarities to the Nordkapp Basin (Gabrielsen et al., 1990).

2.3.4 Hjalmar Johansen High (Fedynsky High)

Hjalmar Johansen High or Fedynsky High as the Russians calls it, is an inverted basin which gives rise to gravitational and magnetic anomalies (NPD). The structural high runs in the same direction as the Tiddlybanken Basin, extending westward towards the Nordkapp Basin. In seismic, the area is characterized by extensive erosion of the Cenozoic cover and the presence of a deep graben that cuts into the Carboniferous/ Permian sediments on the Norwegian side (Fig. 2.5).

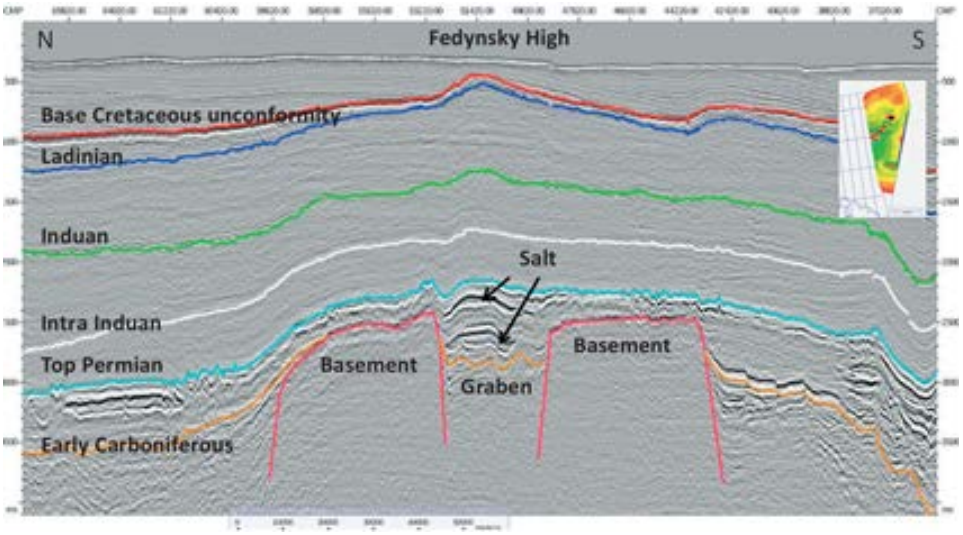

Fig. 2.5: Seismic section from the Bjarmeland Platform (Fedynsky High) showing Carboniferous/Permian graben structure. Figure from NPD's official webpage.

3 Acquisition and processing

3.1 Seismic acquisition

The seismic data was acquired in the period July 27th to August 15th 2012 by the research vessel *Håkon Mosby* managed by the Institute of Marine Research (*IMR*).

3.1.1 Cruise participants

The acquisition was conducted on assignment for the University of Bergen and financially supported by the Norwegian Petroleum Directorate *(NPD).* Collaborating institutes that participated includes the University of Oslo, the Research Center for Marine Geosciences *(GEOMAR)* and the University of Copenhagen.

3.1.2 Seismic source

The seismic source was comprised of a 20 four air-guns source array with a total volume of 78.61 l (4800 inch ^{3}). The shot-point interval was fixed to 200 m and triggered by navigational computer at cruise speed around 4.5 – 5.0 knots, corresponding to approximately one shot per minute intervals. A total of 1601 shots were shot along the transect.

3.1.3 Seismic recorder

The seismic recordings were performed by 20 OBS-stations comprised of a four-component system including three horizontal components (geophones) and one vertical component (hydrophone). The OBS-stations was owned and controlled by the crew from GEOMAR. All stations worked as they should during the acquisition. The hydrophone channel was reported to have consistently higher signal-to-noise ratio then the vertical geophone channel.

In addition to the seismic data, magnetic and gravitationally data were recorded continuously during the survey by a LaCoste-Romberg gravimeter and a Marine Cesium vapor magnetometer.

3.2 Processing of the seismic data

The processing includes a syn-processing step which deals with the navigational data during the acquisition; and a post-processing step which deals with the actual seismic data. The latter is done in order to enhance seismic events of interest from noise, to obtain a better signal-to-noise ratio.

3.2.1 Syn-processing of navigational data

The processing of navigational data was executed
by Dr. Audun Libak (UiB) by use of Python scripts written by head engineer Ole Meyer (UiB). The processing steps include repositioning of the logged UTM position from the GPS antenna to the air-gun location which had an offset of 68 m. This was succeeded by conversion of the corrected UTM coordinates to geographical coordinates. Then, the positioning and geophysical measurements from the Eiva file were linked to obtain accurate timing from the GPS timestamp file. The last step was modifying the UKOOA format file containing navigation-data to make it SEG-Y compatible.

3.2.2 Post-processing of OBS-data

The primary objective for wide-angle data is to determine the velocity structure of the crust and upper mantle. Therefore, analyses of wide-angle data typically only include minimal amounts of data-processing, allowing for easier picking of arrival-times from the seismograms. Most commonly applied is bandpass-filtering, velocity (frequency-wave number) filtering, trace summing, and deconvolution in order to attenuate incoherent and coherent noise, and reduce complications from a ringy sources, multiple reflections or previous shot noise (e.g. Nakamura et al., 1987, Christeson et al., 1999).

Dr. Alexey Shulgin (GEOMAR) performed the processing of the OBS-data. The following sequence of processing was applied:

(1) Real time processing: Static time-shift of 3 seconds was applied in order to provide a correct traveltime, as GEOMAR applies a static shift of 3 seconds when the traces are

cut out from the OBS records. Some timing issues resulting in a shift of 60 ms for all data were also corrected for.

(2) Relocation of the OBS. The direct water wave is used to obtain the correct location of the OBS on the seafloor. This takes into account the drift of the station due to currents from the release point recorded with ship navigation.

(3) Applying distance dependent band-pass filter (lower bandpass frequency window with offset increase). Undesired frequencies are attenuated or removed by using a band.pass filter. The seismic signal recorded by the OBSs has most of its power in the 2-20 Hz frequency band; whereas Fourier Transformation of the data shows that noise is found in the 0-0.8 Hz frequency band. The bandpass parameters where set to 2, 5, 15 and 20 Hz respectively, defined by trapezoid shape, and sine tapered edges with intention to minimize ringing caused by sharp corners in the filter (Gibbs phenomenon)

(4) Normalization of the amplitude of the maximum amplitude within the window. Deconvolution is applied to minimize the effect of water bubble reverberations. Predictive deconvolution is a processing-toll that decreases ringing, which may mask later arrivals. Seismic phases that originally were hard to identify may be enhanced this way. Spiking deconvolution with correlation window set to xxx gave the best results.

(5) Post processing in Seismic Unix (Murillo and Bell, 1999).
The first step in Seismic Unix is to apply velocity reduction. Velocity reduction enhances certain refracted phases with specific velocities (apparent dip) in order for better- or more appropriately presentation in the graphical time-distance plot (seismogram), as the transformation simply replaces time on the vertical axis with reduced time:

$$tred = t - \frac{distance(\Delta)}{Vred}$$

On such a plot, the inclination of a specific velocity-value will be horizontal when the velocity of the phase equals the reduction velocity; arrivals with velocities lower than

the reduction velocity will have positive slopes; and phases with greater velocities than the reduction velocity will have negative slopes. Another benefit of applying reduction time is that the space needed to display the seismogram is decreased, as areas without arrivals are removed because traces that have reduced time below zero are deleted.

4 Phase identification and forward-modeling

In the following chapter, the (pre)modeling- and interpretation procedure including software-packages used to construct the final depth-velocity model is described in chronological order. The modeling only includes P-wave arrivals, as S-waves are beyond the scope of this thesis.

4.1 Time-to-depth conversion of MCS-profile in VMODEL

A coincident MCs-profile to the OBS-profile with constraints on the sedimentary cover was provided by the Norwegian Geological Survey in order to construct a starting model. The profile contained data on layer thickness given in two way traveltime (TWT) and the velocity at each successive interface (upper- and lower boundary). These data were plotted in VMODEL which is part of the RAYINVR-package written by Zelt and Smith (1992) and Zelt and Ellis (1988). Associated software-manual is provided in (Zelt, 1993). By running VMODEL, the data given from the MCS-profile is converted from the time-domain- to the depth-domain. The resulting profile is displayed in Fig. 4.1.

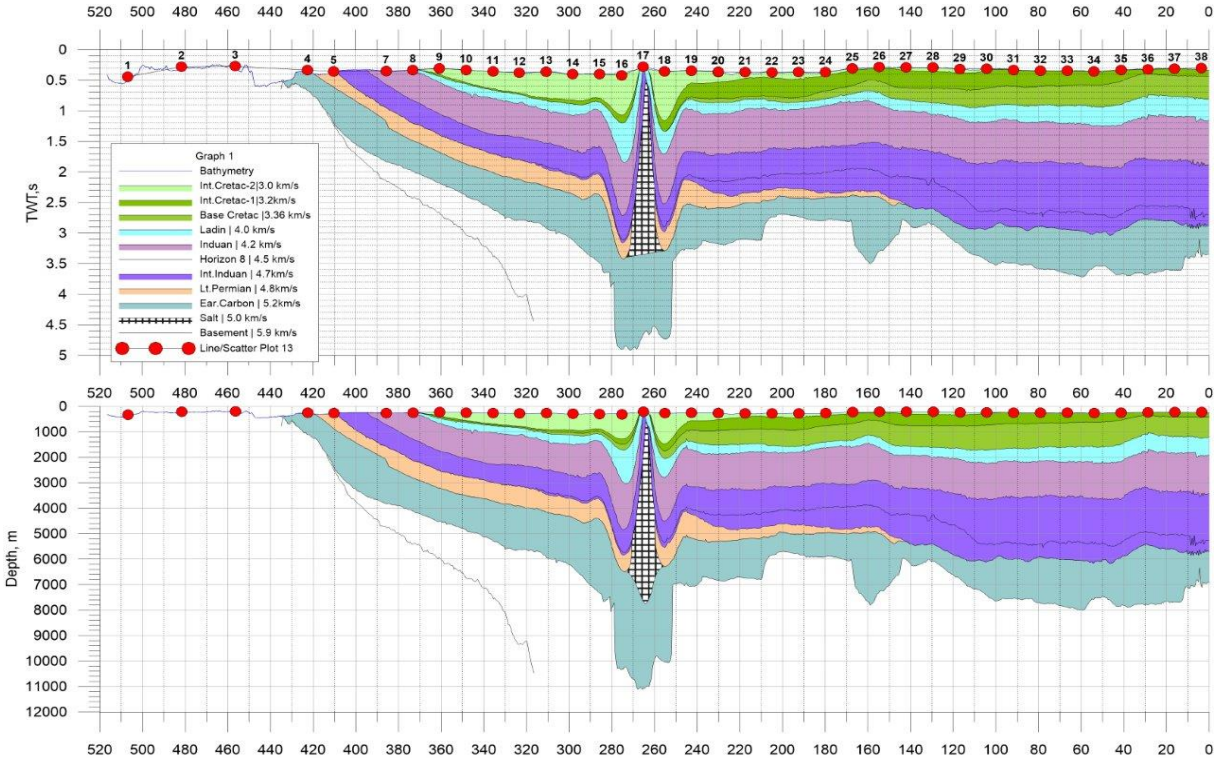

Fig. 4.1 - Multi-channel seismic profile converted from TWT (s) - to depth (m). Seismic data was provided by NPD.

4.2 Phase identification and interpretation in ZPLOT

The interpretation of seismic phases was executed in the interactive plotting and picking program ZPLOT (part of the RAYINVR-package) which display the seismogram as a wiggle-plot. Main features in this program include plotting in reduced time vs offset, applying bandpass-filter from the seismic processing-stage, and fully automated picking. The latter should be avoided because of low accuracy related to spatial aliasing noise, weak signals contained in large amplitude coda and waveform changes over large offset range (Zelt, 1999).

The interpretation of seismic events in ZPLOT was performed with certain guidelines in mind. First of all, all individual phases were picked at the zero-phase wavelet, with respect to the deconvolution performed in the processing; and to provide coherent interpretation of the arrival-times.

4.2.1 Refraction events

Refraction arrivals are in general picked as first arrivals after it overtakes the direct ray at cross over distance, and are recognized as straight lines (linear travel-time curves) in the seismogram. Refraction arrivals provide information on the apparent velocity within the individual layers, and the total traveltime of a refracted ray-path can be expressed with Formula 2, where x denotes the total travel-distance of the refracted ray; v1 and v_2 is the velocity in layer one and two respectively; z is the refraction-depth; and cos Θ equals $1 - (v_1^2/v_2^2)^{1/2}$:

$$t = \frac{x}{v2} + \frac{2z\cos\theta}{v1}$$

It is important to stress that the apparent velocity not necessarily represent the true velocity in the layer. This only applies when the bedding is horizontal. If the bedding is down dipping in the direction of the profile, this will produce a more gentle inclination, and the apparent velocity will be higher than the true velocity, and vice versa for the opposite situation (Sheriff and Geldart, 1995).

4.2.2 Reflection events

Reflection arrivals are identified in the seismogram as secondary arrivals, and can be identified by its characteristic hyperbolic moveout geometry (curved paths on t-x- diagrams). By identify reflection events in the seismograms, these events can be used to identify seismic horizons (interfaces), inclinations or offsets in they layering and layer thickness in the modeling.

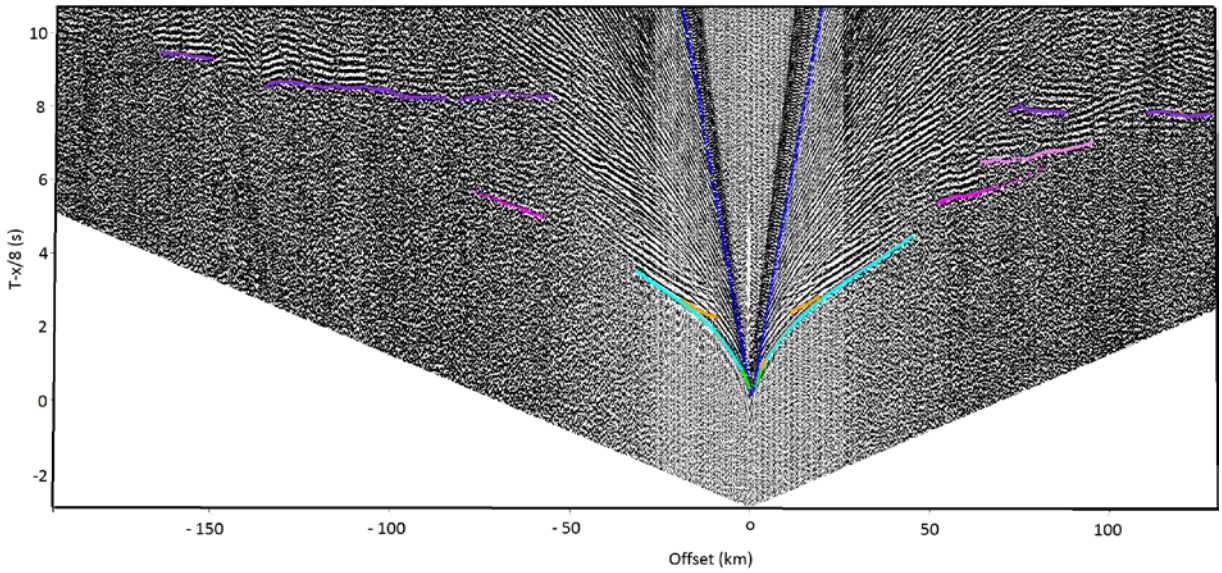

Fig. 4.2 – Picked phases on OBS 28 with bandpass-filter turned on and reduction velocity set to 8 km s^{-1}. The first arrivals marked with green and blue corresponds to refracted phases from the sedimentary cover. The steepening of the curve indicates an increase in the apparent velocity with depth, and was measured to 2.5 km s^{-1} at the bottom to around 5.2 km s^{-1} at the top. The orange color indicates a clear reflection event from the lowermost sedimentary layer. The dark pink phase corresponds to reflections- or possibly refractions from the upper crust; whereas the light pink color corresponds to an intra-crustal reflection. The almost sub-horizontal to horizontal phase in purple correspond to Moho and upper mantle arrivals, with pre-critical reflections at close offsets (±50 to ±90 km), the refracted phase around ±100 to ±130 km offsets and a post-critical reflection between -140 to -160 km. The blue phase corresponds to the direct wave.

4.3 Forward modeling in MacRay

The most efficient modeling method for obtaining 2-D velocity-depth structures of the sedimentary cover, the crust and uppermost mantle from wide-angle seismic data are acquired by ray-tracing software's (e.g. Braile and Smith, 1975, Mooney, 1989, Chulick, 1997, Zelt and Smith, 1992, Zelt, 1999). Ray-tracing software's enables construction of theoretical (synthetic) seismograms, and calculation of travel-times through the layered model.

Subsequently, the theoretical model are compared with observed data (refraction- and wide-angle reflection events) and adjusted until it matches the observed data (Kearey et al., 2009).

The modeling in this thesis was carried out with the interactive 2D seismic raytracing program MacRay written by Luetgert (1992); complemented by the associated software manual Luetgert (1988). MacRay was preferred over the RAYINVR-package, as MacRay provides a more straightforward user-interface were parameters are easily manipulated within the model-window. The drawback in comparison to RAYINVR is that it does not provide inversion-algorithms nor uncertainty calculation to provide estimates on the model non-uniqueness, model parameter resolution and uncertainties (Zelt, 1999).

In MacRay, layers are created from successive interfaces defined by interconnected velocity- and depth nodes that are manually customized to fit the observed data. The depth- and geometry of an interface are manipulated by dragging the individual nodes to new positions in the profile-window; whereas the velocities are interpolated between neighboring nodes, allowing for lateral velocity-gradients to occur across an interface or vertical velocity-gradients through a layer (Luetgert, 1988). This comes in handy in areas with later change in lithology, localized structures or geological features such as salt-domes, or sedimentary basins where variation in layer thickness and compaction from the overburden implies different velocities within the same layer(s). The density of the nodes should be customized in respect to the seismic resolution, data-coverage and structures observed in the seismogram. For areas with complex geology, good quality data and high-resolution one should consider a high concentration of nodes; and vice versa for the opposite situation to prevent over interpretation (Zelt, 1999).

The initial model building started by re-constructing the velocity-depth profile of the sedimentary cover, computed in VMODEL. The lateral sampling-interval (node-space) was set to around 0.5 km. When this was finished, the interpreted seismograms (pickings) were converted to readable file for the MacRay-environment, and the actual modeling could start.

The actual modeling was executed in a layer-stripping way (forward modeling) implying that only one layer should be designed at the time, starting from the very top of the sedimentary cover- and working down to the lowermost upper-mantle arrivals. An interface is adjusted until it gives a good match to the observed data (refraction- and reflection events) through error-and-trial modeling (e.g. Zelt, 1999).

Refractions are the first parameter to be adjusted by assigning a velocity-gradient (upper- and lower velocity) to the layer. The second step is to adjust the layer thickness, geometry and depth position by adjusting it to reflection events (if observed). If step two included modification of the layer geometry, this would affect the steepness of the steepness of the refraction curve, implying a change in the velocity. To correlate for this change, the velocity-gradient has to be double-checked, and changed if the model requires it. When this is done, the refraction event will be correlated to the true velocity of the layer, and the next layer can be modelled, following the same procedure.

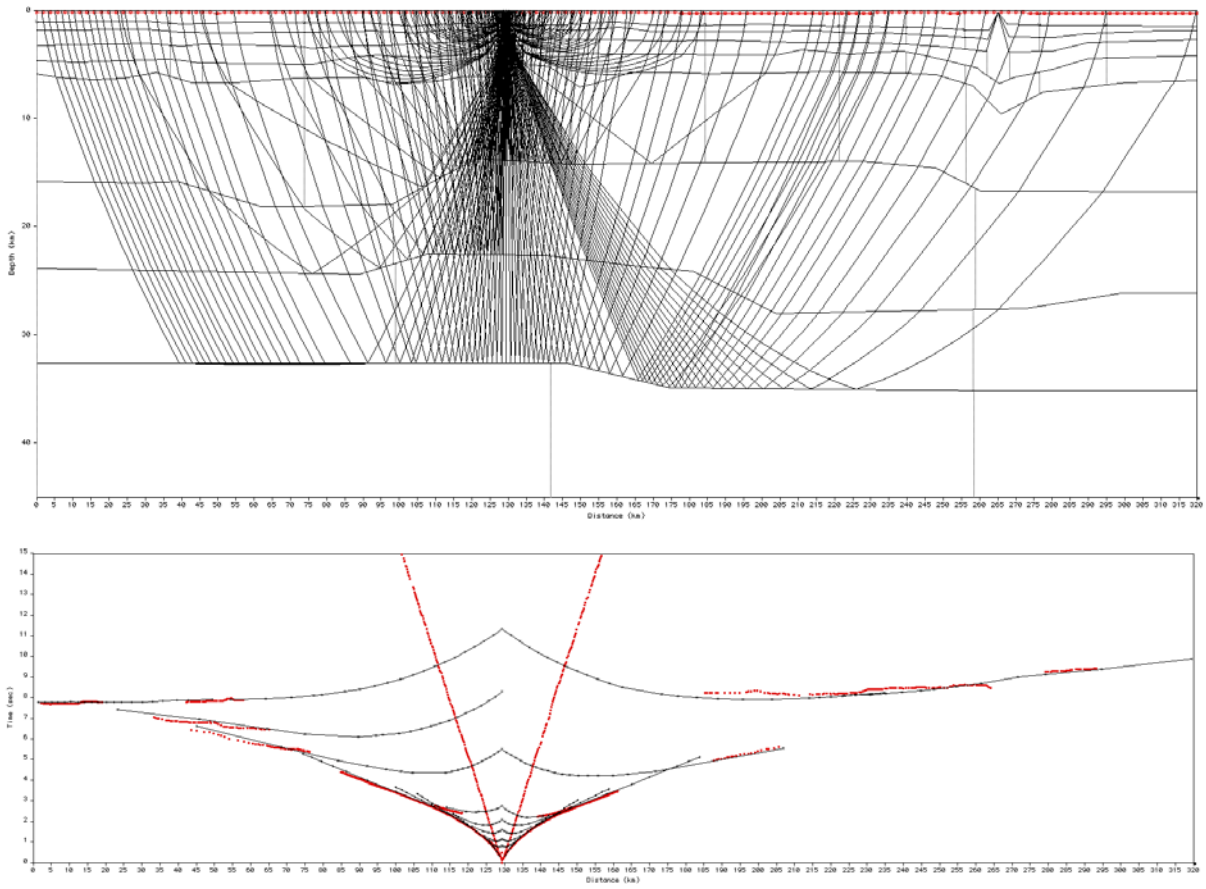

Fig. 4.3 – Raytracing in MacRay for OBS 28. The upper plot shows the ray-path of the synthetic P-waves shoot through the sub-surface of the constructed model. The lower plot shows the fit between the calculated travel-time curves from the upper plot (black lines) and the seismic events that was picked in OBS 28 (red dots). In general, there is a good fit for the sedimentary cover; the geometry of the reflection events from the crust gives a good fit with the model. The Moho arrivals are well-constrained at far offsets, but there is a misfit of around 100 ms at close offset (pre-critical reflections). This misfit can possibly be explained by bad picking as the seismogram was blurry in this specific area due to the overprint of multiples.

5. Results

5.1. Phase picking and identification

Clear arrivals from the sedimentary cover are well recorded on all of the OBS-stations. Arrivals from the upper crystalline crust are often tricky to identify due to the overprint of multiple energy from earlier events; whereas intra-crustal arrivals appears more sporadically and typically as high-amplitude events. The Moho and upper mantle arrivals are recorded on most stations, but was hard to identify on certain seismograms, especially station 20, 21 and 35 which contains poor data on sub-sedimentary structures in general. Examples of recorded sections from the profile are shown in Figures 4.1 – 4.3. For a complete overview of all seismograms, see appendix [A-T]. Table 1 gives an overview of abbreviations used for the seismic events observed in the seismograms.

Table 1 - List of abbreviations for seismic events

P-wave phases	**Symbol**
Sedimentary refractions	P_{s1-6}
Mafic sill refraction	***Ps***
Top basement reflections	***PcP***
Basement (upper crust) refractions	***Pc***
Intra-crustal reflection	P_GP
Moho reflections	P_MP
Upper mantle refractions	***Pn***
Upper mantle reflections	P_FP

5.1.1 Sedimentary phases

Clear and high amplitude refractions from the sedimentary cover (P_{sed}) are observed as first arrivals in the vicinity of shot points up to offsets of 70 km and show an apparent velocity ranging from 2.5 to 5.3 km s^{-1} (Fig. 4.1). Pronounced velocity-breaks that occur along the refracted arrivals reveals that the sedimentary cover can be subdivided into five velocity-intervals that can be laterally correlated across the profile, with the exception of a few stations where the velocity deviate in the order of ± 0.2 km s^{-1}. The following velocity-gradients are observed, assigned with abbreviation from bottom to top: P_{s1} [2.5 – 3.8]; P_{s2} [3.9 – 4.0]; P_{s3} [4.1 – 4.35]; P_{s4} [4.7 - 4.8] and P_{s5} [5.0 – 5.2]. Post-critical (wide-angle) reflection was also observed on most of the stations, and was especially easy to recognize for interface P_{s1} to P_{s2},

P_{s3} to P_{s4} and P_{s4} to P_{s5} (Fig. 4.1). In addition to the five sedimentary phases described above which correlates with velocities given in the NPD-model (Fig. 4.5), one additional layer is included under the definition of the sedimentary layers, and the refracted phase from this layer is referred to as P_{s6} (Fig. 4.2). The apparent velocity of this phase ranges from 5.7 to 6.0 km s^{-1}. This puts it in the very upper velocity-spectrum of meta-sedimentary rocks. The onset of this arrival is well-constrained by strong post-critical reflection (Fig. 4.1) that occurs in almost all of the stations. P_{s6} is characterized by discontinuous, weak and low amplitude arrivals which made it really tricky to pick. Only a few stations (22-25 and 37) provided good enough quality to pick the phase for longer offsets. For this reason, the observed velocity should be applied an uncertainty of around ± 0.2 km s^{-1}. In general, the P_{s6} phase is observed as first arrivals from offsets of 25 km up to 140 km where it terminates in strong reflection events from the Moho (PmP) or upper mantle refractions (Pn) in the time-window between 7 and 8 s (for reduction velocity 8 km s^{-1}). It should be noted that crustal arrivals (both refractions and reflections) possibly might interfere with the P_{s6} phase from offsets around 60-70 km for station 19 – 29, but this is really hard to quantify due to the weak and low amplitude of upper crust arrivals.

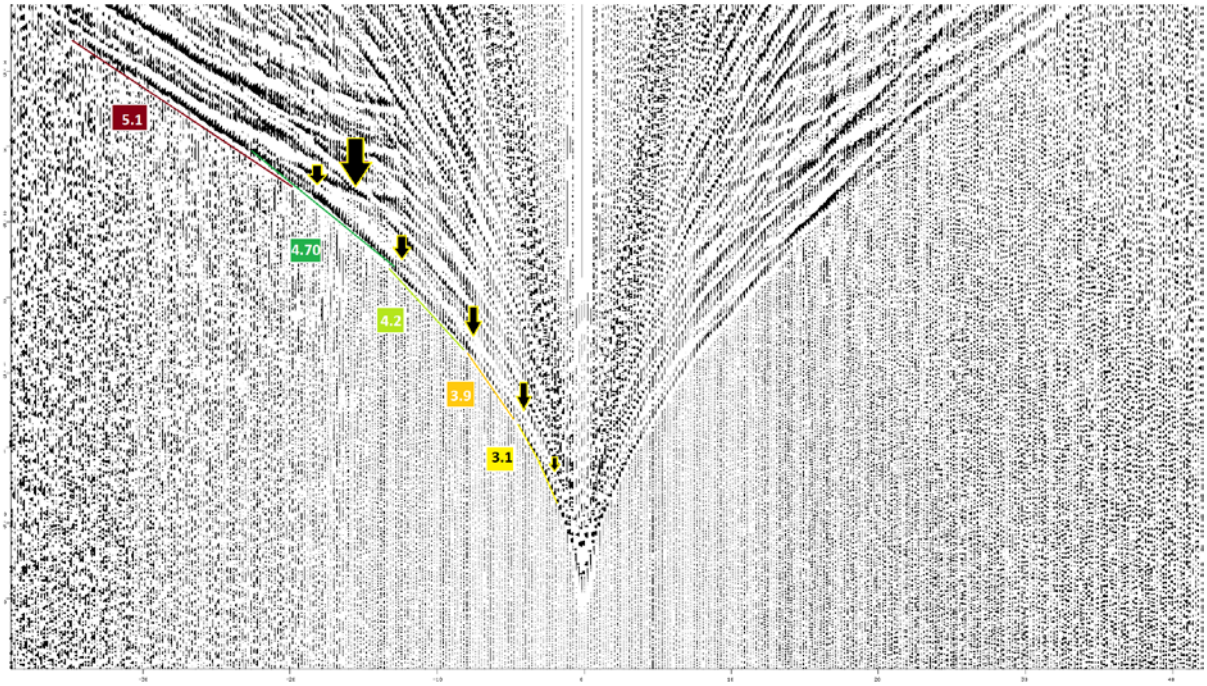

Fig. 4.1 *– A section of the sedimentary phases recorded at OBS 30. The assigned numbers equals the average velocity observed for the different phases. Color codes: yellow (P_{s1}); orange (P_{s2}); light green (P_{s3}); dark green (P_{s4}); and red (P_{s5}). Small arrows indicates the position of post-critical reflections. On this station we can observe reflections from all sedimentary phases, including a possible reflection within P_{s1}. Also note that the different phases show variations in amplitude, making it fairly easy to differentiate the different phases. The big arrow indicate the onset of a new reflection event with much larger amplitude than observed for sedimentary phases below, indicating the transition into a layer with physical properties significantly deviating from the overlaying sediments. This reflection event marks the transition into a high-velocity layer that has been categorized into the meta-sedimentary sequence.*

5.1.2 Crustal phases

The term basement is here used to define the upper crystalline crust that lies below the meta-sedimentary rocks. The top basement reflections (PcP) and the top crust refractions (Pc) are observed at highly varied offsets from 35 km to around 120 km where it intercepts with Moho and/or upper mantle arrivals. The top-crust arrivals were in general difficult to identify in the OBS recordings as they appear masked by multiple energy. This was especially diagnostic at close offsets (30-60 km) where pre-critical reflections are expected. At greater offsets, the recorded section seem to be clearing up a little as wide-angle arrivals are free of many of the interbed multiples and scattered energy that obscure near vertical incidence data. The best attempts of picking basement reflection events were at stations 19, 24–29, 31-33 and 37. The most prominent basement reflectors was observed at station 28 (Fig. 4.3) and 31 where energy from the sedimentary cover was absent from offsets of 30 km. Strong multiples from the Pc phase seen in Fig. 4.3 gives a good indication of the velocity of the upper crust, which was measured to 6.2 km s^{-1} for this particular station. This value correlates well with other measurements of weak- linear events in the offset range of 50 to 100 km which showed velocities ranging from 6.1 to 6.35 km s^{-1}.

Intra-crustal reflections P_GP from the middle crust are recorded in most of the stations, and are characterized by highly variable amplitude that appear to increase from SSE to NNE across the profile. The pre-critical reflections are the most dominant arrivals from this part of the crust, and are mainly observed at short offset-intervals between 40 km to around 100 km where it intercepts with arrivals from the Moho- or upper mantle. Intra-crustal refraction are hard to identify as it correlates to secondary arrivals, intercepting with refractions from the P_{s6} and/or Pc arrivals at offsets around ±90 to ±120 km. Several measurements of possible refractions were conducted in order to constrain the velocity of the middle crust, but the results showed scattered values in the range of 6.5 to 7.3 km s^{-1}. Regardless of the bad constrain of the refraction events from the middle crust, high-amplitude events along with long offsets of pre-critical reflection indicates that there exist a significant velocity-gap between the layers which can be further examined in the modeling.

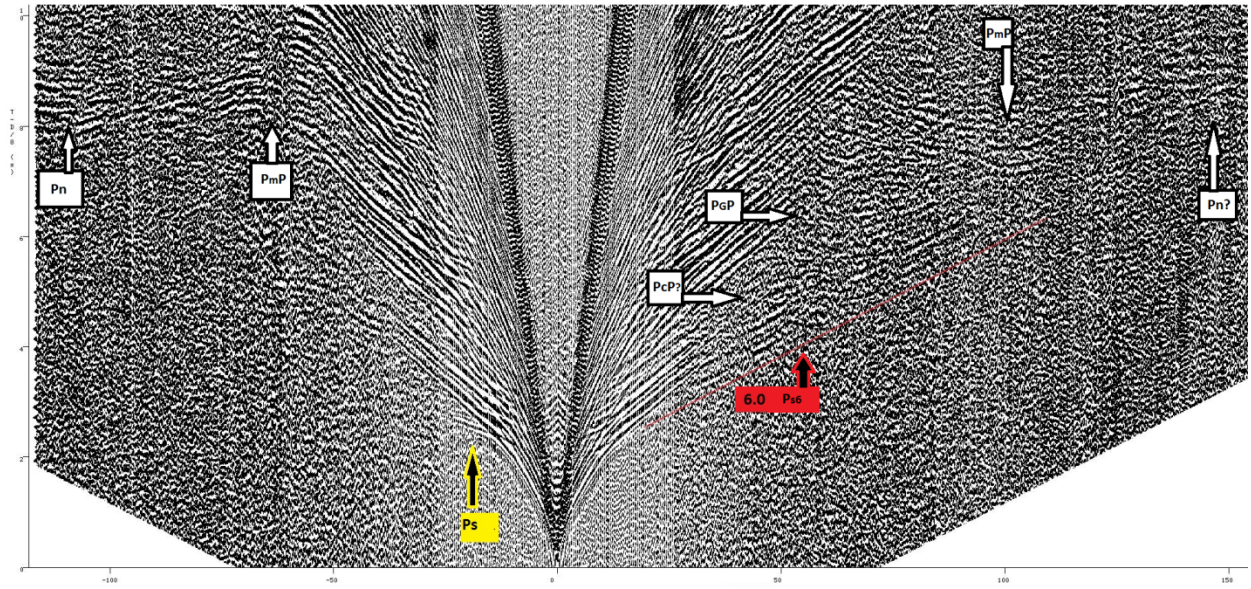

Fig. 4.2 *– A section of the recordings from OBS 22, one of few stations where the refraction phase for the lowermost sedimentary layer (P_{s6}) appears with high amplitude along a clear and continues phase seen at offsets from 25 km to around 125 km. Also note the high-velocity refraction phase (6.7 km s^{-1}) marked in yellow. This is properly a mafic sill (Ps) situated somewhere between interface 5 and 6 in the sedimentary cover. The Top basement reflector (P_cP) is marked with a question mark to illustrate the challenging task of identifying the onset of top basement arrivals, as recordings appears chaotic due to the overprint of multiples. Intra-crustal reflectors (P_GP) on the other hand can be located as multiple energy is attenuated in the section of later arrivals. In the time-window 7-9 s, the chaotic signature appears again, potentially masking Moho reflections (P_MP) and upper mantle refractions (Pn). Fortunately, the high acoustic impedance between the lower crust and the upper mantle produces high amplitude arrivals that stands out from the noise. The sub-horizontal to horizontal moveout geometry for the* P_MP and Pn phases was consistently recognized throughout the profile-length and facilitated the picking.

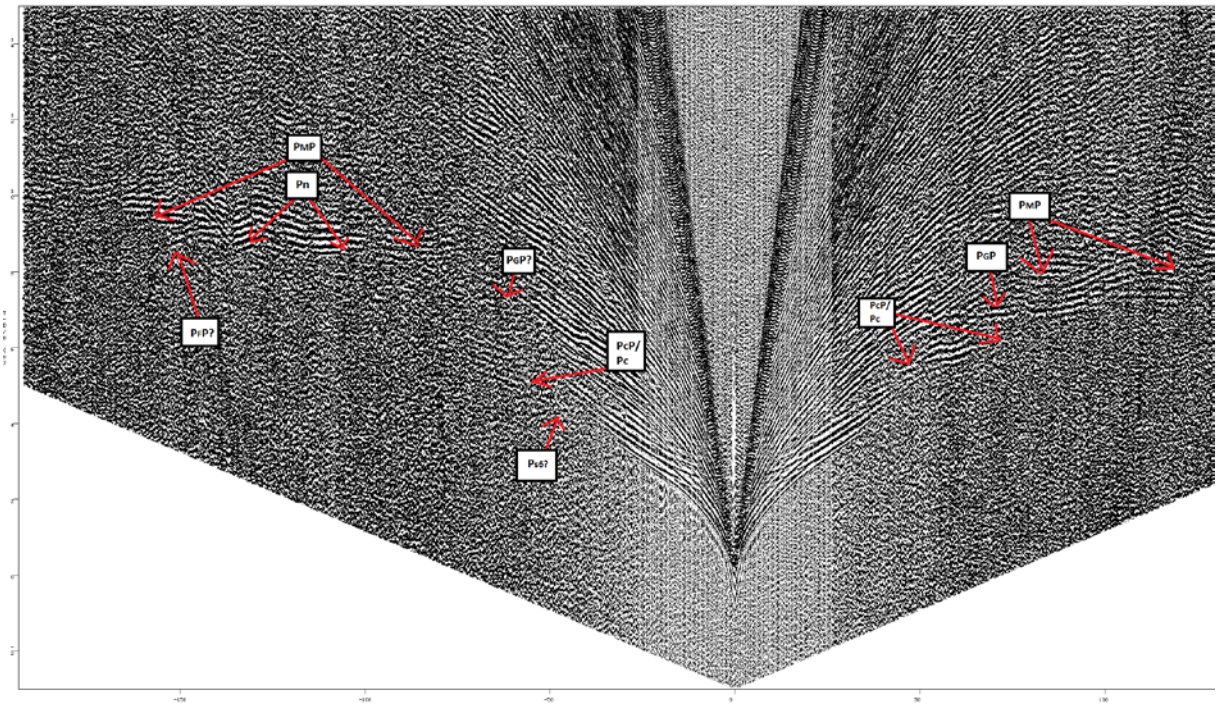

Fig. 4.3 – *Recorded section from OBS 28, one of few stations where the basement reflector (PcP) is easy to identify (right hand side). On the left side, a weak P_{s6} phase seems to merge together with the basement reflection at 60 km offset, implying that a verification of whether we observe the upper crust refraction or the P_{s6} phase at greater offsets can be challenging. Especially since the apparent velocity of the two approximates; and because they don't have any distinctive signature which allows us to distinguish them. Note how the Moho and upper mantle arrivals bends into a concave shape at offset -130 km to -140 km. This feature is caused by a large salt-diapir situated in the Tiddlybanken Basin.*

4.1.3 Moho discontinuity and upper mantle phases

The Moho discontinuity is easily identified in the seismic section on almost all stations as it is characterized by clear- and high amplitude arrivals in the offset range of 80 km to around 170 km (Fig. 4.3). The curvature (normal move-out) for the pre-critical phase (P_MP) and the upper mantle refractions (Pn) are close to horizontal in most recordings, revealing that the Moho should be have a simple- almost flat geometry and/or a uniform velocity around 8 km s^{-1}. The best recordings in this respect are from OBSs 24-28 where the P_MP and the Pn phase are recorded over large portions of the profile [0-125 km] and [200-320 km].

5.2 Synthetized velocity-depth model

A reasonable P-wave velocity-depth model was achieved after several attempts of adjusting the model-parameters to fit the observed data (picked arrivals) from OBS 19-38. The final model (Fig. 5.1) consists of six sedimentary layers, two crystalline crustal layers and the upper part of the uppermost mantle layer.

5.2.1 The sedimentary cover

The sedimentary cover was initially modeled with basis on the MCS data provided by NPD (Fig 4.5 and 5.1). This model divides the sedimentary cover into six distinct stratigraphic megasequences based on unconformities that likely represents velocity discontinuities. The following data was given: The uppermost sedimentary layer consists of Cretaceous sediments with a velocity ranging from 3.0 – 3.36 km s^{-1} and a thickness of around 0.8-1.6 km. The second, third and fourth layer in the sequence are the Ladin (4.0 km s^{-1}) the Induan (4.2 - 4.5 km s^{-1}) and Inter Induan (4.5 – 4.7 km s^{-1}) which corresponds to Middle and Early Triassic sediments. The thickness of these layers range from 0.2-0.8 km, 1.2-1.4 km and 1.8-2.5 km respectively. The fifth layer in the sequence is the Late Permian (4.8 km s^{-1}) that onlaps the Early Carboniferous layer at around 140 km, gradually thickening toward SSW of the profile. The lowermost layer in the sequence is the Early Carboniferous (5.2 km s^{-1}) which shows large variation in thickness (0.8-2.3 km) due to an irregular base-geometry. The thickness of this layer range from 0.8-2.3 km. In addition to the megasequences, a large salt-diapir is present at around 260-270 km. This Salt-diapir intrudes all layers from the bottom of Carbon, almost reaching the top of the seafloor. The velocity of this salt-diapir has been set to 5 km s^{-1}.

The parallel layer-geometry for the five uppermost layers seems to be controlled by the topography of the upper part of the Carboniferous layer. In terms of structures, the five uppermost megasequences can be described fairly simple. From 0-30 km the strata gradually steepens before they drop with approximately 500 m from 30-40 km in the profile. Around 40-120 km in the profile, the layers are relatively flat and close to horizontal before they rise again with approximaly 1000 m from around 120-160 km in the profile. This gradual steepening reflects a general decrease in layer thickness towards SSW. From 160-240 km in the profile, the layers are more or less horizontal, with a gradual downslope towards the salt-diapir where a pronounced drop (2000-3000 m) occurs in all layers. The area behind the salt-diapir (255-320 km) is unconstrained in the OBS-data, as no arrivals from the sedimentary layers are observed beyond this point in the seismograms.

The base of the Carboniferous reveals three basin-shaped areas. From 0-110 km a broad and extensive basin appears. A deep and narrow trough-like feature indicates the presence of a basin from 150-170 km. The area 210-290 km marks the position of the Tiddlybanken Basin.

5.2.1.1 NPD-model vs OBS data.

After constructing the preliminary model of the sedimentary cover from the NPD-model, the layer-thickness, layer geometry and velocity-distribution for the sedimentary megasequences was compared with the picked events from the OBS-data described above. This was done in order to see if the model needed modifications to obtain a better fit to the OBS data (see Fig. 4.4 for comparison). The first change that was applied was a change in the velocity-gradient in the Cretaceous from 3.0 - 3.36 km s^{-1} to 2.5 - 3.8 km s^{-1} as the latter was consistently observed in all seismograms. The layer thickness and the geometry of the base were also slightly modified, as the Cretaceous/Ladin interface could be correlated with strong and clear reflection events.

The Ladin layer had no need for major changes, other than some fine-tuning to compensate for changes performed in the Cretaceous. The same goes for the Induan.

The biggest change in the model is the significant thickness-reduction of the Inter Induan. The thickness of this layer had to be reduced with up to 1.4 km in central parts of the profile as the onset of the P_{s5} (refraction from the Carboniferous) totally missed the picked arrivals from the Carboniferous. From figure 5.4 it can be observed that the base of the Inter Induan probably gives a better fit to Horizon 8, inferred as a velocity-boundary within the Inter Induan. The Permian layer could not be identified in the seismogram, and was for this

reason not included in the model. It is however assumed that Permian layer is modeled as part of the Inter Induan layer due to the similarity in velocity (+ 0.1 km s^{-1}). The thickness and geometry of the Early Carboniferous layer had no need for big modifications except for the area 210-260 km where the pronounced deepening seen in the NPD-model gave no match with picked events from the seismogram, and was consequently modeled with a flat geometry. A refraction with apparent velocity of 6.7 km s^{-1} was observed within the Early Carboniferous layer (Fig. 5.2) in OBS 19-22, and was modeled as a ~200 m thick sill intrusion extending from 235 - 265 km in the final velocity model (Fig. 5.5). The depth position of this sill is properly situated a little deeper, but as it is impossible to create a "floating sill" within a layer, it was modeled as a confined layer between the Early Carboniferous and Inter Induan interface.

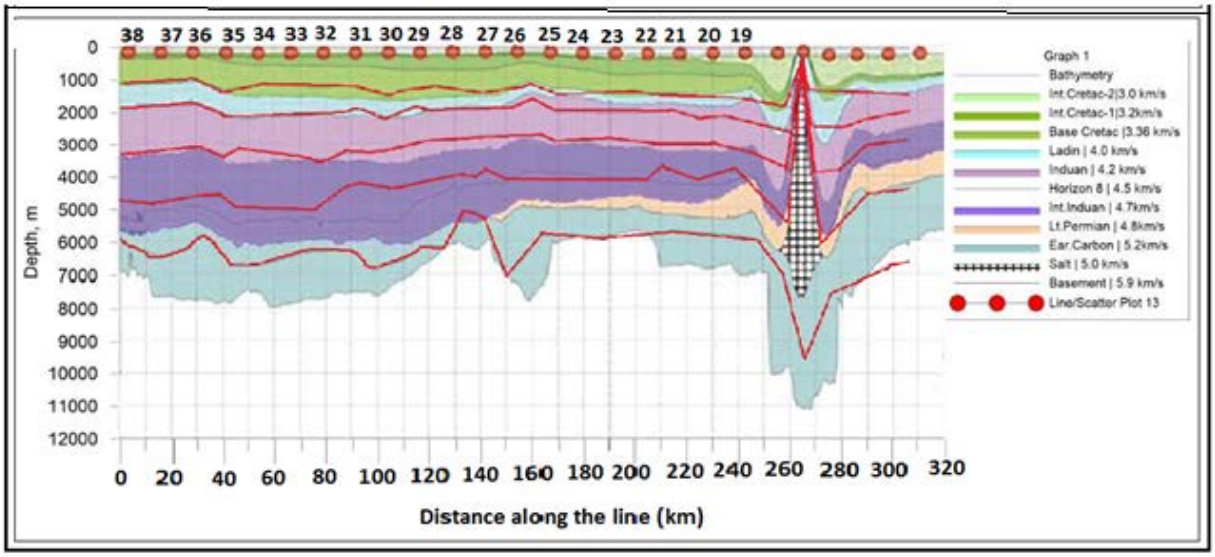

Fig. 5.4 – Depth-converted seismic line provided by NPD overlaid by the sedimentary model build in MacRay (red lines). The biggest modifications from the two are the increased velocity-interval for the cretaceous which was changed from 3.0 – 3.3.6 km s^{-1} – to 2.5 – 3.8 km s^{-1}; and a significant thickness-reduction of the Inter Induan layer with up to 1.2 km.

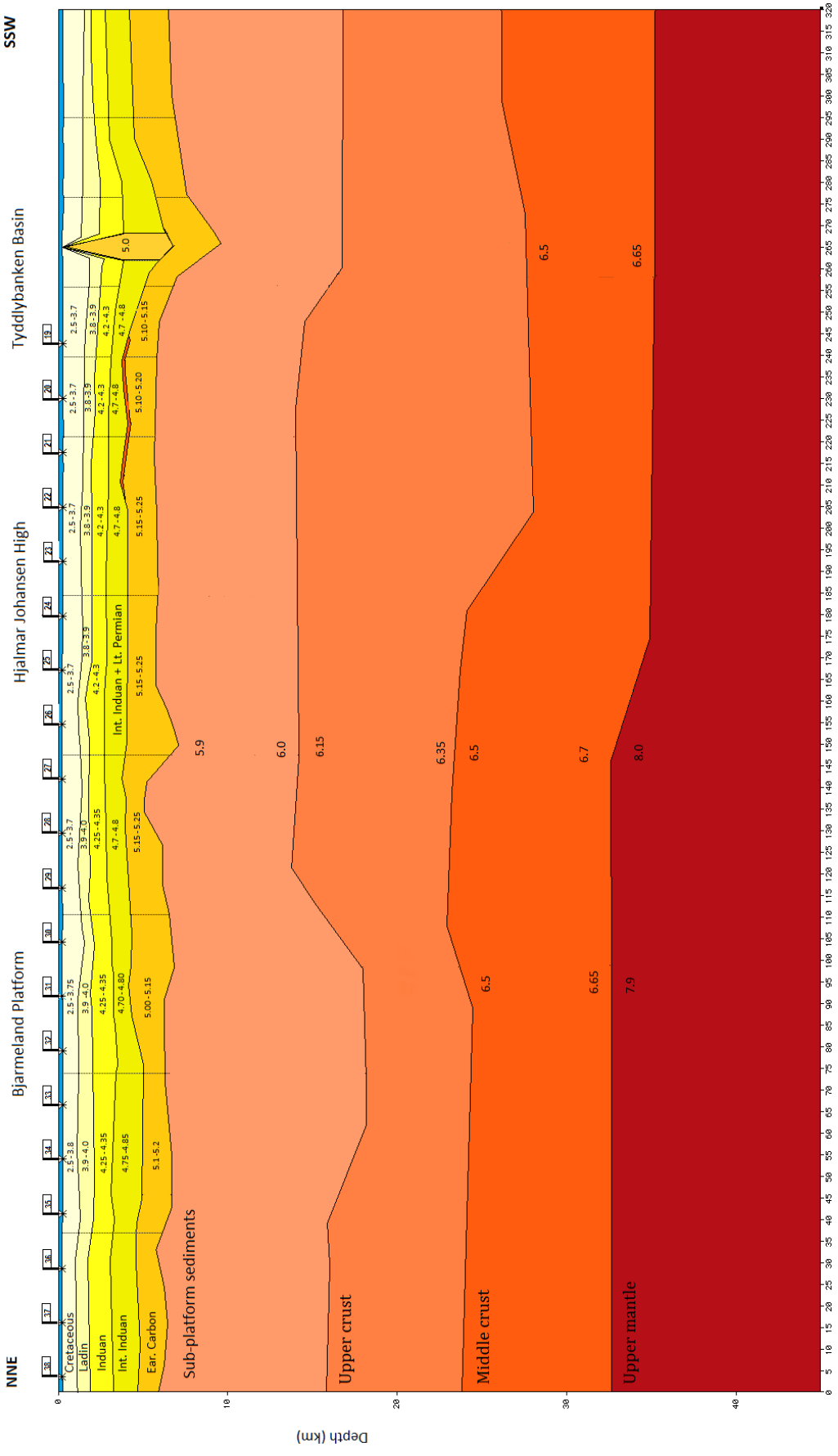

Fig 5.5 - Final velocity model

5.2.2 Sub-platform sediment(s)

The lowermost layer in the sedimentary succession is interpreted as meta-sedimentary rocks belonging to the Riphean complex. This megasequence is characterized by its great thickness varying from 10-11 km in the in the very NNE part of the profile at Bjarmeland Platform, to 7-8 km at Hjalmar Johansen High, and from 8-9 km at the Tiddlybanken Basin area. The velocity-gradient in this layer was modeled to 5.9 – 6.0 km s^{-1} which corresponds to observations described in the section above. As implied, the velocity is constrained from very few arrivals as the refracted phase (P_{s6}) appears sporadically in the seismogram, typically as highly discontinuous events. The velocity-control on this layer is in general fairly low.

During the modeling, MacRay apparently had difficulties to distribute the shot-points evenly across the profile. It turned out that the irregular geometry at the base of the Early Carboniferous acted as a topographical barrier for further migration of the shallow head-waves. This observation can possibly explain the discontinuity of the arrivals in the seismogram.

5.2.3 The upper crust

The crystalline upper crust varies in thickness from 6-13 km and shows a general thickening from NNE towards SSE of the profile, with the thickest section beneath the southern part of the Hjalmar Johansen High. The basement topography varies across the profile and can be categorized into an extremely deep basin area (15-16 km) in the Bjarmeland Platform area where a local depression occurs from 45–90 km. A pronounced upward swallowing trend (~10°) from 95-120 km marks the onset of a topographic high, inferred to represent the northern flank of the Hjalmar Johansen High. This basement high is stabilized at 12 km depth before it drops to around 13-14 km depth in the Tiddlybanken Basin area. In respect to the low resolution of seismic arrivals from the upper crust due to the overprint of multiple energy, the basement-interface has been interpolated between neighboring OBSs where basement arrivals was picked. This leaves great areas unconstrained, and the geometry and depth-position of the basement should be consider a very simplified model.

The interval-velocity of the upper crust has been assigned a gradient of 6.15 – 6.35 km s^{-1} from top to base. This velocity-gradient was used on the basis of the observation discussed in the section above. Such a low velocity contrast between the crystalline crust and the Riphean complex would also explain the lack of reflectivity from the basement.

5.2.4 The middle crust

The middle crust shows an almost uniform thickness of 8-10 km with geometry parallel to the Moho discontinuity. The thickest part of the middle crust is from 105-205 km where the layer has been modeled as topographic high. This area was quite complex to model due to abrupt changes in the dip the pre-critical reflection from the respectable seismograms where the interface was identified for this area. Several geometrical and velocity modification was tested out before it was decided that the geometry seen in Fig. 5.5 gave the overall best fit. A possible explanation for the complexity is the presence of reflectors from other features than the middle crust boundary. This could unfortunately not be tested as floating reflectors can't be created in MacRay.

The slope from180-200 km could possibly be relocated somewhere between 160-200 km as the slope was not covered by seismic arrivals. It had to be put somewhere in this interval because seismic events in the area SSW of 220 km gave a fit with a drop in the elevation of about 3.5–4.5 km.

The velocity-interval of the middle crust is set to 6.5 – 6.7 km s^{-1} as the high amplitude and long offset of pre-critical reflections implies a large difference in the velocity of the layers. The velocity could possibly be even higher but is hard to constrain without refractions. Lateral velocity-gradients could possibly also be introduced as the amplitude of the arrivals appeared highly variable across the profile, but the lack in consistency between neighboring OBSs made it hard to correlate over distance. It was therefore decided to keep the layer simple to prevent over-interpreting.

5.2.5 The Moho- and upper mantle

The Moho discontinuity is modeled to depth-position of 32 km from 0-145 km. A downslope appears from 145-175 km where the elevation of the Moho drops to 34 km depth. From 170-320 km the geometry of the Moho discontinuity is flat and horizontal.

The velocity of the upper mantle is well-constrained from clear refraction events, and was set to 7.9 km s^{-1} in the NNE half of the profile- to 8.0 km s^{-1} in the SSW half of the profile.

5.3 Model assessment and uncertainty estimation

Models constructed by forward modeling from seismic travel-times does not represent a unique solution (Zelt, 1999). To evaluate the model uncertainty one have to consider the quality of the MCS and the OBS-data, the ray coverage, errors in phase picking, comparison

of travel times with observed arrivals (investigate hit-points) and consider the low control on velocity gradients (e.g. Zelt, 1999, Ansorge et al., 1982). There are also potential pitfalls when correlation near vertical incident reflection data with corresponding wide-angle data as the MCS is sensitive to vertical velocities and the OBS-data is sensitive to horizontal velocities. By introducing transverse isotropy in the rock/sediment, this will consequently provide an incorrect correlation of depth position between the two (Godfrey et al., 2002). This is normally a problem in layered mediums like shales. Even though there exists good data on the lithology of the sedimentary succession, calculations of misfit due to anisotropy is not within the scope of this thesis.

The sedimentary cover is in general pretty well constrained by strong and clear arrivals containing both wide-angle reflections and continues refraction events down to the Early Carboniferous. The phase picking for this section is therefore believed to be quite accurate. As the sedimentary phases also showed relatively simple geometry and coherent velocity-gradients across the profile, the modeling of the layers was straight forward, and a god fit between the synthetic travel-time curves and the picked phases should give a pick-uncertainty of 10 ms for the upper layer to around 30 ms for the lower part of the sedimentary cover.

For the Riphean complex, which corresponds to layer six in the sedimentary sequence, high amplitude reflections was observed in all OBSs, and the depth-position of this layer is therefore fairly well constrained. The interval-time for multiples in this section corresponds to around 40 ms and would account as an uncertainty in the picking. The biggest source of uncertainty for the Riphean complex is however the velocity-gradient from top to bottom. The ray coverage from this layer is almost no existing. This section is therefore a source of uncertainty in estimating the depth to the basement. A possible deviation of -0.3 - (-0.4) km s^{-1} is realistic, and would impart a 6-7 % uncertainty to the thickness estimate of the section (Breivik et al., 2002).

The Basement is also suffering from low ray-coverage and appears concealed by multiples from earlier arrivals. The pick uncertainty of reflection arrivals from the basement is in general considered very high, ranging from 80 – 120 ms. In a worst case scenario, multiples from earlier arrivals might even have been interpreted as basement-reflectors, and could possibly have a big impact on the modeled depth position of the basement in the order of several km's.

The middle crust is covered by clear and high amplitude arrivals, and was fairly easy to identify with certainty. The pick-uncertainty should therefore be around 80 ms, which is the time-interval between reciprocal pairs (multiples). The largest element of uncertainty for the

middle crust is the complex pattern of the reflectors in the area of 100-200 km in the profile which most likely represent independent reflections, or a local dip in the layering.

The Moho discontinuity is well-constrained by continues reflectors seen at great offsets-intervals, especially in OBSs 24-28. The uncertainty for the interface would be around ~100 ms which is the time-interval between multiples. The refraction events give a good match with observed data, and the geometry should be fairly realistic. The biggest uncertainty in regard of the depth-position of the Moho-discontinuity would be the following errors from layers above.

6. Discussion

6.1.1 Sedimentary cover

The sedimentary part of the model includes four major megasequences boundaries divided into a Cretaceous interval with velocity estimated to 2.5 – 3.8 km s^{-1}; a Middle and Early Triassic succession (Ladin, Induan and Inter Induan) with velocities estimated from 3.9 – 4.75 km s^{-1}; and the Early Carboniferous sequence with a velocity measured from 5.0 – 5.2 km s^{-1}. The Permian layer seen in the MCS from NPD was not included in the model as it could not be identified in the OBS-data. A possible explanation for this is the similarities in velocities between the Permian and Inter Induan layer (± 0.1 km s^{-1}). Another plausible explanation is that the Permian layer was interpreted from a seismic horizon in the MCS which possibly can be correlated to the sill observed in the OBS-data. The background to this claim is that a sill-intrusion was located at the same depth-position (Inter Induan – Early Carboniferous interface) and around the same area of the profile. Anyways, this will just be speculative as the raw-data of MCS-data was not available. In addition, no details on the actual position of the MCS-data relative to the OBS-transect were given. A large offset could possibly explain the variation between the constructed model from the OBS-data and the NPD-model.

The low velocity observed in the upper part of the Triassic don't gives any correlation with the expected values which both locally and regionally is confined within the 3.0 – 4.05 km s^{-1} interval (e.g. Breivik et al., 2002, Breivik et al., 2005, Breivik et al., 2003). As the velocity shows coherency across the whole profile, a mass-transfer of sediments in form of turbidity currents and sediment flow can be excluded. Neither are there any pronounced slopes in the area which could induce such a current. This leaves us with the possibility of an upper layer of Cenozoic age. This contradicts the general perception that Cenozoic sediments is missing in this area (e.g. Klitzke et al., 2014) due to the Late Cenozoic erosion (Vågnes et al., 1992).

6.1.2 Sub-platform sedimentary rocks

The lowermost sedimentary layer can either be correlated to Early Paleozoic age, which constitutes the main sedimentary cover beneath the eastern Barents Sea

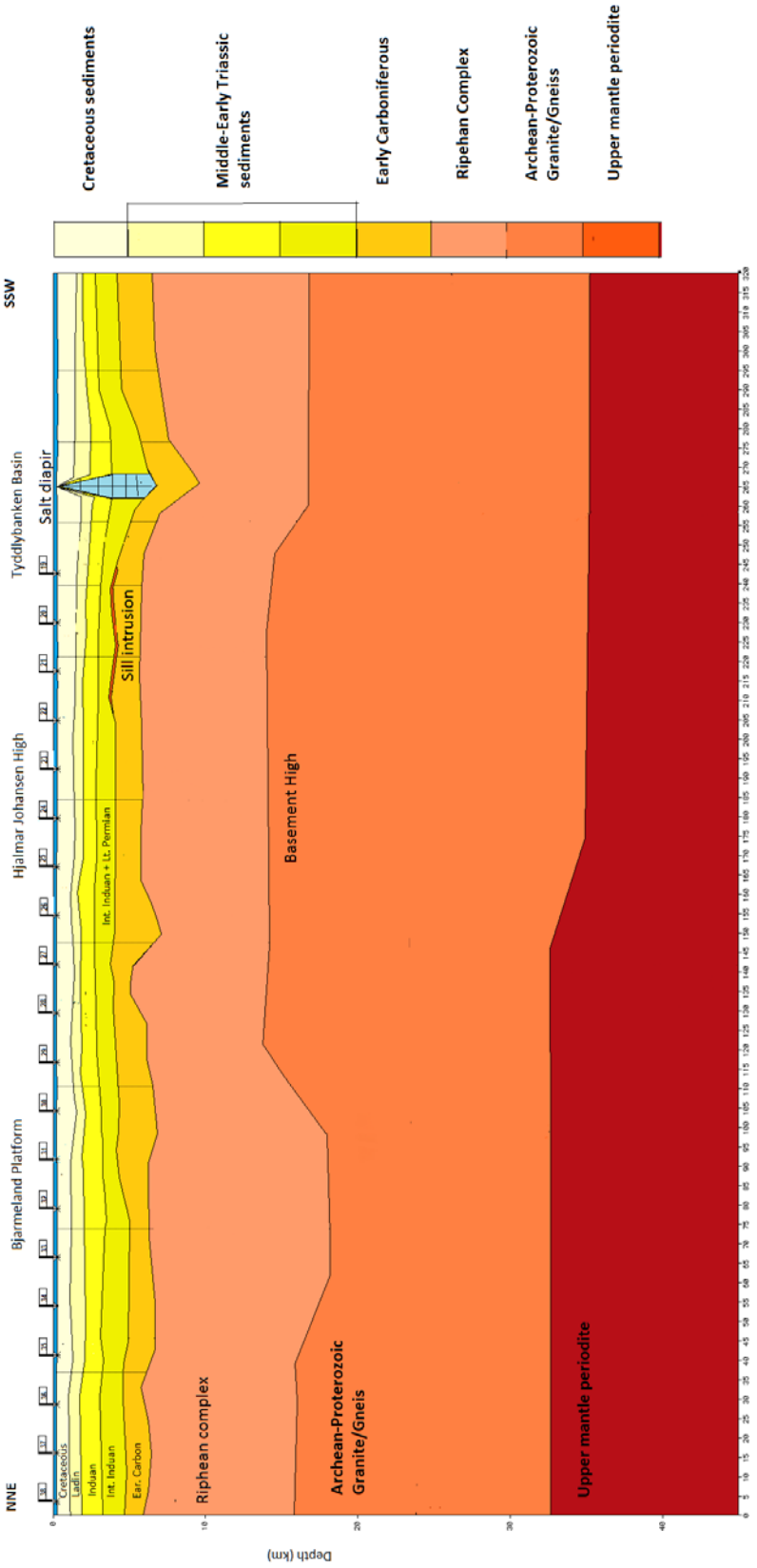

Fig. 6.1 - Geological model of the profile

constraints from aeromagnetic data above Bjarmeland Platform and the Nordkapp Basin (Gernigon et al., 2014). One of closest wide-angle and refraction profile to the study-area is the 1-AR profile from Ivanova et al. (2006) which supports the results from the aeromagnetic data. The SW-NE trending profile traces Riphean complex (corresponds to Middle-Late Proterozoic age) from outcroppings at the Baltic shield towards Hjalmar Johansen High (Fedynsky High/Uplift) (Fig. 6.2). The Uppermost Riphean deposits have been measured to hold a velocity off 5.7 – 5.9 km s^{-1} (Gramberg, 1988) which approximates the velocity given in the model. The lower Riphean are mapped beneath Bjarmeland Platform and consists of marbles, crystalline schist, gneiss and quartzite and is considered basement complex due to the folded and metamorphosed signature. The Riphean deposits might reach a thickness of 5-9 km, increasing to 12-13 km within graben structures (Ivanova, 2001). This is within the thickness-range seen in the final model.

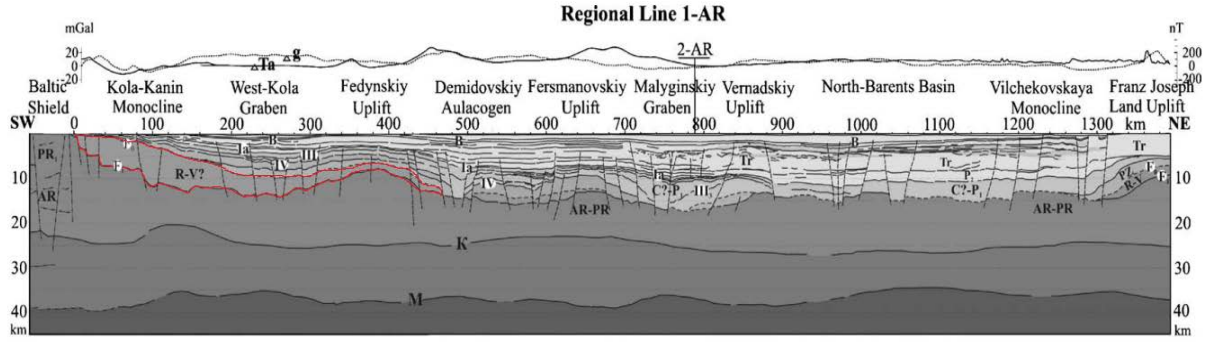

Fig. 6.2 – *Crustal profile transecting the Barent- Kara Region from south to north. The most important lithologies in this profile are the Riphean complex (R-V?); the crystalline upper crust (AR-PR) of granite-gneissic metamorphic Archean-Proterozoic complex recognized by a velocity-interval of 6.1 – 6.6 km s^{1-}; the K boundary with stable velocity of 6.8 – 7.0 km s^{-1} and the Moho-discontinuity (M).Figure from (Ivanova et al., 2006)*

6.1.3 The upper and middle crystalline crust

The velocity of the granite-gneissic metamorphic Archean-Proterozoic rocks in the 1-AR profile also fits the velocity of the upper and middle crust in the model, which is measured to 6.1 - 6.6 km s^{-1} from rocks sampled from a super deep well-tie on the Kola Peninsula and from refraction studies of the profile (Ivanova et al., 2006; and references therein). The thickness of the upper crust is highly variable in the 1-AR profile, ranging from 3-8 km in grabens to 15-20 km within Hjalmar Johansen Platform (Ivanova et al., 2006). This also fits the upper crust in the final model.

The velocity-gradient from the 1-AR profile suggest a gradually increase in velocity within the granite-gneissic metamorphic Archean-Proterozoic rocks. If this was to be applied to the final model, the strong reflection events observed from the middle crust needs an alternative explanation to the high amplitude, which was interpreted to be a result of a high velocity contrast between the upper and middle crust. A wide-angle reflection and refraction study northeast of the study area (Breivik et al., 2002) have observed almost the same velocities as the 1-AR profile in the whole crustal profile, with a velocity of 6.3 km s^{-1} in the upper crystalline basement to 6.6 km s^{-1} at the base of the lower crust. As the velocity-gradient seem to be more or less gradual from these studies, the strong reflectivity from the middle crust might possibly be reinterpreted. An alternative to the reflectivity is shear zones with mylonites or eclogites (Hurich et al., 1985, Fountain et al., 1994) or fluid-filled cracks within fault zones (Harjes et al., 1997), as inferred in (Breivik et al., 2002). Strong and high amplitude arrivals merge together with the Moho-reflections at close offsets on some of the OBSs and could possible support the presence of mylonites and eclogite in the very lower parts of the crust. The reason this arrivals was not constrained in the model was due to the lateral inconsistency.

6.1.4 The upper mantle

The velocity in the upper mantle is within the average velocity beneath continents, which has been calculated to be 8.09 ± 0.20 km s^{-1} (Christensen and Mooney, 1995), reflecting a peridotite bulk composition.

6.2 Crustal type

There is a systematic variation in crustal structures as a function of basement age and tectonic setting (e.g. Christensen and Mooney, 1995). Mooney et al. (1998) recognize 14 different types of crust (Fig. 6.3). The two most relevant for this study is the extended and the platform type. In comparison to figure 6.3, the model fits the extended crust in terms of crustal thickness and velocity-distribution; whereas a platform area might be give a better fit in terms of the absence of complex structures. If the Lower Riphean complex is represented in top parts of the sub-platform section, this would modify the position of the upper crystalline basement and consequently favor a platform area.

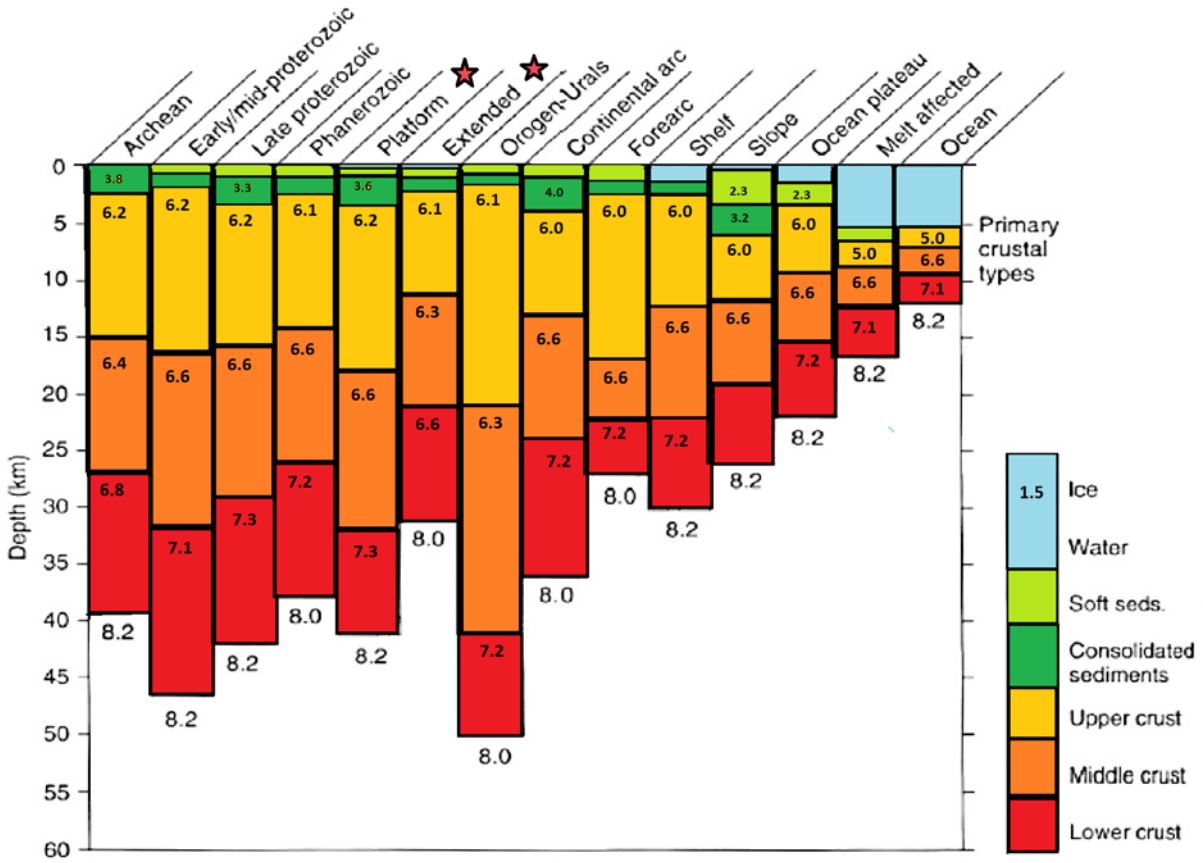

Fig. 6.3 *– Typical P-wave velocity and crustal structure (thickness) for continental and oceanic crustal types (Mooney, 1989). Velocities indicate the velocity in the upper part of each layer. The velocity–gradient is commonly from 0.01-0.02 km s^{-1}/km. Figure is modified from Romanowicz and Dziewonski (2010).*

7. Summary and conclusion

A P-wave velocity depth model was constructed from a total of 20 OBSs along a 320 km long profile transecting the Tiddlybanken Basin, Hjalmar Johansen High (Fedynsky High) and Bjarmeland Platform from SSW to NNE. The final velocity-model is divided into 9 layers, comprising six sedimentary layers, two crustal layers and upper parts of the upper mantle.

The sedimentary cover is extremely thick varying from 16-13 km, and has been divided into megasequences of Cretaceous, Early-Middle Triassic, and Carboniferous and Late Proterozoic age where the latter constitute the bulk of the sediments. The velocity from top to bottom is measured to 2.5–6.0 km s^{-1}. The ray-coverage for this section is really good constrained by clear arrivals, with the exception for the Late Proterozoic which only occurred in a few OBSs.

The crust consists of Archean-Proterozoic Granite and/or Gneiss with a velocity-interval of 6.15 – 6.35 km s^{-1} in the upper crust and 6.5 – 6.7 km s^{-1} in the middle crust. The total thickness of the crust varies from 13-20 km, typical for an extended crust type. The thickest section is beneath the basement high correlated to Hjalmar Johansen High. They ray coverage for the upper basement is really poor, and is a source of large uncertainty in terms of constraining depth-position and the velocity of the upper crust. The middle crust interface is consistently recognized by high-amplitude arrivals, but the lack of refractions gives an uncertainty in estimating the velocity within the layer and therefore also the depth-position of the Moho-discontinuity.

The Moho-discontinuity is located to 32-34 km depth, and has a pronounced slope beneath Hjalmar Johansen High. The velocity of the upper mantle is estimated to 7.9 – 8.0 km s^{-1}, typical for peridotite.

8. Bibliography

ANDERSEN, T. B. 1998. Extensional tectonics in the Caledonides of southern Norway, an overview. *Tectonophysics,* 285**,** 333-351.

ANDERSEN, T. B. & JAMTVEIT, B. 1990. Uplift of deep crust during orogenic extensional collapse: A model based on field studies in the Sogn-Sunnfjord Region of western Norway. *Tectonics,* 9**,** 1097-1111.

ANSORGE, J., PRODEHL, C. & BAMFORD, D. 1982. Comparative interpretation of explosion seismic data. SPRINGER VERLAG 175 FIFTH AVE, NEW YORK, NY 10010.

ARTYUSHKOV, E. 2005. The formation mechanism of the Barents basin. *Russian Geology and Geophysics (Geologiya i Geofizika),* 46**,** 683-696.

BERGSAGER, E. 1986. Future petroleum potential of the Barents Sea. *Habitat of Hydrocarbons on the Norwegian Continental Shelf***,** 339-354.

BRAILE, L. W. & SMITH, R. B. 1975. Guide to the interpretation of crustal refraction profiles. *Geophysical Journal International,* 40**,** 145-176.

BREIVIK, A. J., MJELDE, R., GROGAN, P., SHIMAMURA, H., MURAI, Y. & NISHIMURA, Y. 2005a. Caledonide development offshore–onshore Svalbard based on ocean bottom seismometer, conventional seismic, and potential field data. *Tectonophysics,* 401**,** 79-117.

BREIVIK, A. J., MJELDE, R., GROGAN, P., SHIMAMURA, H., MURAI, Y. & NISHIMURA, Y. 2005b. Caledonide development offshore–onshore Svalbard based on ocean bottom seismometer, conventional seismic, and potential field data. *Tectonophysics,* 401**,** 79-117.

BREIVIK, A. J., MJELDE, R., GROGAN, P., SHIMAMURA, H., MURAI, Y., NISHIMURA, Y. & KUWANO, A. 2002. A possible Caledonide arm through the Barents Sea imaged by OBS data. *Tectonophysics,* 355**,** 67-97.

CHRISTESON, G., MCINTOSH, K., SHIPLEY, T., FLUEH, E. R. & GOEDDE, H. 1999. Structure of the Costa Rica convergent margin, offshore Nicoya Peninsula. *Journal of Geophysical Research: Solid Earth (1978–2012),* 104**,** 25443-25468.

CHULICK, G. S. 1997. Comprehensive seismic survey database for developing three-dimensional models of the Earth's crust. *Seismological Research Letters,* 68**,** 734-742.

CLOETINGH, S. & KOOI, H. 1992. Intraplate stresses and dynamical aspects of rifted basins. *Tectonophysics,* 215**,** 167-185.

COCKS, L. & TORSVIK, T. 2006. European geography in a global context from the Vendian to the end of the Palaeozoic. *MEMOIRS-GEOLOGICAL SOCIETY OF LONDON,* 32**,** 83-95.

DENGO, C. & RØSSLAND, K. 1992. Extensional tectonic history of the western Barents Sea. *Structural and tectonic modelling and its applications to petroleum geology,* 1**,** 91-107.

DORÉ, A. 1991. The structural foundation and evolution of Mesozoic seaways between Europe and the Arctic. *Palaeogeography, Palaeoclimatology, Palaeoecology,* 87**,** 441-492.

DORÉ, A., LUNDIN, E., JENSEN, L., BIRKELAND, Ø., ELIASSEN, P. & FICHLER, C. Principal tectonic events in the evolution of the northwest European Atlantic margin. Geological Society, London, Petroleum Geology Conference series, 1999. Geological Society of London, 41-61.

DRACHEV, S., MALYSHEV, N. & NIKISHIN, A. Tectonic history and petroleum geology of the Russian Arctic Shelves: an overview. Geological society, London, petroleum geology conference series, 2010. Geological Society of London, 591-619.

EBBING, J., BRAITENBERG, C. & WIENECKE, S. 2007. Insights into the lithospheric structure and tectonic setting of the Barents Sea region from isostatic considerations. *Geophysical Journal International,* 171**,** 1390-1403.

EIKEN, O. & AUSTEGARD, A. 1987. The Tertiary orogenic belt of West-Spitsbergen: Seismic expressions of the offshore sedimentary basins. *Norsk Geologisk Tidsskrift,* 67**,** 383-394.

ELDHOLM, O., THIEDE, J. & TAYLOR, E. Evolution of the Norwegian continental margin: background and objectives. Eldholm, O., Thiede, J., Taylor, E., et al., Proc. ODP, Init. Repts, 1987. 5-25.

ELDHOLM, O., THIEDE, J. & TAYLOR, E. The Norwegian continental margin: Tectonic, volcanic, and paleoenvironmental framework. Proceedings of the ocean drilling program, scientific results, 1989. 5-26.

ENGEN, Ø., FALEIDE, J. I. & DYRENG, T. K. 2008. Opening of the Fram Strait gateway: a review of plate tectonic constraints. *Tectonophysics,* 450**,** 51-69.

FALEIDE, J., GUDLAUGSSON, S., ELDHOLM, O., MYHRE, A. & JACKSON, H. 1991a. Deep seismic transects across the sheared western Barents Sea-Svalbard continental margin. *Tectonophysics,* 189**,** 73-89.

FALEIDE, J., VÅGNES, E. & GUDLAUGSSON, S. Late Mesozoic–Cenozoic evolution of the southwestern Barents Sea. Geological Society, London, Petroleum Geology Conference series, 1993a. Geological Society of London, 933-950.

FALEIDE, J. I., GUDLAUGSSON, S. T., ELDHOLM, O., MYHRE, A. M. & JACKSON, H. R. 1991b. Deep seismic transects across the sheared western Barents Sea-Svalbard continental margin. *Tectonophysics,* 189**,** 73-89.

FALEIDE, J. I., GUDLAUGSSON, S. T. & JACQUART, G. 1984. Evolution of the western Barents Sea. *Marine and Petroleum Geology,* 1**,** 123-150.

FALEIDE, J. I., SOLHEIM, A., FIEDLER, A., HJELSTUEN, B. O., ANDERSEN, E. S. & VANNESTE, K. 1996a. Late Cenozoic evolution of the western Barents Sea-Svalbard continental margin. *Global and Planetary Change,* 12**,** 53-74.

FALEIDE, J. I., SOLHEIM, A., FIEDLER, A., HJELSTUEN, B. O., ANDERSEN, E. S. & VANNESTE, K. 1996b. Late Cenozoic evolution of the western Barents Sea-Svalbard continental margin. *Global and Planetary Change,* 12**,** 53-74.

FALEIDE, J. I., TSIKALAS, F., BREIVIK, A. J., MJELDE, R., RITZMANN, O., ENGEN, O., WILSON, J. & ELDHOLM, O. 2008. Structure and evolution of the continental margin off Norway and the Barents Sea. *Episodes,* 31**,** 82.

FALEIDE, J. I., VÅGNES, E. & GUDLAUGSSON, S. T. 1993b. Late Mesozoic-Cenozoic evolution of the south-western Barents Sea in a regional rift-shear tectonic setting. *Marine and Petroleum Geology,* 10**,** 186-214.

FICHLER, C., RUNDHOVDE, E., JOHANSEN, S. & SAETHER, B. 1997. Barents Sea tectonic structures visualized by ERS1 satellite gravity data with indications of an offshore Baikalian trend. *first break,* 15**,** 582-585.

FOSSEN, H. 1992. The role of extensional tectonics in the Caledonides of south Norway. *Journal of structural geology,* 14**,** 1033-1046.

FOSSEN, H. 2000. Extensional tectonics in the Caledonides: Synorogenic or postorogenic? *Tectonics,* 19**,** 213-224.

FOSSUM, B. J., SCHMIDT, W. J., JENKINS, D. A., BOGATSKY, V. I. & RAPPOPORT, B. I. 2001. AAPG Memoir 74, Chapter 13: New frontiers for hydrocarbon production in the Timan-Pechora Basin, Russia.

GABRIELSEN, R., KLØVJAN, O., RASMUSSEN, A. & STØLAN, T. 1992. Interaction between halokinesis and faulting: structuring of the margins of the Nordkapp Basin, Barents Sea region. *Structural and tectonic modelling and its application to petroleum geology. Norwegian Pet Soc Spec Publ,* 1**,** 121-131.

GABRIELSEN, R., ODINSEN, T. & GRUNNALEITE, I. 1999. Structuring of the Northern Viking Graben and the Møre Basin; the influence of basement structural grain, and the particular role of the Møre-Trøndelag Fault Complex. *Marine and Petroleum Geology,* 16**,** 443-465.

GABRIELSEN, R. H., FAERSETH, R. B. & JENSEN, L. N. 1990. *Structural Elements of the Norwegian Continental Shelf. Pt. 1. The Barents Sea Region,* Norwegian Petroleum Directorate.

GAC, S., HUISMANS, R. S., PODLADCHIKOV, Y. Y. & FALEIDE, J. I. 2012. On the origin of the ultradeep East Barents Sea basin. *Journal of Geophysical Research: Solid Earth (1978–2012),* 117.

GEE, D. 2004. The barentsian caledonides: death of the high arctic barents craton. *Arctic Geology, Hydrocarbon Resources and Environmental Challenges,* 2**,** 48-49.

GEE, D., BOGOLEPOVA, O. & LORENZ, H. 2006. The Timanide, Caledonide and Uralide orogens in the Eurasian high Arctic, and relationships to the palaeo-continents Laurentia, Baltica and Siberia. *Geological Society, London, Memoirs,* 32**,** 507-520.

GEE, D. G., FOSSEN, H., HENRIKSEN, N. & HIGGINS, A. K. 2008. From the early Paleozoic platforms of Baltica and Laurentia to the Caledonide Orogen of Scandinavia and Greenland. *Episodes,* 31**,** 44.

GEE, D. G. & PEASE, V. 2004. The Neoproterozoic Timanide Orogen of eastern Baltica: introduction. *Geological Society, London, Memoirs,* 30**,** 1-3.

GODFREY, N., CHRISTENSEN, N. & OKAYA, D. 2002. The effect of crustal anisotropy on reflector depth and velocity determination from wide-angle seismic data: a synthetic example based on South Island, New Zealand. *Tectonophysics,* 355**,** 145-161.

GRAMBERG, I. 1988. Barentsevskaya Sshel'fovaya Pilita. Moscow: Nedra.

GRAMBERG, I. S., GLEBOVSKY, V., GRIKUROV, G. E., IVANOV, V. L., KORAGO, E. A., PISKAREV, A., POGREBITSKY, Y., SHIPELKEVITCH, Y. & SUPRUNENKO, O. 2001. Eurasian Arctic margin: earth science problems and research challenges. *Polarforschung,* 69**,** 3-25.

GROGAN, P., NYBERG, K., FOTLAND, B., MYKLEBUST, R., DAHLGREN, S. & RIIS, F. 2000. Cretaceous magmatism south and east of Svalbard: evidence from seismic reflection and magnetic data. *Polarforschung,* 68**,** 25-34.

GUDLAUGSSON, S., FALEIDE, J., FANAVOLL, S. & JOHANSEN, B. 1987. Deep seismic reflection profiles across the western Barents Sea. *Geophysical Journal International,* 89**,** 273-278.

GUDLAUGSSON, S., FALEIDE, J., JOHANSEN, S. & BREIVIK, A. 1998. Late Palaeozoic structural development of the south-western Barents Sea. *Marine and Petroleum Geology,* 15**,** 73-102.

HAGEVANG, T., ELDHOLM, O. & AALSTAD, I. 1983. Pre-23 magnetic anomalies between Jan Mayen and Greenland-Senja fracture zones in the Norwegian Sea. *Marine Geophysical Researches,* 5**,** 345-363.

HARTZ, E. H. & ANDRESEN, A. 1997. From collision to collapse: Complex strain permutations in the hinterland of the Scandinavian Caledonides. *Journal of Geophysical Research: Solid Earth (1978–2012),* 102**,** 24697-24711.

HENRIKSEN, E., RYSETH, A., LARSSEN, G., HEIDE, T., RØNNING, K., SOLLID, K. & STOUPAKOVA, A. 2011. Tectonostratigraphy of the greater Barents Sea:

implications for petroleum systems. *Geological Society, London, Memoirs,* 35**,** 163-195.
HOSSACK, J. & COOPER, M. 1986. Collision tectonics in the Scandinavian Caledonides. *Geological Society, London, Special Publications,* 19**,** 285-304.
IVANOVA, N., SAKOULINA, T. & ROSLOV, Y. V. 2006. Deep seismic investigation across the Barents–Kara region and Novozemelskiy Fold Belt (Arctic Shelf). *Tectonophysics,* 420**,** 123-140.
JACKSON, H., FALEIDE, J. & ELDHOLM, O. 1990. Crustal structure of the sheared southwestern Barents Sea continental margin. *Marine Geology,* 93**,** 119-146.
JAKOBSSON, M., MAYER, L., COAKLEY, B., DOWDESWELL, J. A., FORBES, S., FRIDMAN, B., HODNESDAL, H., NOORMETS, R., PEDERSEN, R. & REBESCO, M. 2012. The international bathymetric chart of the Arctic Ocean (IBCAO) version 3.0. *Geophysical Research Letters,* 39.
JOHANSEN, S., OSTISTY, B., BIRKELAND, Ø., FEDOROVSKY, Y., MARTIROSJAN, V., BRUUN CHRISTENSEN, O., CHEREDEEV, S., IGNATENKO, E. & MARGULIS, L. 1992. Hydrocarbon potential in the Barents Sea region: play distribution and potential. *Arctic geology and petroleum potential,* 2**,** 273-320.
KANDILAROV, A., MJELDE, R., OKINO, K. & MURAI, Y. 2008. Crustal structure of the ultra-slow spreading Knipovich Ridge, North Atlantic, along a presumed amagmatic portion of oceanic crustal formation. *Marine Geophysical Researches,* 29**,** 109-134.
KEAREY, P., BROOKS, M. & HILL, I. 2009. *An introduction to geophysical exploration,* John Wiley & Sons.
KOYI, H. A., MILNES, A. G., SCHMELING, H., TALBOT, C. J., JUHLIN, C. & ZEYEN, H. 1999. Numerical models of ductile rebound of crustal roots beneath mountain belts. *Geophysical Journal International,* 139**,** 556-562.
KRISTOFFERSEN, Y. & TALWANI, M. 1977. Extinct triple junction south of Greenland and the Tertiary motion of Greenland relative to North America. *Geological Society of America Bulletin,* 88**,** 1037-1049.
KROGH, E. J. 1977. Evidence of Precambrian continent-continent collision in Western Norway. *Nature,* 267**,** 17-19.
LARSSEN, G., ELVEBAKK, G., HENRIKSEN, L. B., KRISTENSEN, S., NILSSON, I., SAMUELSBERG, T., SVÅNÅ, T., STEMMERIK, L. & WORSLEY, D. 2002. Upper Palaeozoic lithostratigraphy of the Southern Norwegian Barents Sea. *Norwegian Petroleum Directorate Bulletin,* 9**,** 76.
LEVSHIN, A. L., SCHWEITZER, J., WEIDLE, C., SHAPIRO, N. M. & RITZWOLLER, M. H. 2007. Surface wave tomography of the Barents Sea and surrounding regions. *Geophysical Journal International,* 170**,** 441-459.
LOBKOVSKY, L., CLOETINGH, S., NIKISHIN, A., VOLOZH, Y. A., LANKREIJER, A., BELYAKOV, S., GROSHEV, V., FOKIN, P., MILANOVSKY, E. & PEVZNER, L. 1996. Extensional basins of the former Soviet Union—structure, basin formation mechanisms and subsidence history. *Tectonophysics,* 266**,** 251-285.
LUETGERT, J. 1992. MacRay: Interactive two-dimensional seismic raytracing for the Macintosh. *US Geol. Surv. Open File Rep,* 92**,** 43.
LUETGERT, J. H. 1988. *User's Manual for RAY84/R83PLT Interactive Two-dimensional Raytracing/synthetic Seismogram Package,* US Department of the Interior, Geological Survey.
LUNDIN, E. & DORÉ, A. G. 2002. Mid-Cenozoic post-breakup deformation in the 'passive' margins bordering the Norwegian–Greenland Sea. *Marine and Petroleum Geology,* 19**,** 79-93.
MAROTTA, A., FERNANDEZ, M. & SABADINI, R. 1998. Mantle unrooting in collisional settings. *Tectonophysics,* 296**,** 31-46.

MCCLAY, M., CONEY, P. & DAVIS, G. 1986. Collapse of the Caledonian orogen and the Old Red Sandstone.

MILNES, A. & KOYI, H. 2000. Ductile rebound of an orogenic root: case study and numerical model of gravity tectonics in the Western Gneiss Complex, Caledonides, southern Norway. *Terra Nova,* 12**,** 1-7.

MILNES, A., WENNBERG, O., SKÅR, Ø. & KOESTLER, A. 1997. Contraction, extension and timing in the South Norwegian Caledonides: the Sognefjord transect. *Geological Society, London, Special Publications,* 121**,** 123-148.

MJELDE, R., DIGRANES, P., SHIMAMURA, H., SHIOBARA, H., KODAIRA, S., BREKKE, H., EGEBJERG, T., SØRENES, N. & THORBJØRNSEN, S. 1998. Crustal structure of the northern part of the Vøring Basin, mid-Norway margin, from wide-angle seismic and gravity data. *Tectonophysics,* 293**,** 175-205.

MOONEY, W. D. 1989. Seismic methods for determining earthquake source parameters and lithospheric structure. *Geological Society of America Memoirs,* 172**,** 11-34.

MURILLO, A. E. & BELL, J. 1999. Distributed Seismic Unix: a tool for seismic data processing. *Concurrency: Practice and Experience,* 11**,** 169-187.

MYHRE, A. M., ELDHOLM, O. & SUNDVOR, E. 1982. The margin between Senja and Spitsbergen fracture zones: implications from plate tectonics. *Tectonophysics,* 89**,** 33-50.

NAIMARK, B. M. & ISMAIL-ZADEH, A. T. 1995. Numerical models of a subsidence mechanism in intracratonic basins: application to North American basins. *Geophysical Journal International,* 123**,** 149-160.

NAKAMURA, Y., DONOHO, P. L., ROPER, P. H. & MCPHERSON, P. M. 1987. Large-offset seismic surveying using ocean-bottom seismographs and air guns: Instrumentation and field technique. *Geophysics,* 52**,** 1601-1611.

NIKISHIN, A., ZIEGLER, P., STEPHENSON, R., CLOETINGH, S., FURNE, A., FOKIN, P., ERSHOV, A., BOLOTOV, S., KOROTAEV, M. & ALEKSEEV, A. 1996. Late Precambrian to Triassic history of the East European Craton: dynamics of sedimentary basin evolution. *Tectonophysics,* 268**,** 23-63.

NILSEN, K. T., VENDEVILLE, B. C. & JOHANSEN, J.-T. 1995. Influence of regional tectonics on halokinesis in the Nordkapp Basin, Barents Sea.

NUNNS, A. & PEACOCK, J. 1983. Correlation, identification and inversion of magnetic anomalies in the Norway Basin. *Earth Evol. Sci,* 2**,** 130-138.

NUNNS, A. G. 1983. Plate tectonic evolution of the Greenland-Scotland Ridge and surrounding regions. *Structure and development of the Greenland-Scotland Ridge.* Springer.

NØTTVEDT, A., BERGLUND, L., RASMUSSEN, E. & STEEL, R. 1988. Some aspects of Tertiary tectonics and sedimentation along the western Barents Shelf. *Geological Society, London, Special Publications,* 39**,** 421-425.

O'LEARY, N., WHITE, N., TULL, S., BASHILOV, V., KUPRIN, V., NATAPOV, L. & MACDONALD, D. 2004. Evolution of the Timan–Pechora and south barents sea basins. *Geological Magazine,* 141**,** 141-160.

OLESEN, O., GELLEIN, J., HÅBREKKE, H., KIHLE, O., SKILBREI, J. & SMETHURST, M. 1997. Magnetic anomaly map Norway and adjacent ocean areas, scale 1: 3 million. *Geological Survey of Norway, Trondheim*.

OTTO, S. & BAILEY, R. 1995. Tectonic evolution of the northern Ural Orogen. *Journal of the Geological Society,* 152**,** 903-906.

PETROV, O. V., SOBOLEV, N. N., KOREN, T. N., VASILIEV, V. E., PETROV, E. O., LARSSEN, G. B. & SMELROR, M. 2008. Palaeozoic and Early Mesozoic evolution of the East Barents and Kara Seas sedimentary basins. *Norw J Geol,* 88**,** 227-234.

PUCHKOV, V. 2002. Paleozoic evolution of the East European continental margin involved in the Uralide orogeny. *Mountain Building in the Uralides: Pangea to the Present*, 9-31.

RITZMANN, O. & FALEIDE, J. I. 2009. The crust and mantle lithosphere in the Barents Sea/Kara Sea region. *Tectonophysics,* 470**,** 89-104.

ROBERTS, D. & GEE, D. 1985. An introduction to the structure of the Scandinavian Caledonides. *The Caledonide orogen–Scandinavia and related areas,* 1**,** 55-68.

ROBERTS, D. & OLOVYANISHNIKOV, V. 2004. Structural and tectonic development of the Timanide orogen. *Geological Society, London, Memoirs,* 30**,** 47-57.

RONNEVIK, H., BESKOW, B. & JACOBSEN, H. P. 1982. Structural and stratigraphic evolution of the Barents Sea.

RYSETH, A., AUGUSTSON, J. H., CHARNOCK, M., HAUGERUD, O., KNUTSEN, S.-M., MIDBØE, P. S., OPSAL, J. G. & SUNDSBØ, G. 2003. Cenozoic stratigraphy and evolution of the Sørvestsnaget Basin, southwestern Barents Sea. *Norwegian Journal of Geology/Norsk Geologisk Forening,* 83.

RØNNEVIK, H. & JACOBSEN, H.-P. 1984. *Structural highs and basins in the western Barents Sea,* Springer.

SAALMANN, K. & THIEDIG, F. 2001. Tertiary West Spitsbergen fold and thrust belt on Brøggerhalvøya, Svalbard: Structural evolution and kinematics. *Tectonics,* 20**,** 976-998.

SAUNDERS, A., FITTON, J., KERR, A., NORRY, M. & KENT, R. 1997. The north Atlantic igneous province. *Large igneous provinces: Continental, oceanic, and planetary flood volcanism***,** 45-93.

SCHOTT, B. & SCHMELING, H. 1998. Delamination and detachment of a lithospheric root. *Tectonophysics,* 296**,** 225-247.

SEMPRICH, J., SIMON, N. S. & PODLADCHIKOV, Y. Y. 2010. Density variations in the thickened crust as a function of pressure, temperature, and composition. *International Journal of Earth Sciences,* 99**,** 1487-1510.

SHERIFF, R. E. & GELDART, L. P. 1995. *Exploration seismology,* Cambridge university press.

SKOGSEID, J., PEDERSEN, T., ELDHOLM, O. & LARSEN, B. T. 1992. Tectonism and magmatism during NE Atlantic continental break-up: the Vøring Margin. *Geological Society, London, Special Publications,* 68**,** 305-320.

SMELROR, M., PETROV, O., LARSSEN, G. B. & WERNER, S. 2009. Geological history of the Barents Sea. *Norges Geol. undersøkelse***,** 1-135.

SRIVASTAVA, S. 1978. Evolution of the Labrador Sea and its bearing on the early evolution of the North Atlantic. *Geophysical Journal International,* 52**,** 313-357.

STEL, H., CLOETINGH, S., HEEREMANS, M. & VAN DER BEEK, P. 1993. Anorogenic granites, magmatic underplating and the origin of intracratonic basins in a non-extensional setting. *Tectonophysics,* 226**,** 285-299.

STEMMERIK, L. & WORSLEY, D. 2005. 30 years on: Arctic Upper Palaeozoic stratigraphy, depositional evolution and hydrocarbon prospectivity. *Norsk Geologisk Tidsskrift,* 85.

SUND, T., SKARPNES, O., JENSEN, L. N. & LARSEN, R. 1986. Tectonic development and hydrocarbon potential offshore Troms, northern Norway.

TALWANI, M. & ELDHOLM, O. 1972. Continental margin off Norway: a geophysical study. *Geological Society of America Bulletin,* 83**,** 3575-3606.

TALWANI, M. & ELDHOLM, O. 1977. Evolution of the Norwegian-Greenland sea. *Geological Society of America Bulletin,* 88**,** 969-999.

TERRY, M. P., ROBINSON, P., HAMILTON, M. A. & JERCINOVIC, M. J. 2000. Monazite geochronology of UHP and HP metamorphism, deformation, and exhumation, Nordøyane, Western Gneiss Region, Norway. *American Mineralogist,* 85**,** 1651-1664.
TORSVIK, T. H. & ANDERSEN, T. B. 2002. The Taimyr fold belt, Arctic Siberia: timing of prefold remagnetisation and regional tectonics. *Tectonophysics,* 352**,** 335-348.
VERBA, M., DARAGAN-SUSHCHOVA, L. & PAVLENKIN, A. 1992. Riftogenic structures of the western Arctic Shelf investigated by refraction surveys. *International Geology Review,* 34**,** 753-764.
VERBA, V. 1985. Comparative geological-geophysical characteristics of the Barents Sea and North Sea salt basins.
VORREN, T. O., HALD, M. & LEBESBYE, E. 1988. Late cenozoic environments in the Barents Sea. *Paleoceanography,* 3**,** 601-612.
VORREN, T. O., KRISTOFFERSEN, Y. & ANDREASSEN, K. 1986. Geology of the inner shelf west of North Cape, Norway. *Nor. Geol. Tidsskr,* 66.
VORREN, T. O., RICHARDSEN, G., KNUTSEN, S.-M. & HENRIKSEN, E. 1991. Cenozoic erosion and sedimentation in the western Barents Sea. *Marine and Petroleum Geology,* 8**,** 317-340.
VÅGNES, E., FALEIDE, J. & GUDLAUGSSON, S. 1992. Glacial erosion and tectonic uplift in the Barents Sea. *Norsk geologisk tidsskrift,* 72**,** 333-338.
WILKS, W. & CUTHBERT, S. 1994. The evolution of the Hornelen Basin detachment system, western Norway: implications for the style of late orogenic extension in the southern Scandinavian Caledonides. *Tectonophysics,* 238**,** 1-30.
WILSON, J. T. 1966. *Did the Atlantic close and then re-open?,* Nature.
WORSLEY, D. 2008. The post-Caledonian development of Svalbard and the western Barents Sea. *Polar Research,* 27**,** 298-317.
WORSLEY, D., NAKREM, H. & MØRK, A. The post-Caledonian geological development of Svalbard and the Barents Sea. Norsk Geologisk Forening 3. Abstracts and Proceedings of the Geological Society of Norway, 2006. Geological Society of Norway Trondheim, 5-21.
ZELT, C. 1993. Documentation for RAYINVR and related programs. *unpublished software manual*.
ZELT, C. & ELLIS, R. 1988. Practical and efficient ray tracing in two-dimensional media for rapid traveltime and amplitude forward modeling. *Can. J. Explor. Geophys,* 24**,** 16-31.
ZELT, C. & SMITH, R. 1992. Seismic traveltime inversion for 2-D crustal velocity structure. *Geophysical journal international,* 108**,** 16-34.
ZELT, C. A. 1999. Modelling strategies and model assessment for wide-angle seismic traveltime data. *Geophysical Journal International,* 139**,** 183-204.
ZIEGLER, P. A. 1988. EVOLUTION OF THE ARCTIC-NORTH ATLANTIC AND THE WESTERN TETHYS--A VISUAL PRESENTATION OF A SERIES OF PALEOGEOGRAPHIC-PALEOTECTONIC MAPS*. *Mem.-Am. Assoc. Pet. Geol,* 43**,** 164-196.

Internet sources

[16. Nov 2014] - http://www.npd.no/en/Publications/Resource-Reports/2013/Chapter-

APPENDIX

Raytracing plots and seismograms

The following pages contain plots of the (1) synthetic P-rays traced trough the constructed P-wave veocity model; (2) the interpreted seismogram (picks) overlaying computed traveltime curves; and (3) the seismograms from the hydrophone channel from OBSs 19-38. All plots are displayed with traveltime reduction of 8 km s^{-1}, and the seismograms are shown with bandpass filter on in order to enchance large offset events such as the Moho reflections (PmP) and the upper mantle refractions (Pn). Note that the of the geometry of the travel-time curves in the ray-tracing highly depends on the ray-coverage (density of shot points). As MacRay has a upper limit of 300 shot points shoot simultaneously, the program tends to interpolate traveltime curves between close and far offset arrivals instead of distribute the shoot points evenly. This results in a unconstrained area in the middle of the plot.

OBS 19

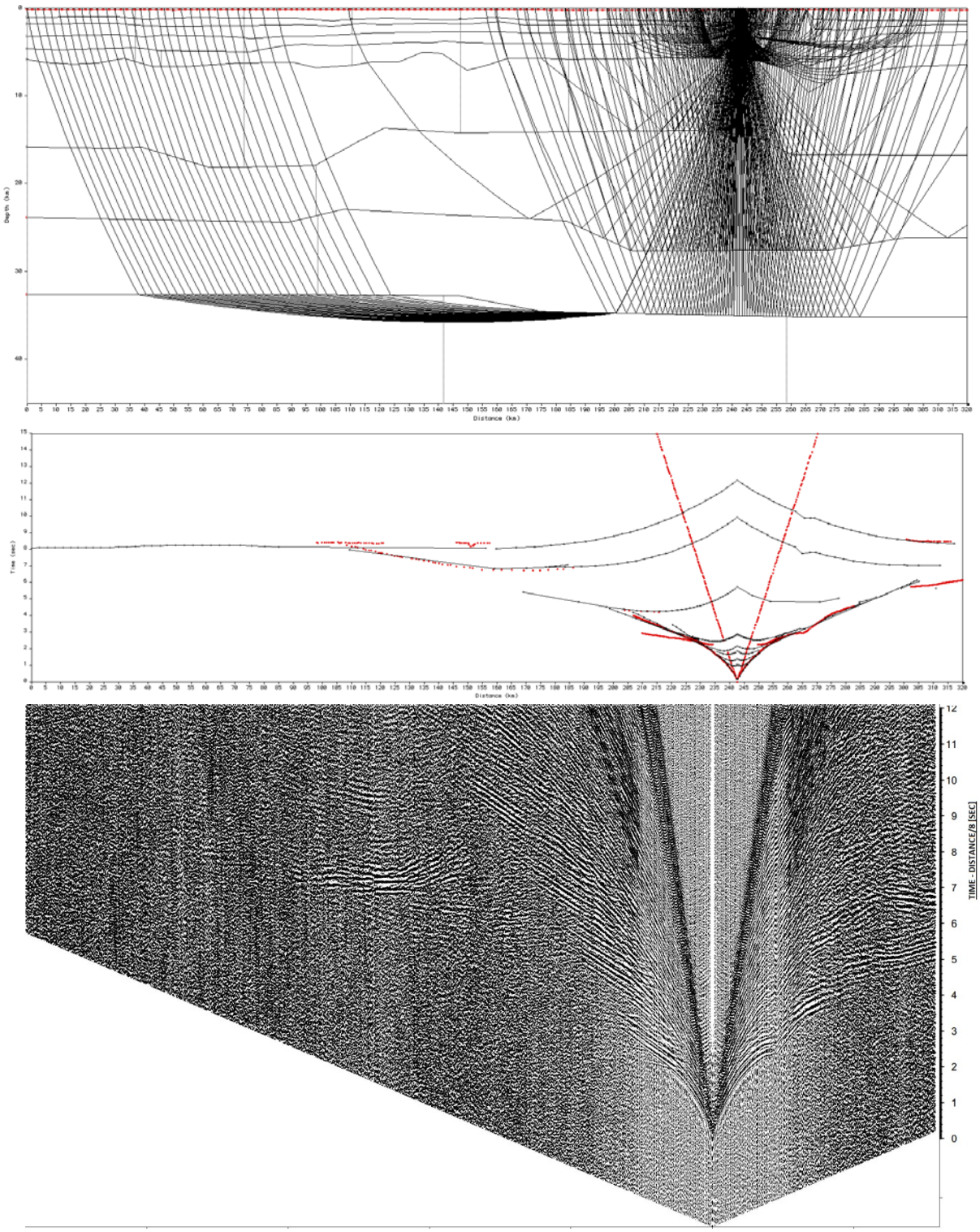

Fig. A – Upper plot shows computed rays traced through the model; middle plot contain calculated traveltime-curves (black) overlain by interpreted picks (red dots); and the lowermost plot is the associated seismogram.

OBS 20

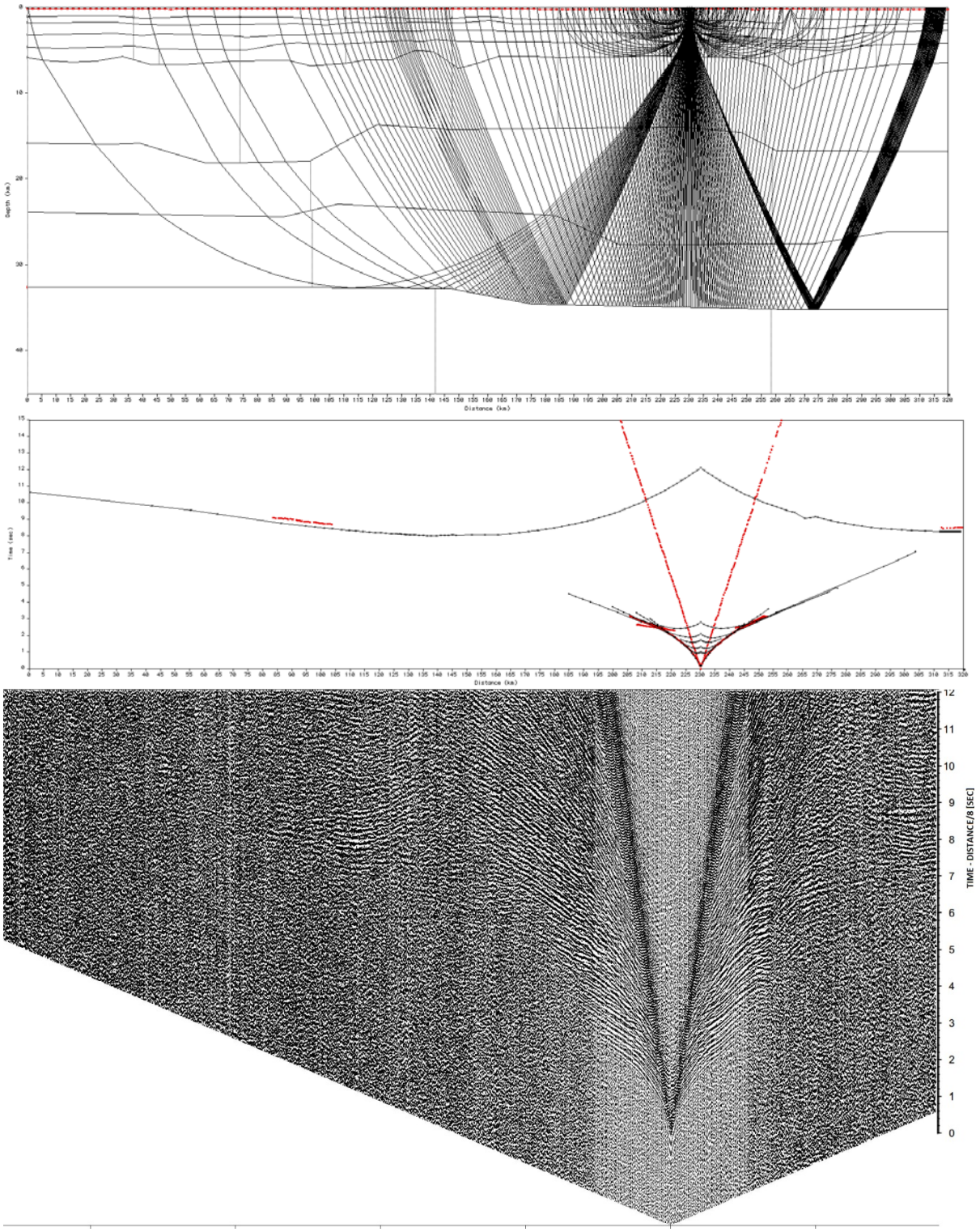

Fig. B - Upper plot shows computed rays traced through the model; middle plot contain calculated traveltime-curves (black) overlain by interpreted picks (red dots); and the lowermost plot is the associated seismogram.

OBS 21

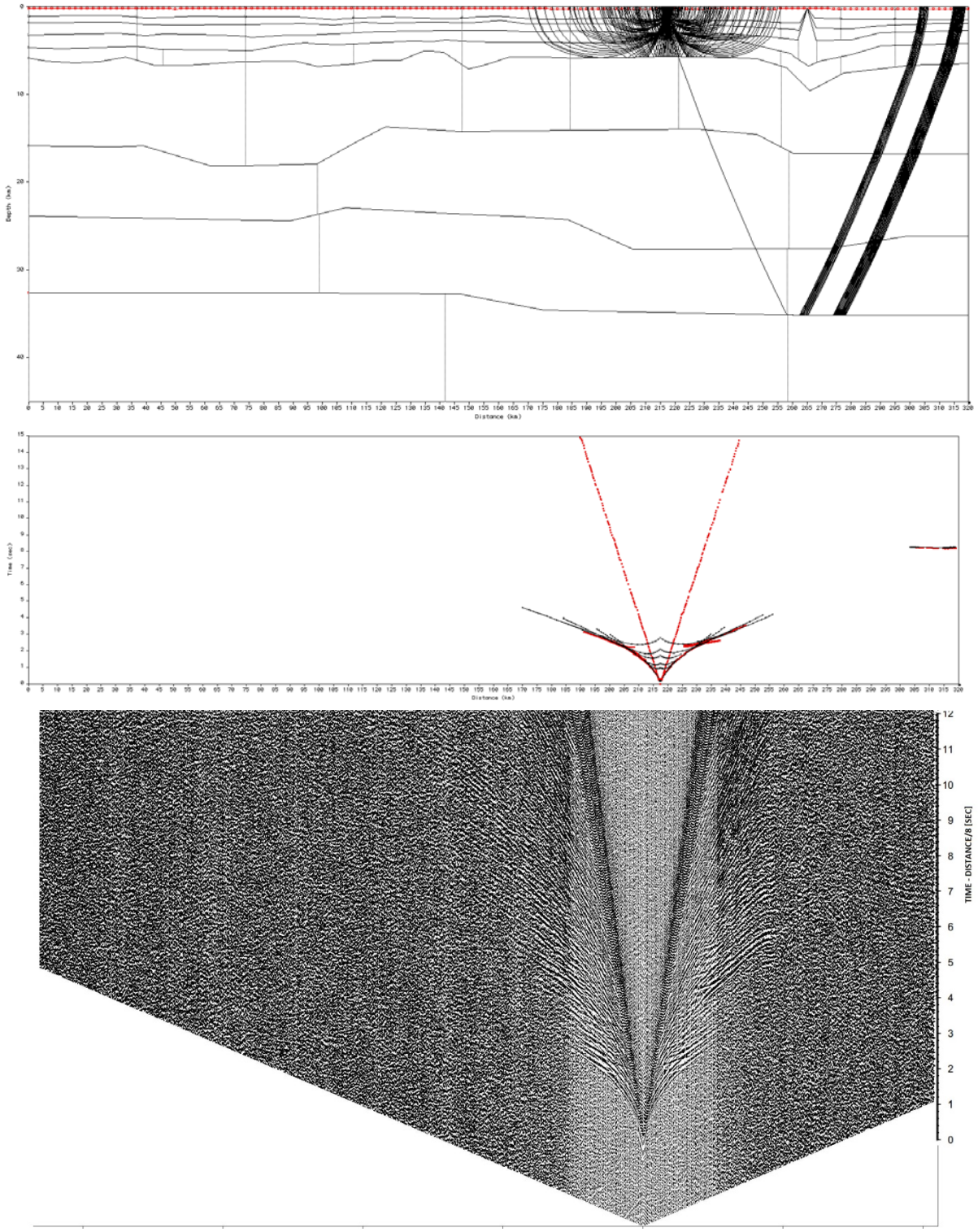

Fig. C - Upper plot shows computed rays traced through the model; middle plot contain calculated traveltime-curves (black) overlain by interpreted picks (red dots); and the lowermost plot is the associated seismogram.
OBS 22

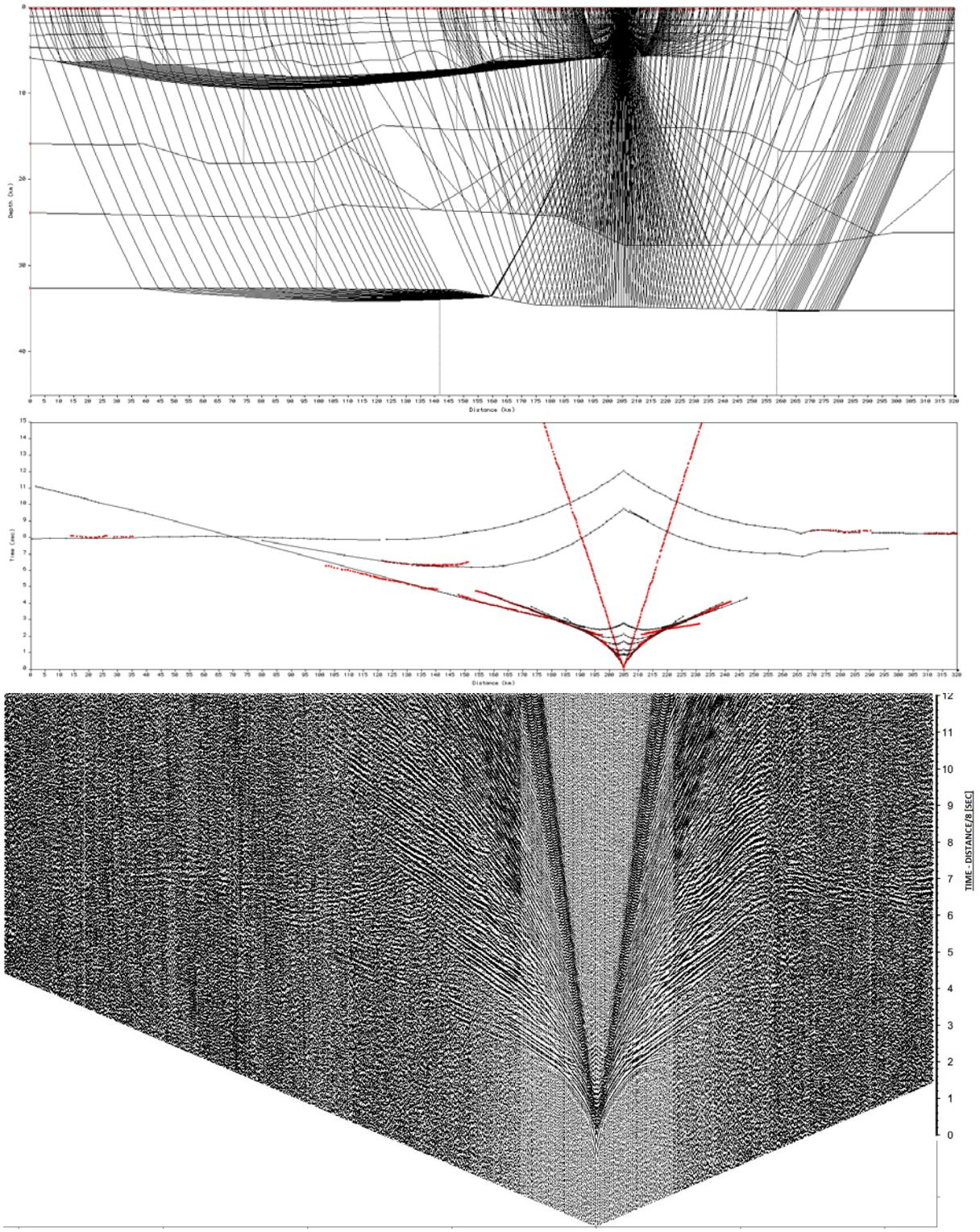

Fig. D - Upper plot shows computed rays traced through the model; middle plot contain calculated traveltime-curves (black) overlain by interpreted picks (red dots); and the lowermost plot is the associated seismogram

OBS 23

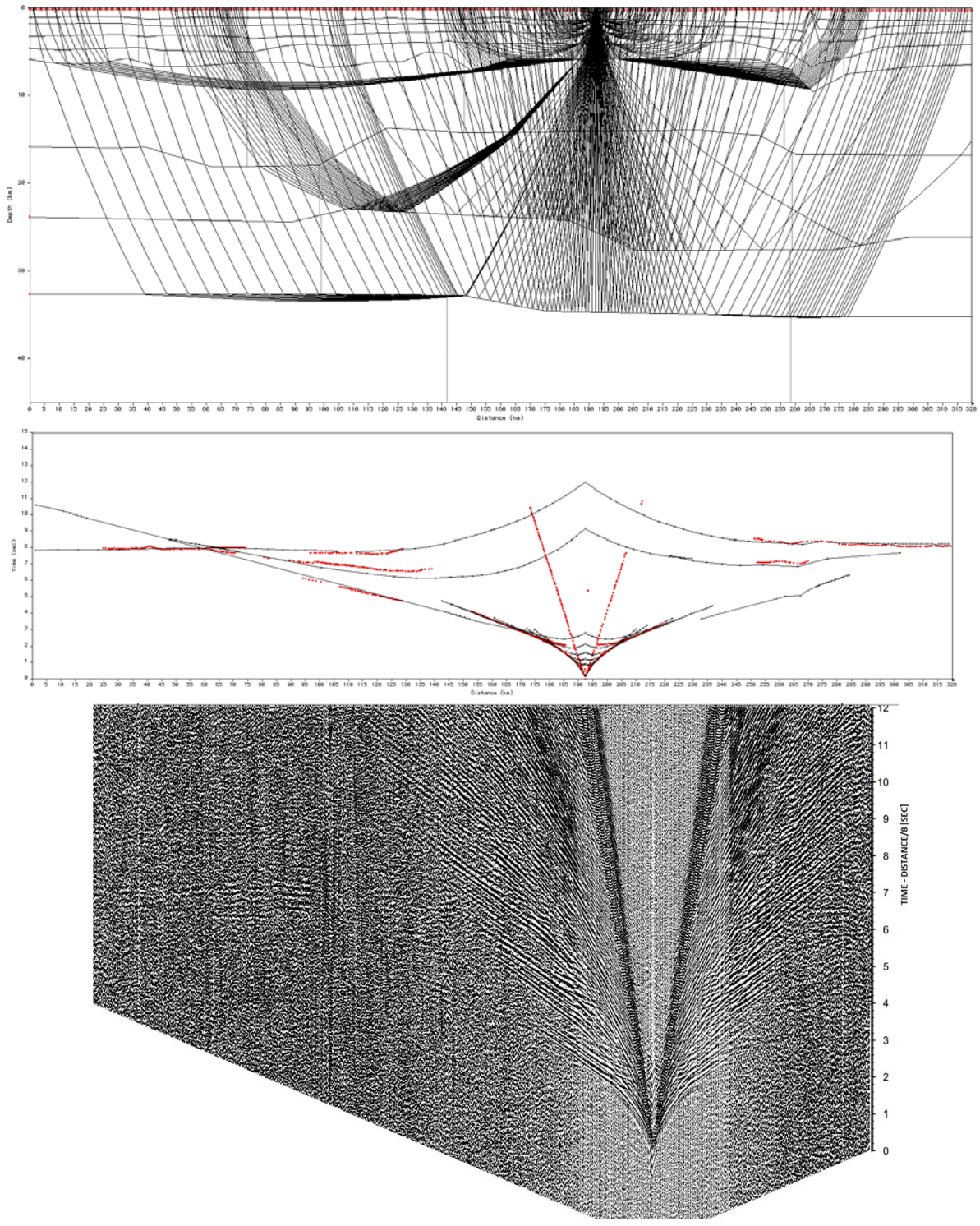

Fig. E - Upper plot shows computed rays traced through the model; middle plot contain calculated traveltime-curves (black) overlain by interpreted picks (red dots); and the lowermost plot is the associated seismogram.

OBS 24

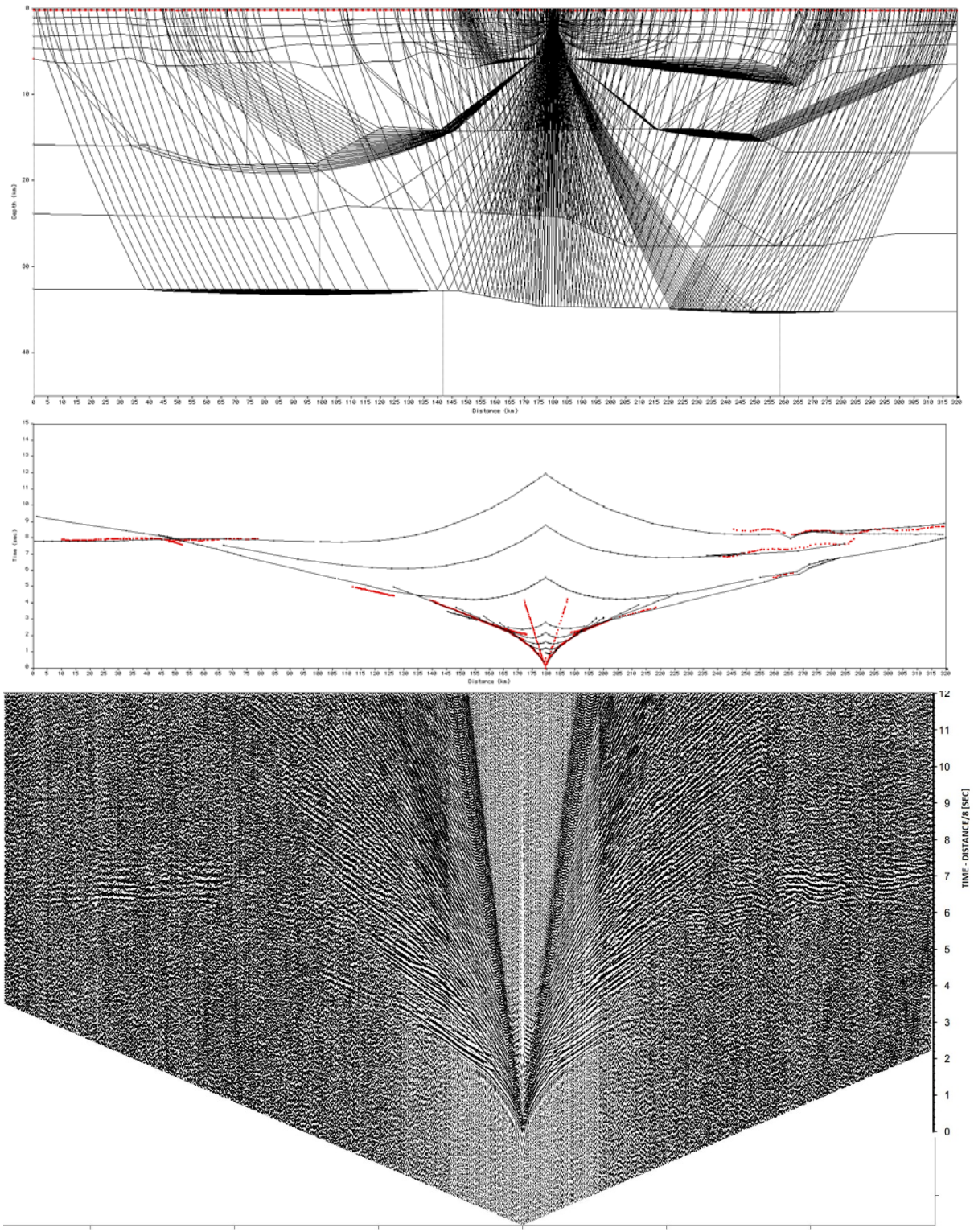

Fig. F - Upper plot shows computed rays traced through the model; middle plot contain calculated traveltime-curves (black) overlain by interpreted picks (red dots); and the lowermost plot is the associated seismogram.

OBS 25

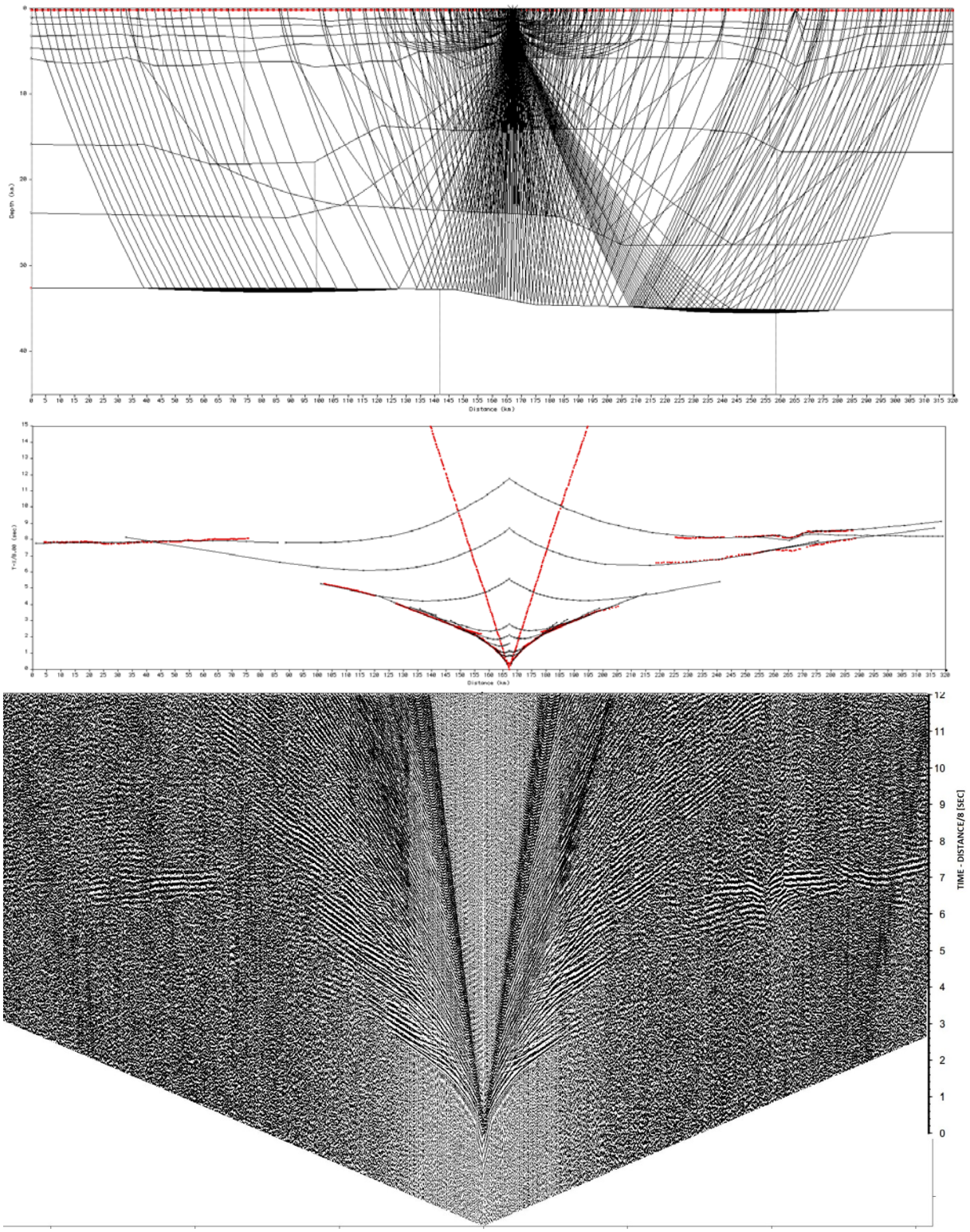

Fig. G - Upper plot shows computed rays traced through the model; middle plot contain calculated traveltime-curves (black) overlain by interpreted picks (red dots); and the lowermost plot is the associated seismogram.

OBS 26

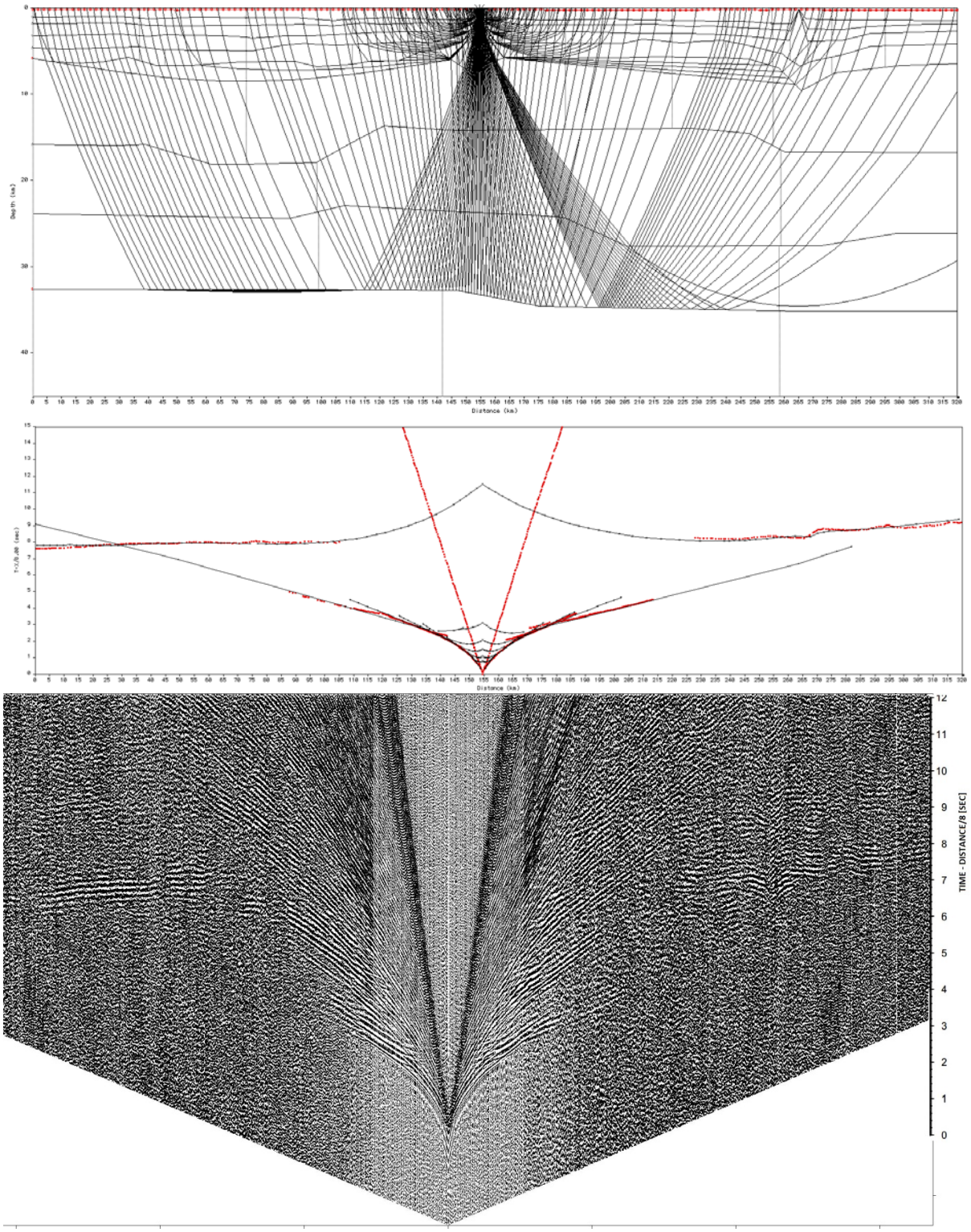

Fig. H - Upper plot shows computed rays traced through the model; middle plot contain calculated traveltime-curves (black) overlain by interpreted picks (red dots); and the lowermost plot is the associated seismogram.

OBS 27

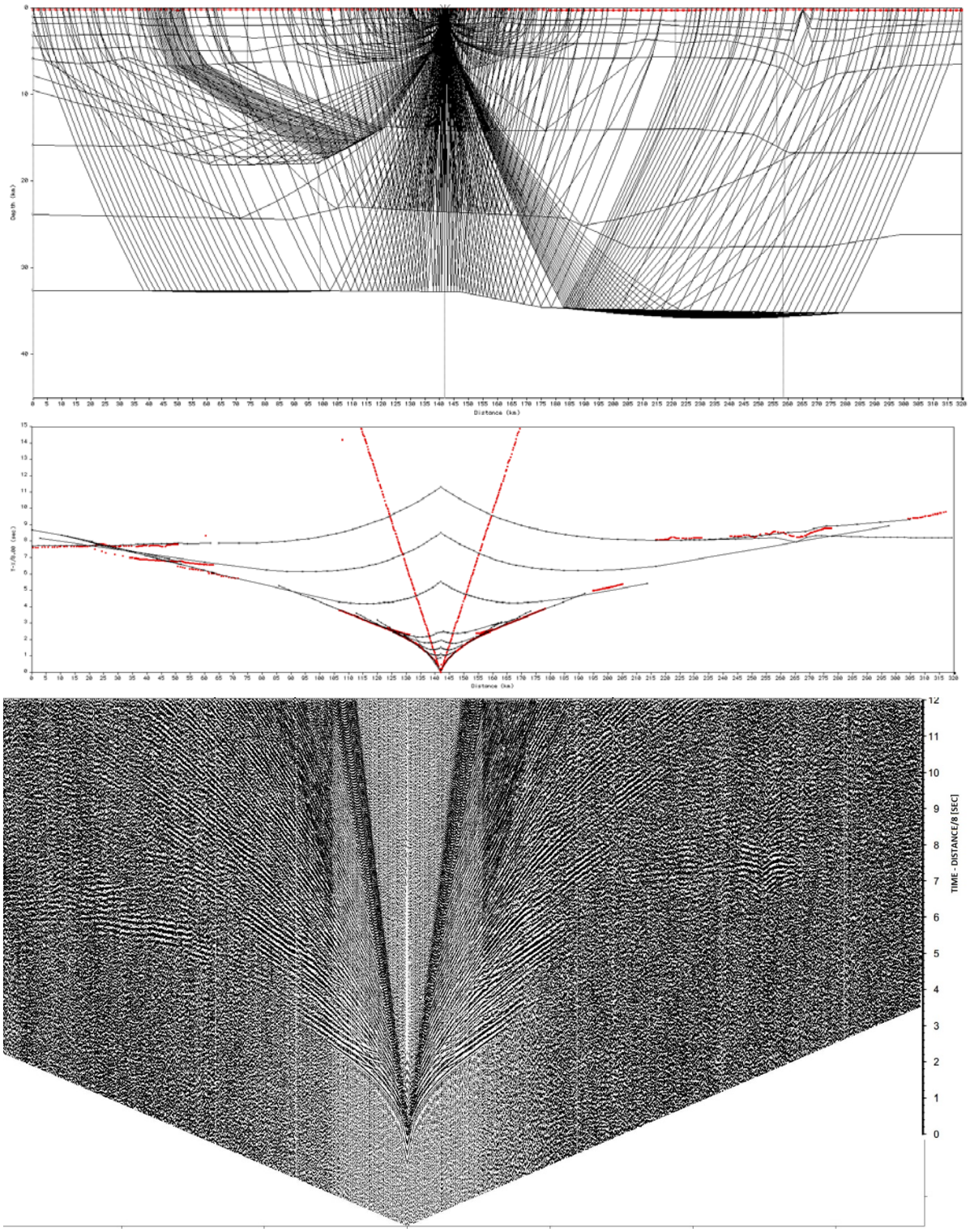

Fig. I - Upper plot shows computed rays traced through the model; middle plot contain calculated traveltime-curves (black) overlain by interpreted picks (red dots); and the lowermost plot is the associated seismogram.

OBS 28

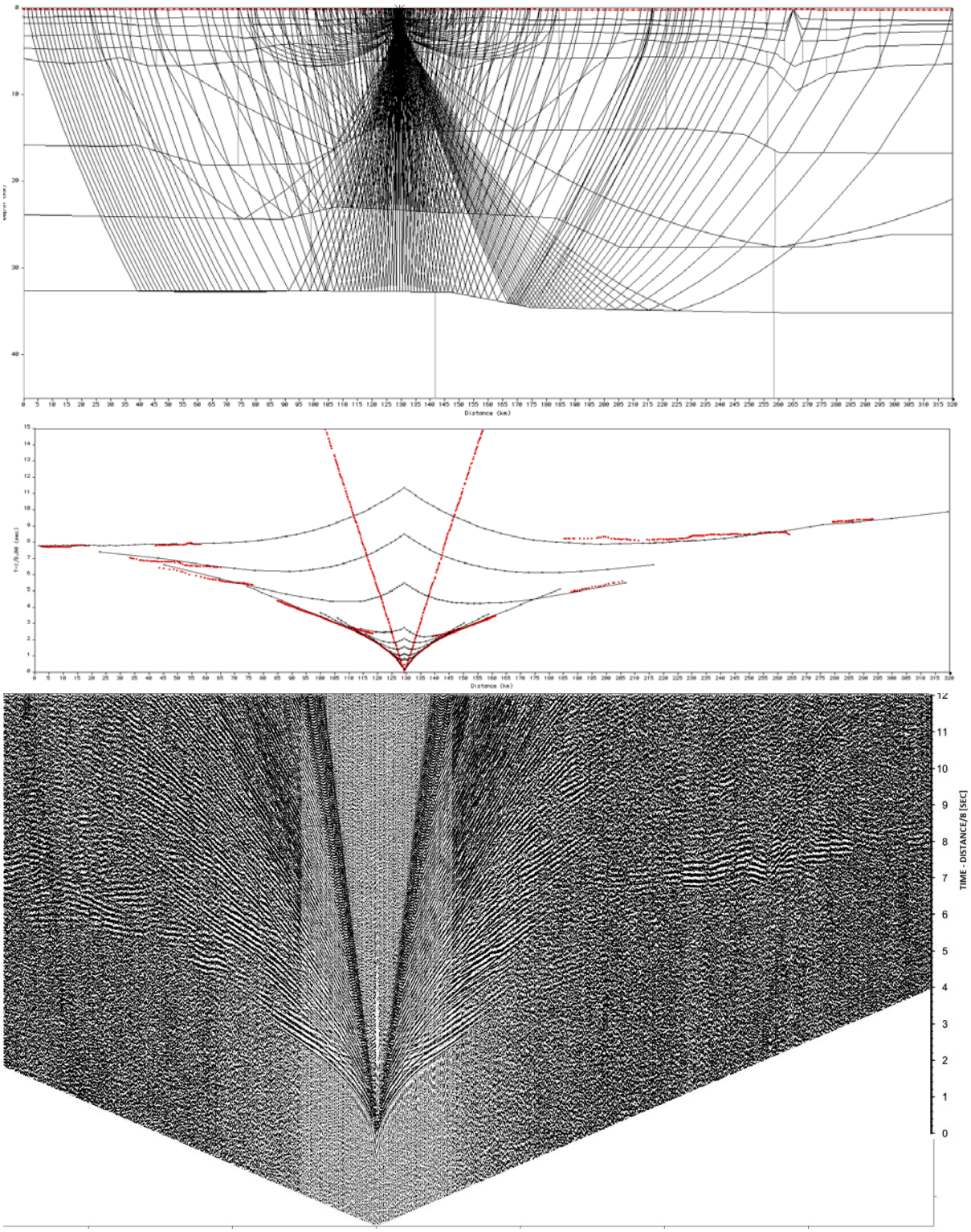

Fig. J - Upper plot shows computed rays traced through the model; middle plot contain calculated traveltime-curves (black) overlain by interpreted picks (red dots); and the lowermost plot is the associated seismogram.

OBS 29

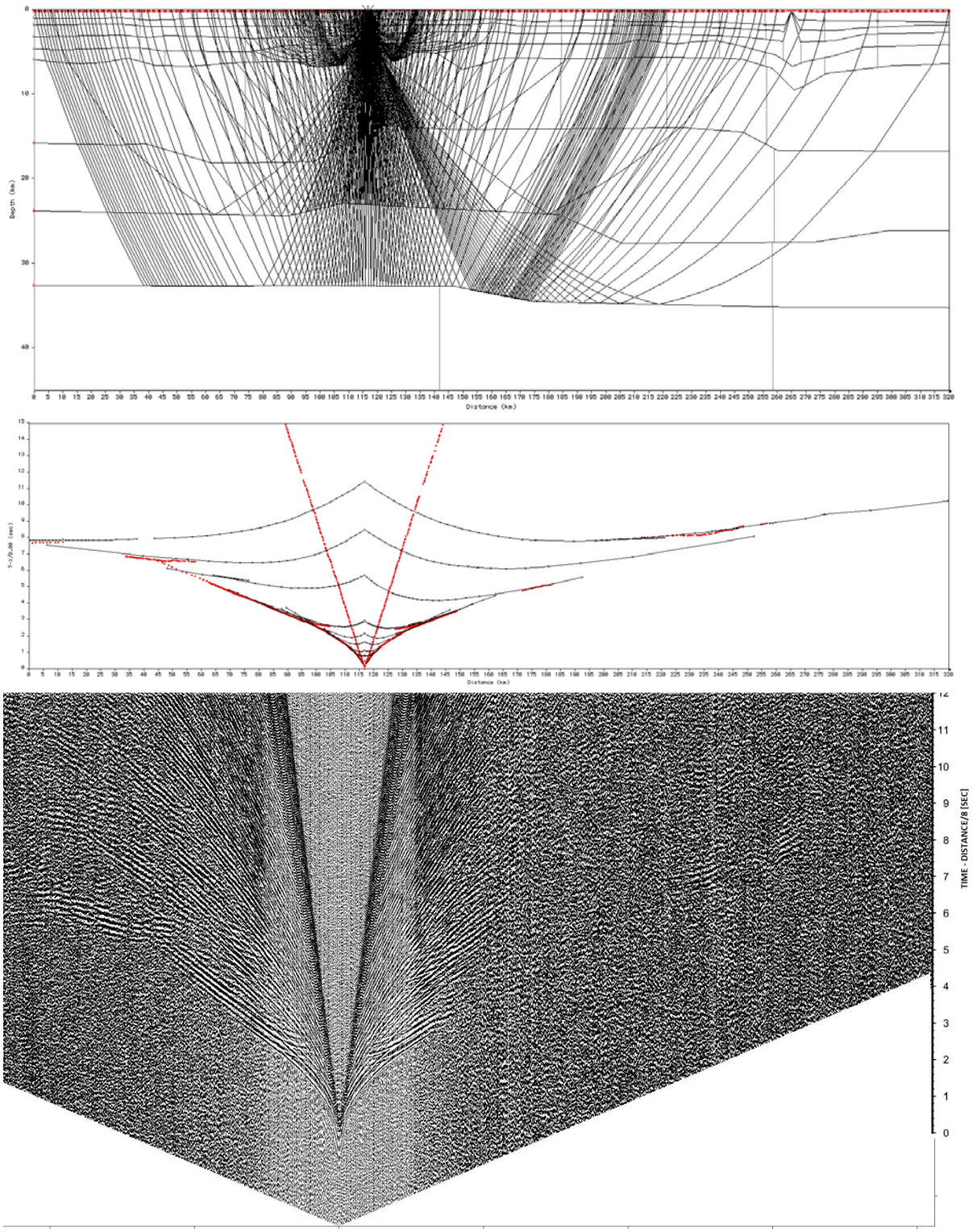

Fig. K - Upper plot shows computed rays traced through the model; middle plot contain calculated traveltime-curves (black) overlain by interpreted picks (red dots); and the lowermost plot is the associated seismogram.

OBS 30

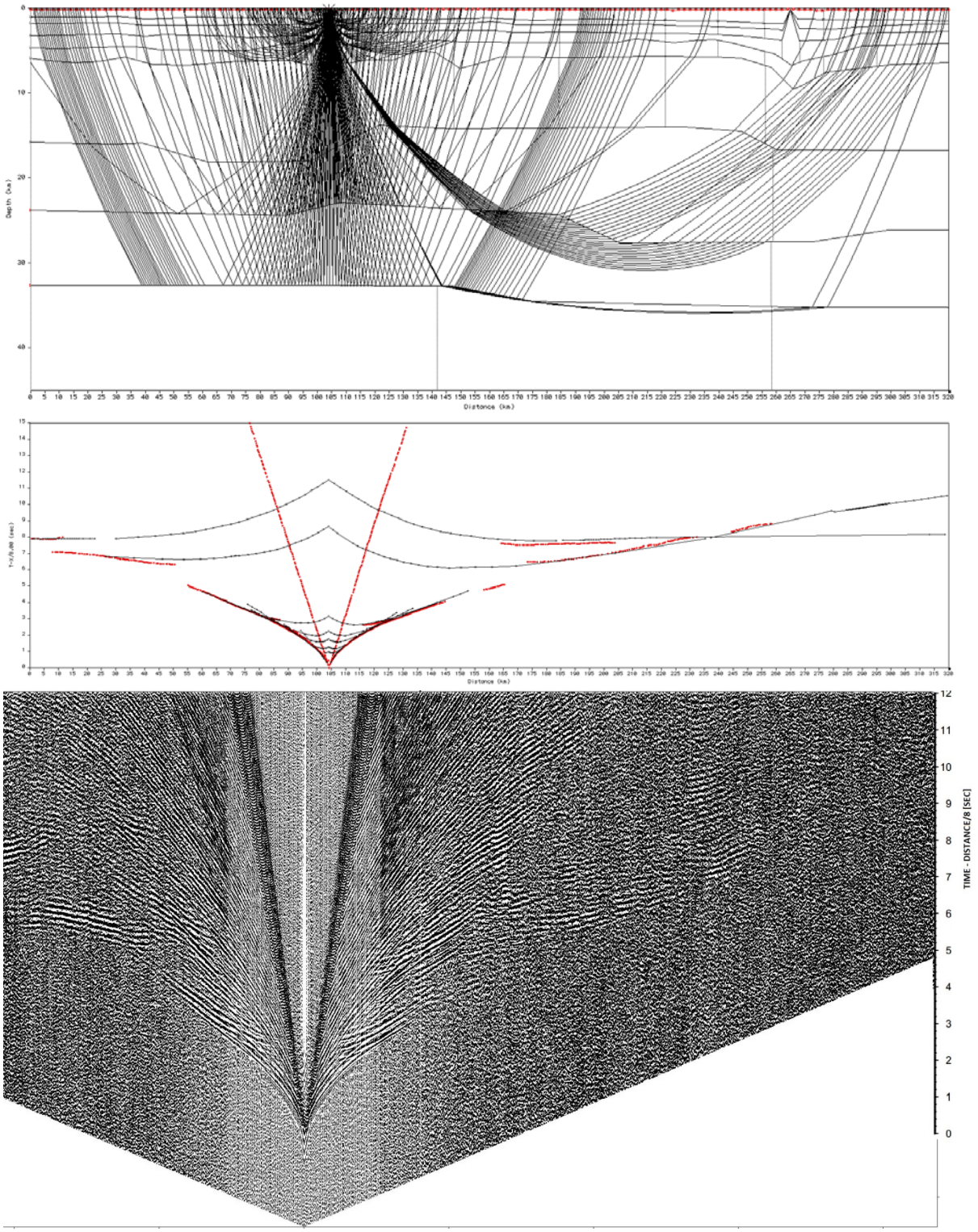

Fig. L - Upper plot shows computed rays traced through the model; middle plot contain calculated traveltime-curves (black) overlain by interpreted picks (red dots); and the lowermost plot is the associated seismogram.

OBS 31

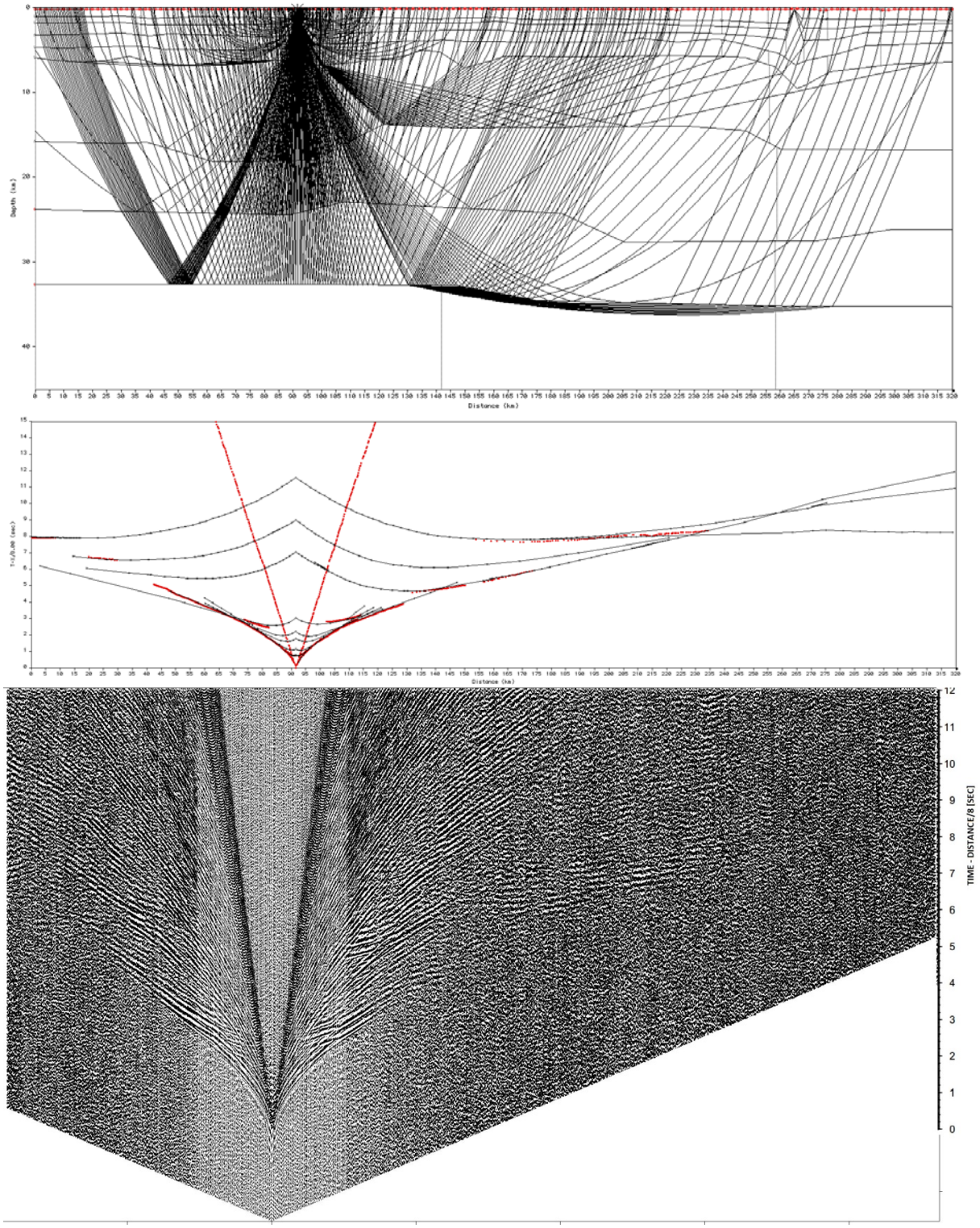

Fig. M - Upper plot shows computed rays traced through the model; middle plot contain calculated traveltime-curves (black) overlain by interpreted picks (red dots); and the lowermost plot is the associated seismogram.

OBS 32

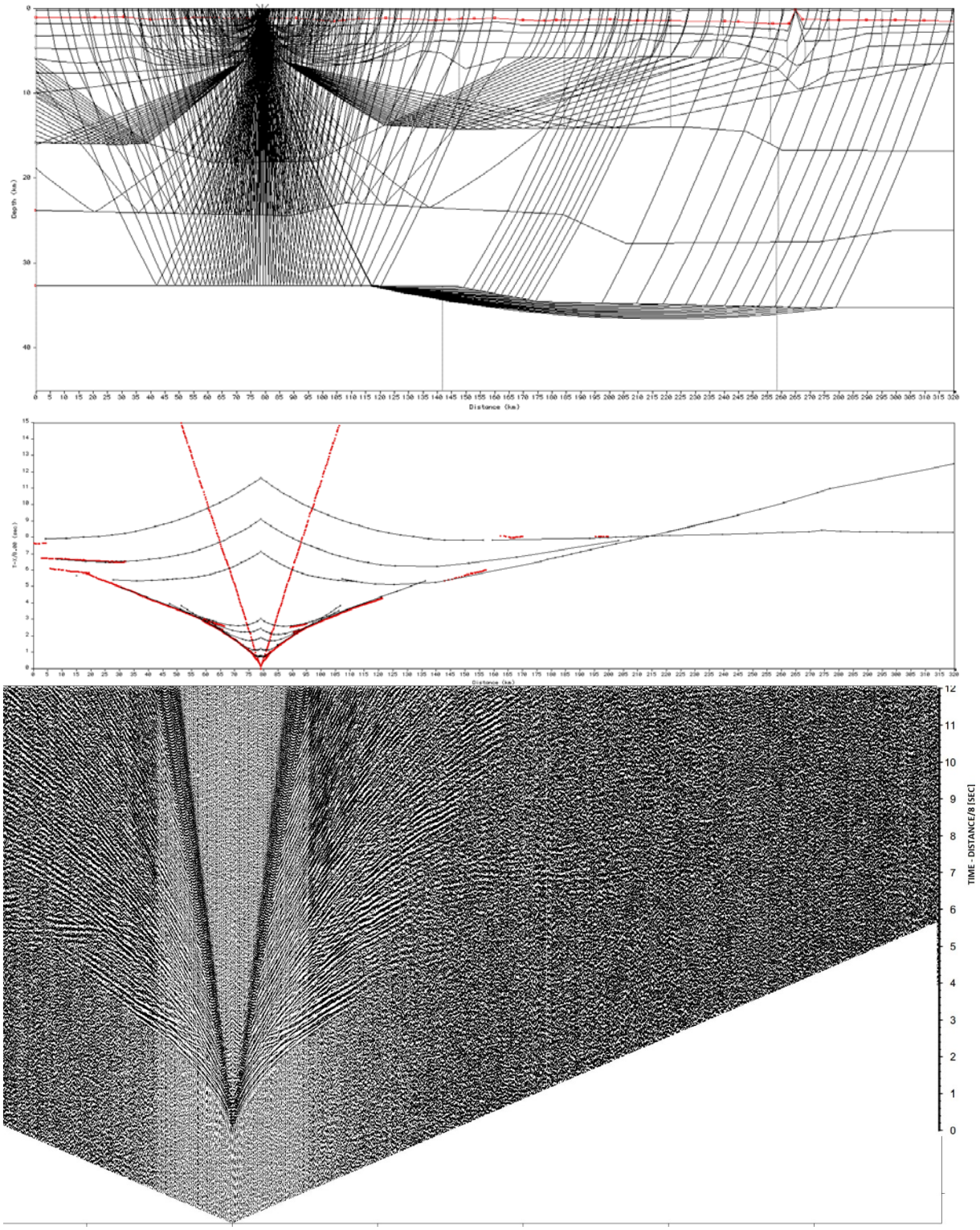

Fig. N - Upper plot shows computed rays traced through the model; middle plot contain calculated traveltime-curves (black) overlain by interpreted picks (red dots); and the lowermost plot is the associated seismogram.

OBS 33

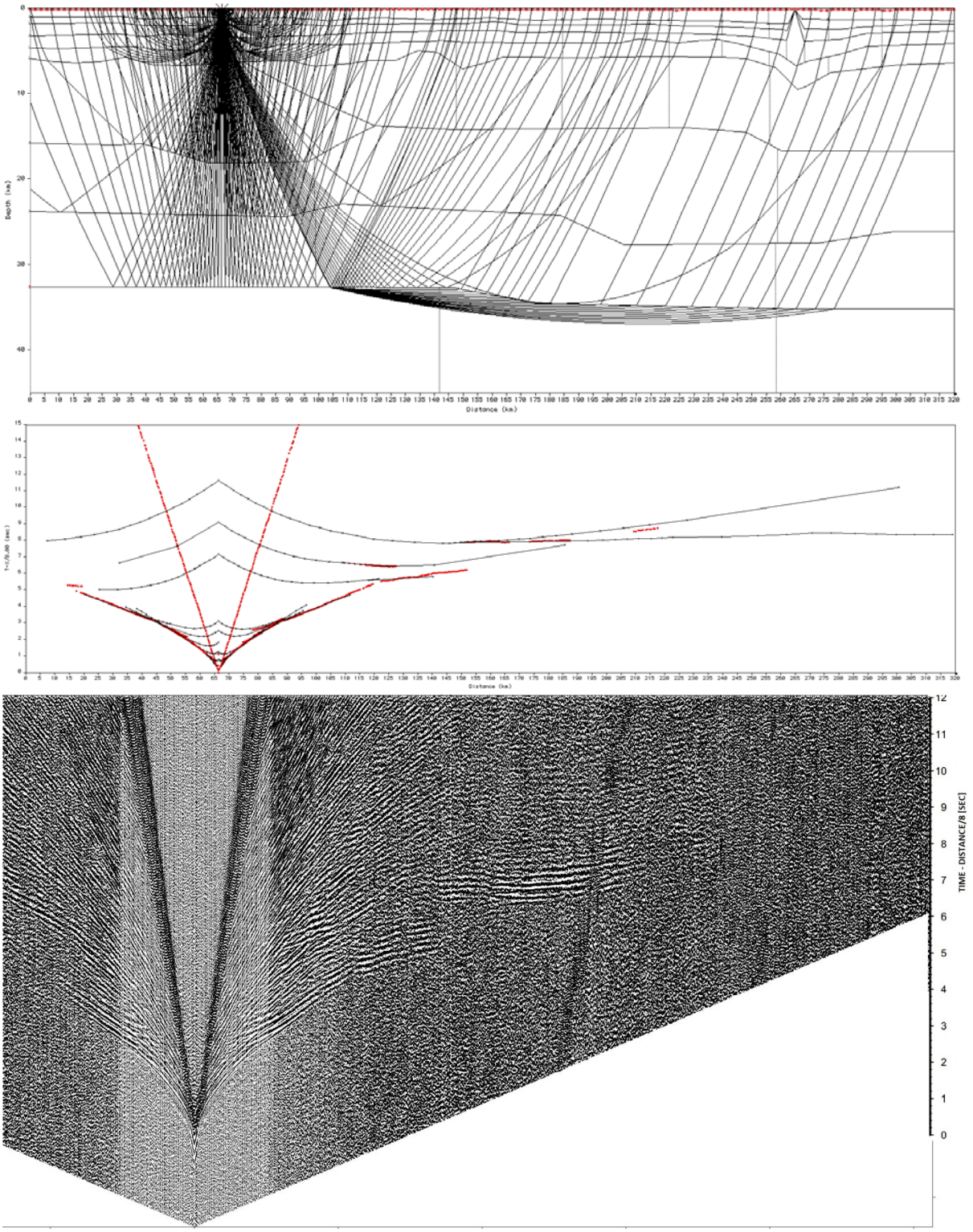

Fig. O - Upper plot shows computed rays traced through the model; middle plot contain calculated traveltime-curves (black) overlain by interpreted picks (red dots); and the lowermost plot is the associated seismogram.

OBS 34

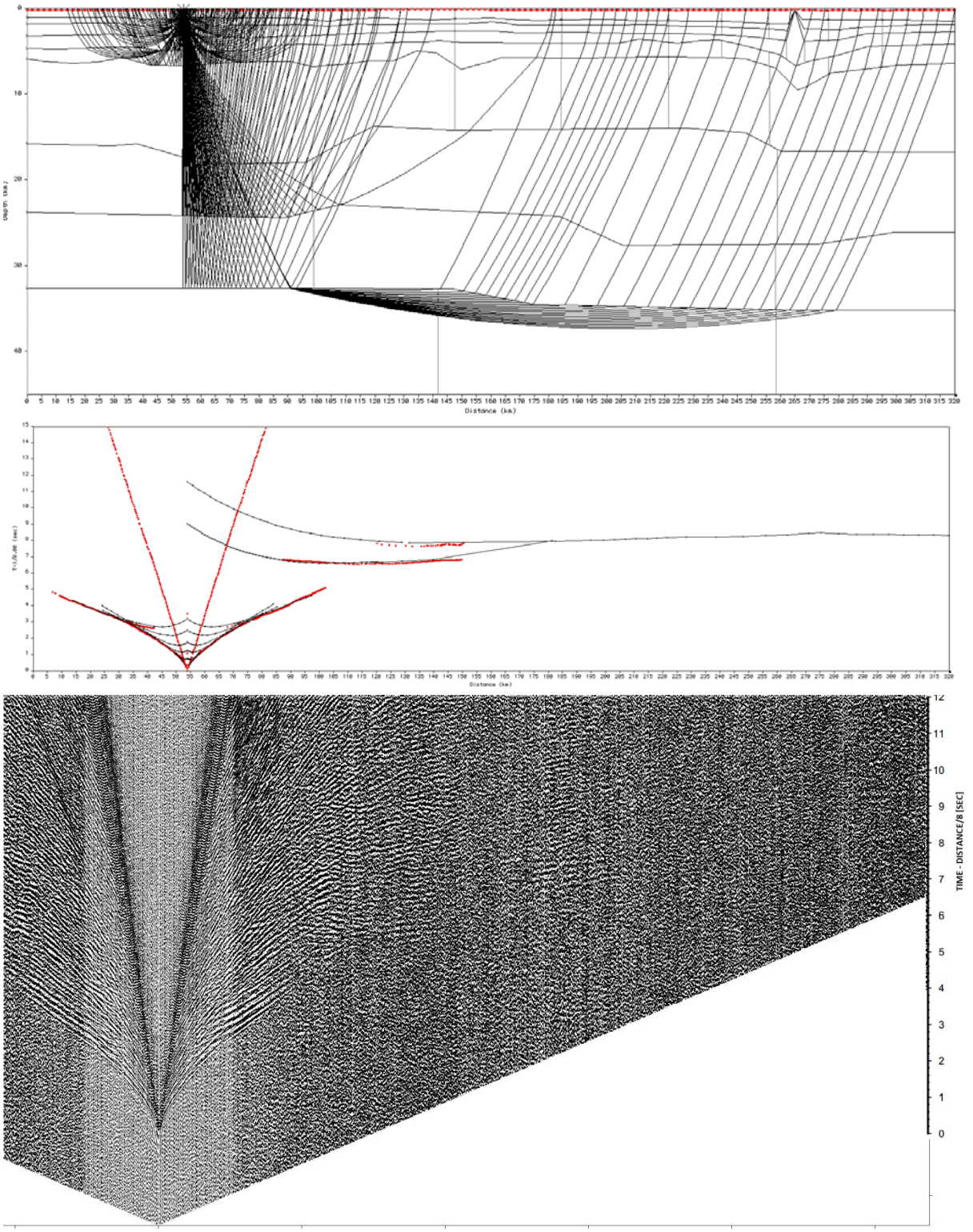

Fig. P - Upper plot shows computed rays traced through the model; middle plot contain calculated traveltime-curves (black) overlain by interpreted picks (red dots); and the lowermost plot is the associated seismogram.
OBS 35

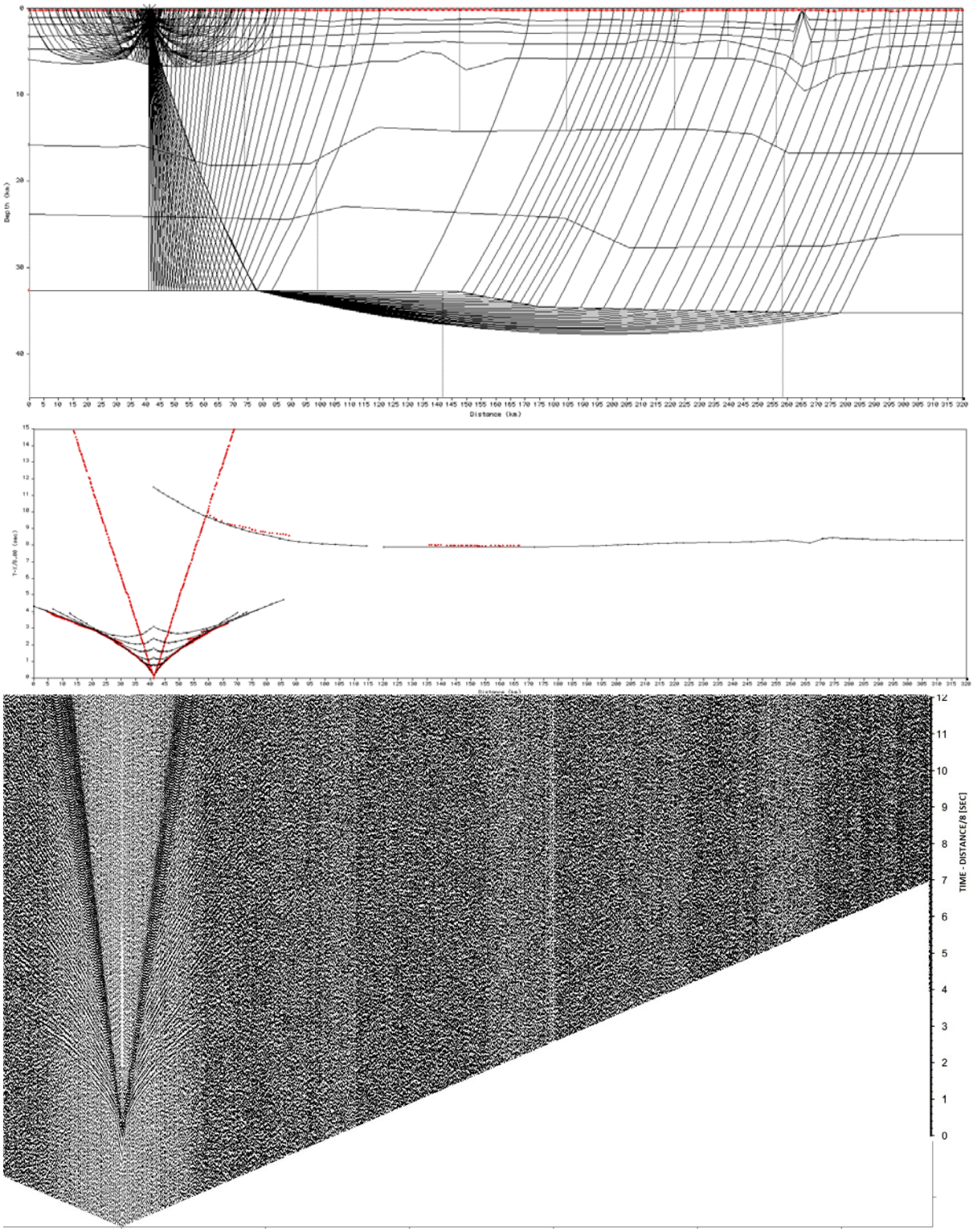

Fig. Q - Upper plot shows computed rays traced through the model; middle plot contain calculated traveltime-curves (black) overlain by interpreted picks (red dots); and the lowermost plot is the associated seismogram.

OBS 36

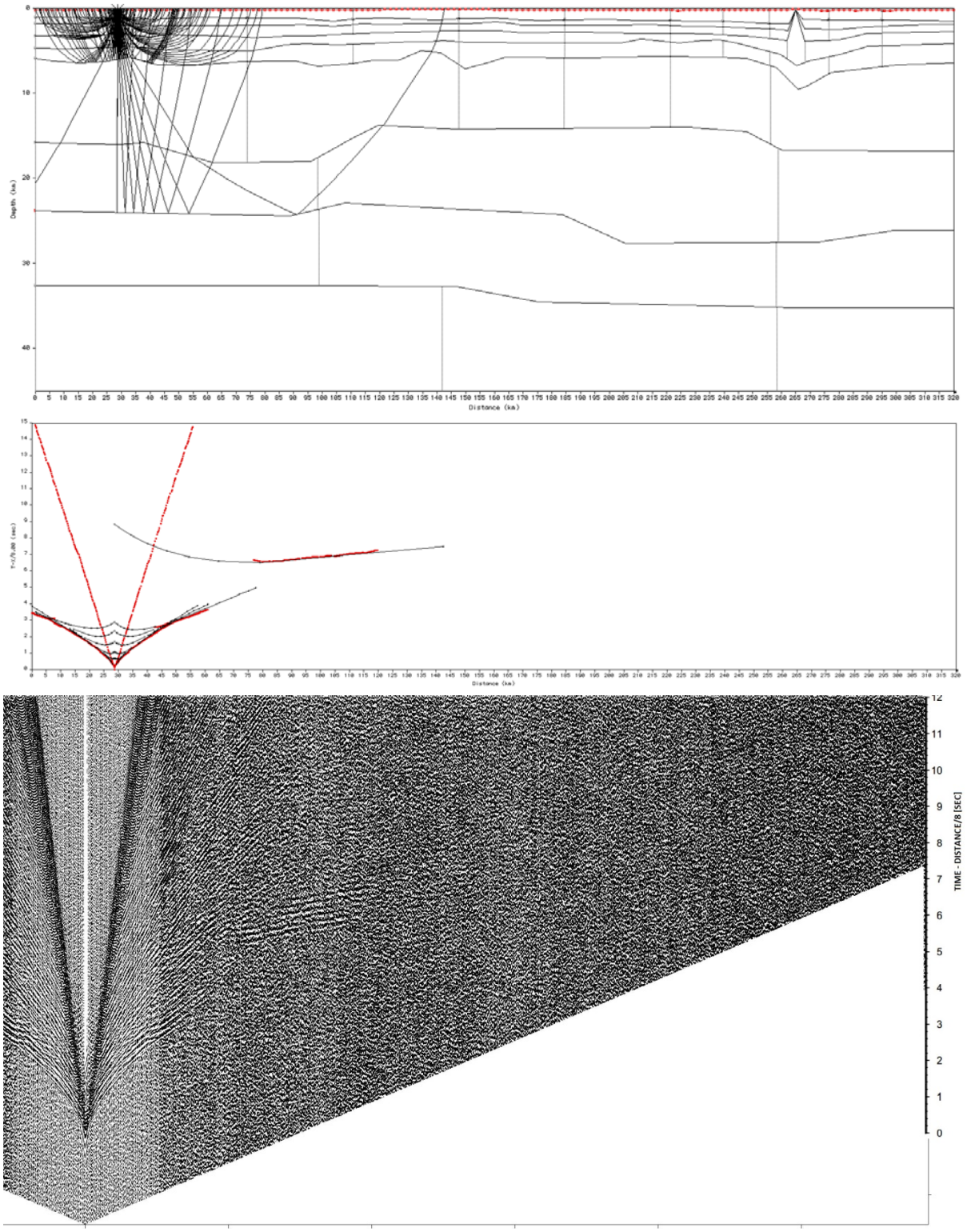

Fig. R - Upper plot shows computed rays traced through the model; middle plot contain calculated traveltime-curves (black) overlain by interpreted picks (red dots); and the lowermost plot is the associated seismogram.

OBS 37

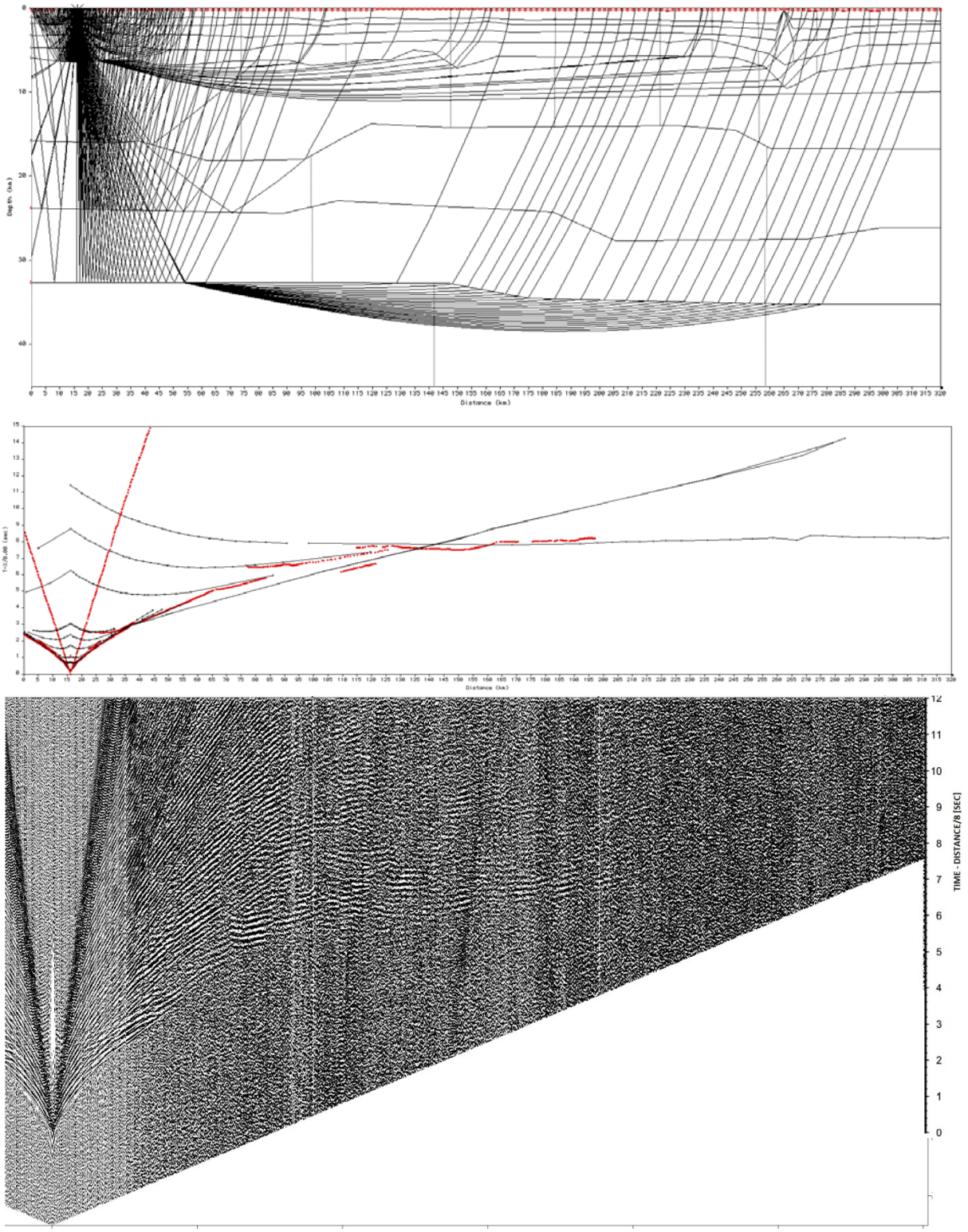

Fig. S - Upper plot shows computed rays traced through the model; middle plot contain calculated traveltime-curves (black) overlain by interpreted picks (red dots); and the lowermost plot is the associated seismogram.

OBS 38

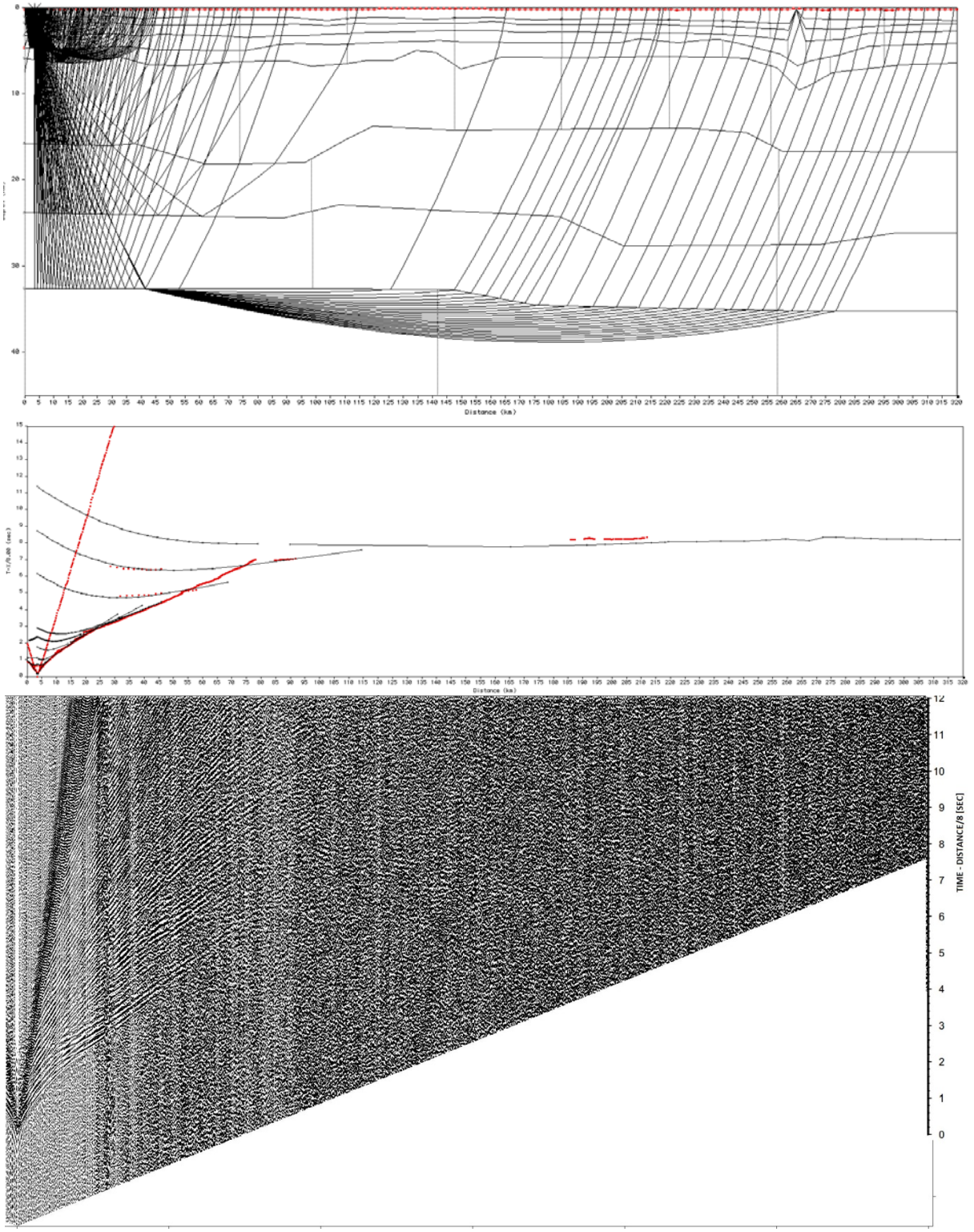

Fig. T - Upper plot shows computed rays traced through the model; middle plot contain calculated traveltime-curves (black) overlain by interpreted picks (red dots); and the lowermost plot is the associated seismogram.